Surface Passivation of Lead Halide Perovskite Semiconductors for Improved Stability and Performance

Farhad Akrami

A dissertation

submitted in partial fulfillment of the

requirements for the degree of

Doctor of Philosophy

University of Washington

2025

Reading Committee:

David S. Ginger, Chair

Brandi M. Cossairt

Dianne J. Xiao

Program Authorized to Offer Degree:

Chemistry

University of Washington

Abstract

Surface Passivation of Lead Halide Perovskite Semiconductors for Improved Stability and Performance

Farhad Akrami

Chair of the Supervisory Committee:

David S. Ginger

Department of Chemistry

Metal halide perovskites have emerged as one of the most promising classes of semiconductors for next-generation optoelectronic technologies, including solar cells, light-emitting diodes, and photodetectors. In photovoltaic devices, perovskites have achieved power conversion efficiencies that rival those of established commercial technologies. However, despite their remarkable progress, the widespread development of perovskite photovoltaics remains hindered by intrinsic instability and the presence of electronic defects, particularly those located at the surface. These surface defects play a crucial role in limiting performance, accelerating degradation, and mediating ionic and electronic processes that challenge long-term operational stability, making surface passivation a central focus in perovskite research for stable, high-efficiency devices.

To address these challenges, a variety of surface passivation strategies have been developed to mitigate defect states and suppress nonradiative recombination. While these approaches have demonstrated substantial improvements in both performance and stability, their implementation

across diverse perovskite compositions and synthetic routes remains nontrivial. The optimal passivation strategy often depends on subtle variations in chemistry, processing, and environmental conditions. Realizing effective passivation demands finely tuned treatment conditions that maximize benefits of defect suppression while minimizing unintended chemical or structural side effects. In this context, defect passivation represents both a scientific challenge and a technological opportunity to accelerate the path toward stable, commercially viable perovskite solar cells.

This dissertation investigates how surface passivation can be used to control ion motion and optimize interfacial properties in lead halide perovskite semiconductors. First, we demonstrate how surface passivation can kinetically suppress light-induced halide migration, thereby enhancing the photostability of perovskites. Second, we investigate the effects of aminosilane-based treatments, highlighting the significance of optimized treatment conditions, while also revealing surface reactivities of these molecules with formamidinium cations, linking interfacial chemistry to changes in optoelectronic behavior. Overall, these studies establish molecular surface passivation as a powerful route to tune ion migration, stability, and performance in lead halide perovskites. They provide insights that can help bridge interfacial chemistry with the practical requirements of durable perovskite optoelectronic technologies.

Table of Contents

Chapter 1: Introduction

1.1 Lead Halide Perovskites

Halide perovskites are a class of emerging semiconductors with the general chemical formula ABX_3, where A is a monovalent cation such as methylammonium (MA^+), formamidinium (FA^+), or Cesium (Cs^+). B is typically lead (Pb^{2+}), and X is a halide such as iodide (I^-), bromide (Br^-), or chloride (Cl^-).[1–4] These materials are mixed ionic-electronic conductors,[5,6] possessing a soft crystal lattice,[7] which together offer a unique combination of optoelectronic properties and processing advantages.[8]

From a manufacturing perspective, lead halide perovskites offer several advantages. They can be prepared from relatively abundant raw materials,[9,10] processed at low temperatures from solution, and are compatible with scalable deposition techniques.[11,12] These attributes make them promising candidates for cost-effective and potentially domestically manufactured optoelectronic technologies.[13,14]

On the photophysical front, lead halide perovskites exhibit high optical absorption coefficients,[1,15] long carrier diffusion lengths,[16] low exciton binding energies,[17] and tunable bandgaps through compositional alloying of both the cation and halide ions.[1,18] Mixed-cation, mixed-halide compositions can access wide bandgaps desirable for tandem solar cells and for light-emitting applications across the visible spectrum. Over the past decade, perovskite solar cells have demonstrated rapid advancements in power conversion efficiency (PCE), reaching 26.95% as single-junction devices and 34.85% as perovskite-silicon tandem cells.[19] Such reported record efficiencies highlight the promise of perovskites in next-generation solar energy systems.

Despite such reported remarkable efficiencies, the commercialization of perovskite solar technologies is held back due to stability concerns.[20] Various external stressors such as light, heat, and bias can accelerate degradation that affect both performance and stability.[21–25] As discussed earlier, low-temperature solution processing of perovskites, while advantageous for manufacturing, often result in defect-rich samples,[26,27] particularly at perovskite interfaces.[28] Among various surface defects, halide vacancies are especially parasitic due to their low formation energies, acting as nonradiative recombination centers and facilitating ionic migration.[26,29] Ion motion causes various undesirable phenomena, including current-voltage hysteresis in devices,[30] light-induced phase separation in mixed-ion compositions,[31–33] and performance loss.[34] Consequently, controlling perovskite defects, especially at the surface, is a critical area of focus in the field.

1.2 Surface Passivation

Lead halide perovskite surfaces play a crucial role in determining the performance and stability of these materials. At terminal planes, the disruption of the crystal lattice introduces under-coordinated ions, halide vacancies, and other point defects.[35] These surface defects facilitate trap-assisted nonradiative recombination and provide pathways for ion transport.[36] As a result, such defects not only reduce performance but also cause instability issues, making effective surface passivation a central strategy for improving both performance and stability in perovskite-based systems.

Surface passivation seeks to mitigate these issues by modifying the chemistry and structure of the exposed perovskite surface. To that end, a wide range of surface passivation strategies have been developed.[37] Molecular passivators such as organic ammonium salts, Lewis bases and amines,

including aminosilanes, have shown considerable promise in suppressing trap-assisted recombination.[38–41] These molecules can coordinate with point defects and improve photoluminescence properties. When properly optimized, such surface treatments can significantly enhance device efficiency and stability under operating conditions.[40,41]

However, the practical implementation of surface passivation is not without challenges. Lead halide perovskites are compositionally diverse, and different synthetic routes can yield surfaces with distinct defect landscapes. As a result, the "optimal" passivation strategy often requires precise tuning of the treatment conditions to ensure maximal benefit without undesirable issues. Furthermore, surface-treating molecules must be chemically compatible with the perovskite to avoid undesired phase instability. Ultimately, surface passivation represents both a scientific challenge and a technological opportunity. Researchers can address fundamental degradation mechanisms while pushing the performance of perovskite devices closer to their theoretical limits, by stabilizing perovskite surfaces and tuning their chemistry.

Within this broader context, two interrelated questions motivate the work in this dissertation:

1. Can molecular passivation be used to mitigate light-induced ion migration in wide-bandgap perovskites, thereby improving their photostability under illumination?
2. How do specific aminosilane structures and processing conditions influence interfacial chemistry, passivation quality, and device-relevant performance?

Addressing these questions requires a combination of detailed interfacial characterization and systematic variation of molecular treatments. These studies can help move from empirical optimization toward a more rational understanding of surface passivation mechanisms.

This thesis focuses on molecular surface passivation to control ion motion and tune interfacial optoelectronic properties in lead halide perovskite semiconductors. This work centers on two research studies that together illustrate how amino-silane-based treatments can be utilized, and must be carefully controlled, to improve stability and performance. Chapter 1 has provided a broad overview of the unique properties and challenges of lead halide perovskites, with particular emphasis on surface defects and surface-related instability. Chapter 2 presents an in-depth investigation into the kinetic suppression of photoinduced halide migration through surface passivation, highlighting the role of surface treatments in stabilizing wide bandgap perovskites under illumination.[32] Chapter 3 examines the effects of aminosilane-based surface treatments, emphasizing the importance of optimized treatment conditions and revealing surface reactivity of these molecules with formamidinium cations.[42] Collectively, these studies contribute to a broader understanding of how molecular surface passivation can be utilized to address performance and stability issues in halide perovskites, and ultimately, support their potential toward commercialization.

1.3 References

(1) Jena, A. K.; Kulkarni, A.; Miyasaka, T. Halide Perovskite Photovoltaics: Background, Status, and Future Prospects. *Chem. Rev.* **2019**, *119* (5), 3036–3103. https://doi.org/10.1021/acs.chemrev.8b00539.

(2) Tao, L.; Qiu, J.; Sun, B.; Wang, X.; Ran, X.; Song, L.; Shi, W.; Zhong, Q.; Li, P.; Zhang, H.; Xia, Y.; Müller-Buschbaum, P.; Chen, Y. Stability of Mixed-Halide Wide Bandgap Perovskite Solar Cells: Strategies and Progress. *Journal of Energy Chemistry* **2021**, *61*, 395–415. https://doi.org/10.1016/j.jechem.2021.03.038.

(3) Akkerman, Q. A.; Manna, L. What Defines a Halide Perovskite? *ACS Energy Lett.* **2020**, *5* (2), 604–610. https://doi.org/10.1021/acsenergylett.0c00039.

(4) Dong, H.; Ran, C.; Gao, W.; Li, M.; Xia, Y.; Huang, W. Metal Halide Perovskite for Next-Generation Optoelectronics: Progresses and Prospects. *eLight* **2023**, *3* (1), 3. https://doi.org/10.1186/s43593-022-00033-z.

(5) Tress, W. Metal Halide Perovskites as Mixed Electronic–Ionic Conductors: Challenges and Opportunities—From Hysteresis to Memristivity. *J. Phys. Chem. Lett.* **2017**, *8* (13), 3106–3114. https://doi.org/10.1021/acs.jpclett.7b00975.

(6) Marunchenko, A.; Kondratiev, V.; Pushkarev, A.; Khubezhov, S.; Baranov, M.; Nasibulin, A.; Makarov, S. Mixed Ionic-Electronic Conduction Enables Halide-Perovskite Electroluminescent Photodetector. *Laser & Photonics Reviews* **2023**, *17* (9), 2300141. https://doi.org/10.1002/lpor.202300141.

(7) Guo, Z.; Wang, J.; Yin, W.-J. Atomistic Origin of Lattice Softness and Its Impact on Structural and Carrier Dynamics in Three Dimensional Perovskites. *Energy Environ. Sci.* **2022**, *15* (2), 660–671. https://doi.org/10.1039/D1EE02131A.

(8) He, C.; Liu, X. The Rise of Halide Perovskite Semiconductors. *Light Sci Appl* **2023**, *12* (1), 15. https://doi.org/10.1038/s41377-022-01010-4.

(9) Li, B.; Li, S.; Gong, J.; Wu, X.; Li, Z.; Gao, D.; Zhao, D.; Zhang, C.; Wang, Y.; Zhu, Z. Fundamental Understanding of Stability for Halide Perovskite Photovoltaics: The Importance of Interfaces. *Chem* **2024**, *10* (1), 35–47. https://doi.org/10.1016/j.chempr.2023.09.002.

(10) Frost, J. M.; Walsh, A. What Is Moving in Hybrid Halide Perovskite Solar Cells? *Acc. Chem. Res.* **2016**, *49* (3), 528–535. https://doi.org/10.1021/acs.accounts.5b00431.

(11) Hoang, M. T.; Ünlü, F.; Martens, W.; Bell, J.; Mathur, S.; Wang, H. Towards the Environmentally Friendly Solution Processing of Metal Halide Perovskite Technology. *Green Chem.* **2021**, *23* (15), 5302–5336. https://doi.org/10.1039/D1GC01756J.

(12) Qiu, L.; He, S.; Ono, L. K.; Liu, S.; Qi, Y. Scalable Fabrication of Metal Halide Perovskite Solar Cells and Modules. *ACS Energy Lett.* **2019**, *4* (9), 2147–2167. https://doi.org/10.1021/acsenergylett.9b01396.

(13) Berry, J. J.; van de Lagemaat, J.; Al-Jassim, M. M.; Kurtz, S.; Yan, Y.; Zhu, K. Perovskite Photovoltaics: The Path to a Printable Terawatt-Scale Technology. *ACS Energy Lett.* **2017**, *2* (11), 2540–2544. https://doi.org/10.1021/acsenergylett.7b00964.

(14) Roose, B.; M. Tennyson, E.; Meheretu, G.; Kassaw, A.; A. Tilahun, S.; Allen, L.; D. Stranks, S. Local Manufacturing of Perovskite Solar Cells, a Game-Changer for Low- and Lower-Middle Income Countries? *Energy & Environmental Science* **2022**, *15* (9), 3571–3582. https://doi.org/10.1039/D2EE01343F.

(15) Faridi, A. W.; Imran, M.; Tariq, G. H.; Ullah, S.; Noor, S. F.; Ansar, S.; Sher, F. Synthesis and Characterization of High-Efficiency Halide Perovskite Nanomaterials for Light-Absorbing Applications. *Ind. Eng. Chem. Res.* **2023**, *62* (11), 4494–4502. https://doi.org/10.1021/acs.iecr.2c00416.

(16) Stranks, S. D.; Eperon, G. E.; Grancini, G.; Menelaou, C.; Alcocer, M. J. P.; Leijtens, T.; Herz, L. M.; Petrozza, A.; Snaith, H. J. Electron-Hole Diffusion Lengths Exceeding 1 Micrometer in an Organometal Trihalide Perovskite Absorber. *Science* **2013**, *342* (6156), 341–344. https://doi.org/10.1126/science.1243982.

(17) Miyata, A.; Mitioglu, A.; Plochocka, P.; Portugall, O.; Wang, J. T.-W.; Stranks, S. D.; Snaith, H. J.; Nicholas, R. J. Direct Measurement of the Exciton Binding Energy and Effective Masses for Charge Carriers in Organic–Inorganic Tri-Halide Perovskites. *Nature Phys* **2015**, *11* (7), 582–587. https://doi.org/10.1038/nphys3357.

(18) Xiao, Z.; Zhao, L.; Tran, N. L.; Lin, Y. L.; Silver, S. H.; Kerner, R. A.; Yao, N.; Kahn, A.; Scholes, G. D.; Rand, B. P. Mixed-Halide Perovskites with Stabilized Bandgaps. *Nano Lett.* **2017**, *17* (11), 6863–6869. https://doi.org/10.1021/acs.nanolett.7b03179.

(19) *Interactive Best Research-Cell Efficiency Chart | Photovoltaic Research | NREL*. https://www.nrel.gov/pv/interactive-cell-efficiency (accessed 2025-07-23).

(20) Siegler, T. D.; Dawson, A.; Lobaccaro, P.; Ung, D.; Beck, M. E.; Nilsen, G.; Tinker, L. L. The Path to Perovskite Commercialization: A Perspective from the United States Solar Energy Technologies Office. *ACS Energy Lett.* **2022**, *7* (5), 1728–1734. https://doi.org/10.1021/acsenergylett.2c00698.

(21) Jiang, F.; Shi, Y.; Rana, T. R.; Morales, D.; Gould, I. E.; McCarthy, D. P.; Smith, J. A.; Christoforo, M. G.; Yaman, M. Y.; Mandani, F.; Terlier, T.; Contreras, H.; Barlow, S.; Mohite, A. D.; Snaith, H. J.; Marder, S. R.; MacKenzie, J. D.; McGehee, M. D.; Ginger, D. S. Improved Reverse Bias Stability in p–i–n Perovskite Solar Cells with Optimized Hole Transport Materials and Less Reactive Electrodes. *Nat Energy* **2024**, *9* (10), 1275–1284. https://doi.org/10.1038/s41560-024-01600-z.

(22) Ono, L. K.; Qi, Y.; Liu, S. (Frank). Progress toward Stable Lead Halide Perovskite Solar Cells. *Joule* **2018**, *2* (10), 1961–1990. https://doi.org/10.1016/j.joule.2018.07.007.

(23) Chen, J.; Hong, X.; Wang, Y.; Guan, X.; Wang, R.; Wang, Y.; Du, H.; Zhang, Y.; Shen, S. Instability Issues and Stabilization Strategies of Lead Halide Perovskites for Photo(Electro)Catalytic Solar Fuel Production. *J. Phys. Chem. Lett.* **2022**, *13* (7), 1806–1824. https://doi.org/10.1021/acs.jpclett.1c04017.

(24) Zhang, C.-X.; Shen, T.; Guo, D.; Tang, L.-M.; Yang, K.; Deng, H.-X. Reviewing and Understanding the Stability Mechanism of Halide Perovskite Solar Cells. *InfoMat* **2020**, *2* (6), 1034–1056. https://doi.org/10.1002/inf2.12104.

(25) Quitsch, W.-A.; deQuilettes, D. W.; Pfingsten, O.; Schmitz, A.; Ognjanovic, S.; Jariwala, S.; Koch, S.; Winterer, M.; Ginger, D. S.; Bacher, G. The Role of Excitation Energy in Photobrightening and Photodegradation of Halide Perovskite Thin Films. *J. Phys. Chem. Lett.* **2018**, *9* (8), 2062–2069. https://doi.org/10.1021/acs.jpclett.8b00212.

(26) Ono, L. K.; Liu, S. (Frank); Qi, Y. Reducing Detrimental Defects for High-Performance Metal Halide Perovskite Solar Cells. *Angewandte Chemie International Edition* **2019**, *59* (17), 6676–6698. https://doi.org/10.1002/anie.201905521.

(27) Motti, S. G.; Meggiolaro, D.; Martani, S.; Sorrentino, R.; Barker, A. J.; De Angelis, F.; Petrozza, A. Defect Activity in Lead Halide Perovskites. *Advanced Materials* **2019**, *31* (47), 1901183. https://doi.org/10.1002/adma.201901183.

(28) Schulz, P.; Cahen, D.; Kahn, A. Halide Perovskites: Is It All about the Interfaces? *Chem. Rev.* **2019**, *119* (5), 3349–3417. https://doi.org/10.1021/acs.chemrev.8b00558.

(29) Eames, C.; Frost, J. M.; Barnes, P. R. F.; O'Regan, B. C.; Walsh, A.; Islam, M. S. Ionic Transport in Hybrid Lead Iodide Perovskite Solar Cells. *Nature Communications* **2015**, *6* (1), 7497. https://doi.org/10.1038/ncomms8497.

(30) Meloni, S.; Moehl, T.; Tress, W.; Franckevičius, M.; Saliba, M.; Lee, Y. H.; Gao, P.; Nazeeruddin, M. K.; Zakeeruddin, S. M.; Rothlisberger, U.; Graetzel, M. Ionic Polarization-Induced Current–Voltage Hysteresis in CH3NH3PbX3 Perovskite Solar Cells. *Nat Commun* **2016**, *7* (1), 10334. https://doi.org/10.1038/ncomms10334.

(31) Hoke, E. T.; Slotcavage, D. J.; Dohner, E. R.; Bowring, A. R.; Karunadasa, H. I.; McGehee, M. D. Reversible Photo-Induced Trap Formation in Mixed-Halide Hybrid Perovskites for Photovoltaics. *Chem. Sci.* **2014**, *6* (1), 613–617. https://doi.org/10.1039/C4SC03141E.

(32) Akrami, F.; Jiang, F.; Giridharagopal, R.; Ginger, D. S. Kinetic Suppression of Photoinduced Halide Migration in Wide Bandgap Perovskites via Surface Passivation. *J. Phys. Chem. Lett.* **2023**, *14* (41), 9310–9315. https://doi.org/10.1021/acs.jpclett.3c02570.

(33) Pothoof, J.; Westbrook, R. J. E.; Giridharagopal, R.; Breshears, M. D.; Ginger, D. S. Surface Passivation Suppresses Local Ion Motion in Halide Perovskites. *J. Phys. Chem. Lett.* **2023**, *14* (26), 6092–6098. https://doi.org/10.1021/acs.jpclett.3c01089.

(34) Zhang, D.; Li, D.; Hu, Y.; Mei, A.; Han, H. Degradation Pathways in Perovskite Solar Cells and How to Meet International Standards. *Commun Mater* **2022**, *3* (1), 58. https://doi.org/10.1038/s43246-022-00281-z.

(35) Ono, L. K.; Liu, S. (Frank); Qi, Y. Reducing Detrimental Defects for High-Performance Metal Halide Perovskite Solar Cells. *Angewandte Chemie International Edition* **2020**, *59* (17), 6676–6698. https://doi.org/10.1002/anie.201905521.

(36) Walsh, A.; Stranks, S. D. Taking Control of Ion Transport in Halide Perovskite Solar Cells. *ACS Energy Lett.* **2018**, *3* (8), 1983–1990. https://doi.org/10.1021/acsenergylett.8b00764.

(37) Chen, B.; Rudd, P. N.; Yang, S.; Yuan, Y.; Huang, J. Imperfections and Their Passivation in Halide Perovskite Solar Cells. *Chem. Soc. Rev.* **2019**, *48* (14), 3842–3867.

https://doi.org/10.1039/C8CS00853A.

(38) Tan, S.; Huang, T.; Yang, Y. Defect Passivation of Perovskites in High Efficiency Solar Cells. *J. Phys. Energy* **2021**, *3* (4), 042003. https://doi.org/10.1088/2515-7655/ac2e13.

(39) Jariwala, S.; Burke, S.; Dunfield, S.; Shallcross, R. C.; Taddei, M.; Wang, J.; Eperon, G. E.; Armstrong, N. R.; Berry, J. J.; Ginger, D. S. Reducing Surface Recombination Velocity of Methylammonium-Free Mixed-Cation Mixed-Halide Perovskites via Surface Passivation. *Chem. Mater.* **2021**, *3* (13), 5035–5044. https://doi.org/10.1021/acs.chemmater.1c00848.

(40) Shi, Y.; Rojas-Gatjens, E.; Wang, J.; Pothoof, J.; Giridharagopal, R.; Ho, K.; Jiang, F.; Taddei, M.; Yang, Z.; Sanehira, E. M.; Irwin, M. D.; Silva-Acuña, C.; Ginger, D. S. (3-Aminopropyl)Trimethoxysilane Surface Passivation Improves Perovskite Solar Cell Performance by Reducing Surface Recombination Velocity. *ACS Energy Lett.* **2022**, *7* (11), 4081–4088. https://doi.org/10.1021/acsenergylett.2c01766.

(41) Lin, Y.-H.; Vikram; Yang, F.; Cao, X.-L.; Dasgupta, A.; Oliver, R. D. J.; Ulatowski, A. M.; McCarthy, M. M.; Shen, X.; Yuan, Q.; Christoforo, M. G.; Yeung, F. S. Y.; Johnston, M. B.; Noel, N. K.; Herz, L. M.; Islam, M. S.; Snaith, H. J. Bandgap-Universal Passivation Enables Stable Perovskite Solar Cells with Low Photovoltage Loss. *Science* **2024**, *384* (6697), 767–775. https://doi.org/10.1126/science.ado2302.

(42) Huang, Z.; Akrami, F.; Zhang, J.; Barlow, S.; Marder, S. R.; Ginger, D. S. Surface Passivation for Halide Optoelectronics: Comparing Optimization and Reactivity of Amino-Silanes with Formamidinium. *J. Am. Chem. Soc.* **2025**, *147* (46), 42918–42925. https://doi.org/10.1021/jacs.5c15574.

Chapter 2: Kinetic Suppression of Photoinduced Halide Migration in Wide Bandgap Perovskites via Surface Passivation

Adapted from Akrami, F.; Jiang, F.; Giridharagopal, R.; Ginger, D. S. Kinetic Suppression of Photoinduced Halide Migration in Wide Bandgap Perovskites via Surface Passivation. *J. Phys. Chem. Lett.* **2023**, *14* (41), 9310–9315. https://doi.org/10.1021/acs.jpclett.3c02570.

2.1 Overview

In this work, we study the kinetics of photoinduced halide migration in $FA_{0.8}Cs_{0.2}Pb(I_{0.8}Br_{0.2})_3$ wide (~1.69 eV) bandgap perovskites and show halide migration slows down following surface passivation with (3-aminopropyl) trimethoxysilane (APTMS). We use scanning Kelvin probe microscopy (SKPM) to probe the contact potential difference (CPD) shift under illumination, and the kinetics of surface potential relaxation in the dark. Our results show APTMS-passivated perovskites exhibit a smaller CPD shift under illumination, and a slower surface potential relaxation in the dark. We compare the evolution of the photoluminescence spectra of APTMS-passivated and unpassivated perovskites under illumination. We find that APTMS-passivated perovskites exhibit more than 5 times slower photoluminescence redshift, consistent with the slower surface potential relaxation as observed by SKPM. These observations provide evidence for kinetic suppression of photoinduced halide migration in APTMS-passivated samples, likely due to reduced halide vacancy densities, opening avenues to more efficient and stable devices.

2.2 Introduction

Metal halide perovskites are being widely explored in applications ranging from solar cells and light-emitting diodes to sources of quantum light.[1–5] The research community is demonstrating rapid advancements in the performance of these devices. For instance, in 2023, the perovskite solar

cell power conversion efficiency (PCE) record stands at 26.1% for single junction and 33.7% for perovskite-silicon tandems, compared to 23.3% and 27.3% only 5 years ago.[6] At the same time, improved materials have enabled efficient perovskite light-emitting diodes,[3] and even coherent single photon sources.[5]

While perovskites are attractive semiconductor materials because they are easily synthesized and processed over large areas at low temperatures, these properties make them prone to a range of surface and bulk defects.[7–11] Understanding and controlling these defects, particularly unpassivated surface states, is important due to their influence on nonradiative loss pathways that affect device performance and stability.[12–16] Furthermore, certain defects like halide vacancies also facilitate ionic conductivity, for instance via vacancy migration.[17–21] Passivation strategies that remove halide vacancies could thus have important implications for materials performance and stability, especially for the mixed halide perovskites that are commonly used to tailor the semiconductor bandgap in solar cell and light-emitting diode applications.[2,3,22,23]

Many groups have studied surface passivation strategies, usually with an emphasis on reducing non-radiative recombination as probed by photoluminescence.[11,24–27] Others have focused on photoinduced ion migration in both pure halide and mixed halide compositions.[28–33] However, despite the need for understanding and controlling the kinetics of photoinduced ion migration, experimental evidence for kinetic effects of surface passivation on photoinduced halide migration is limited.[34–36]

Previously, our group has shown that (3-aminopropyl) trimethoxysilane (APTMS) can successfully reduce nonradiative recombination,[11] improve the open-circuit voltage of devices,[37] and mitigate electric field-induced ion motion in perovskite films.[38] Based on the role of halide vacancies in ion migration,[17–21] we hypothesize that surface passivation should also kinetically

hinder *photoinduced* ion migration by reducing the density of halide vacancies. In this work, we test this hypothesis by studying the kinetic effects of APTMS surface passivation on photoinduced halide migration in $FA_{0.8}Cs_{0.2}Pb(I_{0.8}Br_{0.2})_3$, a wide bandgap perovskite (E_g of 1.69 eV). We chose this formulation as it offers an ideal optical bandgap for top sub-cells in perovskite-silicon tandems. We study the effects of passivating the perovskite surfaces with APTMS by tracking both the contact potential difference (CPD) shift and photoluminescence evolution with time under illumination, and the kinetics of surface potential relaxation in the dark following illumination. Consistent with our hypothesis, we observe that APTMS-treated samples undergo a smaller CPD shift under illumination and exhibit a slower surface potential relaxation in the dark. In addition, the APTMS-treated samples show more than 5 times slower redshift in photoluminescence under illumination.

2.3 Results and Discussion

We synthesize $FA_{0.8}Cs_{0.2}Pb(I_{0.8}Br_{0.2})_3$ perovskites by adapting previously reported methods[39] as described in detail in the Appendix A. To passivate the surface of these samples, we deposit APTMS using a vacuum oven for 5 minutes, as in our previous work (see Appendix A).[11] We measure the bandgap to be ~1.69 eV via UV-Vis spectroscopy (Appendix A, Figure S1a), and confirm the perovskite structure via X-ray diffraction (XRD) (Appendix A, Figure S1b). Appendix A, Figure S1b shows that there are no detectable changes to the perovskite XRD patterns after APTMS surface passivation. We confirm the successful surface passivation of this perovskite composition by APTMS via steady-state and time-resolved photoluminescence, which show significant increases in photoluminescence intensity (~36 times increase) and photoluminescence lifetime (~7 times increase) (Appendix A, Figure S3 – 4).

To further study the effects of perovskite surface passivation with APTMS, we use scanning Kelvin probe microscopy (SKPM) to probe the CPD shift under illumination and the kinetics of surface potential relaxation in the dark following illumination (Figure 1). Figure 1a shows a schematic diagram of the samples used for the SKPM and steady-state photoluminescence measurements in this study (see Appendix A for details). Briefly, we deposit the perovskite films on spin coated SnO_2 electron transport layer on top of indium tin oxide (ITO) covered glass substrates. Figure 1a also shows the molecular structure of the APTMS monomer, and the structure of the first layer of polymerized APTMS as it is likely to interact with the perovskite.[11] Figure 1b depicts a simplified SKPM measurement setup employed in this study.

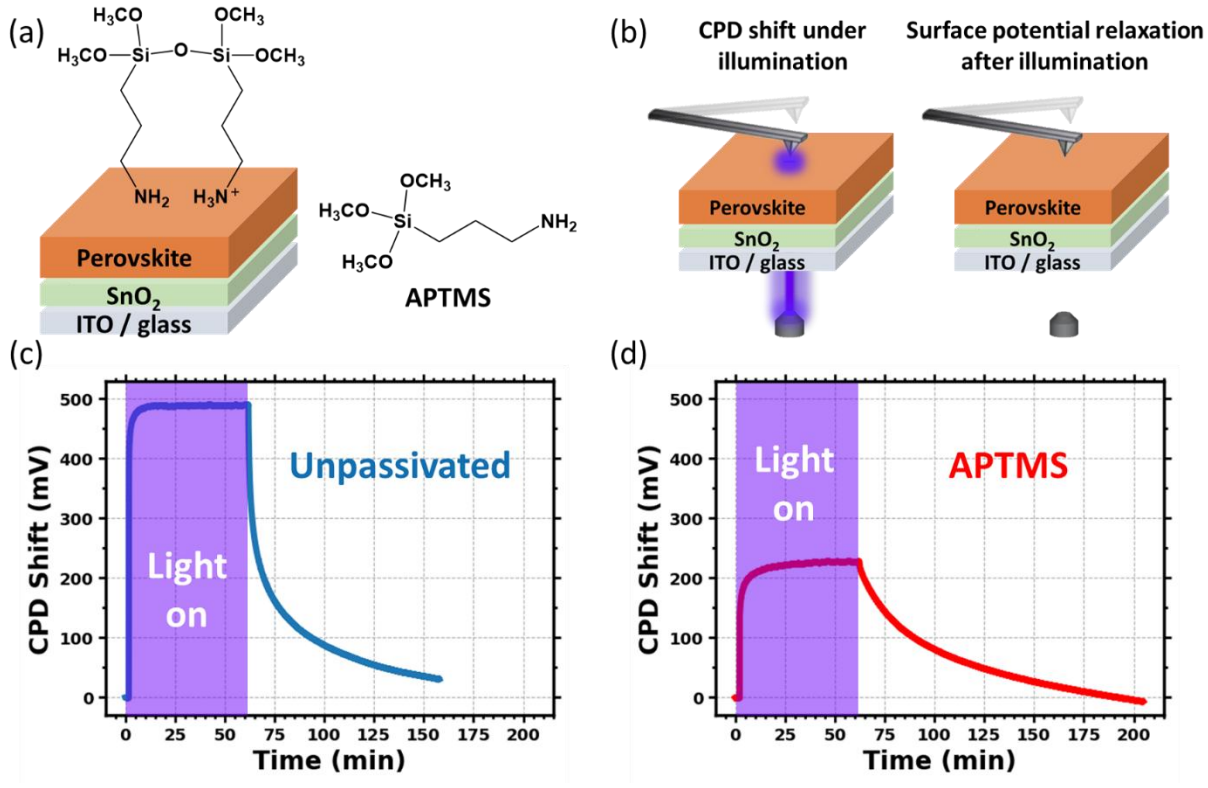

Figure 1. SKPM of unpassivated and APTMS-passivated samples. (a) A schematic diagram of samples and the molecular structure of APTMS surface passivator shown as a monomer (on the right) and polymerized as it is likely to interact with the perovskite (on the top). (b) A simplified SKPM measurement setup on the surface of a sample. CPD shifts as a function of time showing the effects of illumination on CPD evolution and surface potential relaxation following illumination of (c) unpassivated, and (d) APTMS-passivated samples. The illumination source is a 405 nm continuous wave laser, 18 kW m^{-2}, co-aligned with the atomic force microscopy (AFM) tip.

Figure 1c – d compare the CPD shift in unpassivated and APTMS-passivated samples as a function of time during and after illumination. As shown in Figure 1c – d, APTMS surface passivation leads to a smaller CPD shift under illumination, and slower surface potential relaxation after switching off the illumination source. We use a stretched exponential decay function to determine the surface potential relaxation time in unpassivated perovskite to be ~1000 s (~16.7 min) while in APTMS-passivated sample it is ~2550 s (~42.5 min) (see Appendix A and Table S1 for details). We also observe a smaller CPD shift under illumination and slower surface potential relaxation in APTMS-passivated samples at a higher illumination intensity (Figure S5 – 6). Notably, we observe a fast early surface potential relaxation in unpassivated samples at both light intensities which is less pronounced in APTMS-passivated samples.

We propose that the differences in CPD shift magnitude under illumination for the unpassivated and APTMS-treated samples are primarily because of differences in surface charge accumulation, whereas ion motion explains the time-dependence during and after illumination. Prior to illumination, the higher density of surface defects causes a larger surface band bending in unpassivated samples. Upon illumination, the surface defects cause a larger surface charge

accumulation in unpassivated samples which manifest in the higher CPD shifts observed. APTMS surface passivation decreases the density of surface trap states and hence less surface charge accumulation is expected.

One of the major challenges in studying ion motion in halide perovskites is coupled ionic and electronic motion, though studies suggest these processes can be decoupled due to differences in their timescales.[40–42] Electronic motion is reported to occur with a timescale of femtoseconds to microseconds, while ion motion is reported to occur with milliseconds to seconds and longer timescales.[40–42] Surface potential relaxation occurs on a timescale of minutes which is consistent with ion motion. Furthermore, due to the lower activation energy of mobile halides[17,20] and our previous visualization of photo-induced halide migration in hybrid organic-inorganic perovskites,[21] we expect that the dominant mobile ions are halides. Therefore, we attribute surface potential relaxation to halide migration. After illumination, the light source is switched off which allows for halide ions to slowly migrate back towards an equilibrium state. This process is thermodynamically driven by entropy, and kinetically governed by concentration gradients.[14,21,43] Due to higher surface charge accumulation in unpassivated samples, initially the trapped halides migrate back relatively quickly. However, new lower concentration gradients slow down the kinetics over time, as shown in Figure 1c – d and Figure S6. Less surface charge accumulation in APTMS-passivated samples mitigate the early fast surface potential relaxation observed in unpassivated samples and suppress the overall kinetics (see Appendix A for details).

Based on the slower kinetics of APTMS-passivated samples as probed by SKPM, we expect that APTMS-treated samples should also exhibit kinetically suppressed halide phase segregation. To test this, we conduct photoluminescence measurement because hole funneling into lower-bandgap iodide rich domains makes halide phase segregation easily detectable via this method.[14,29] We

monitor the photoluminescence λ_{max} shift under illumination as a function of time (Figure 2). Figure 2 shows that APTMS passivation helps suppress the photoluminescence redshift that occurs under illumination in these samples. We also study the intensity dependence of this process. As shown in Figure 2c, higher illumination intensities cause faster photoluminescence redshifts in both unpassivated and APTMS-passivated samples. However, APTMS-passivated samples exhibit more than 5 times slower photoluminescence redshift. Notably, APTMS-passivated samples undergo slower photoluminescence redshift even at the illumination intensity of 46 kW m^{-2} compared to unpassivated samples at both 23 kW m^{-2} and 46 kW m^{-2}. This observation shows the effectiveness of APTMS passivation in mitigating halide segregation.

Although we cannot completely rule out the possibility of deeply trapped electronic carrier's motion, both SKPM and photoluminescence data show kinetics with timescales on the order of minutes, and the PL shifts are a clear signature of ion migration. Considering the mixed A-site cations in our studied perovskite composition and the possibility of A-site cation phase segregation as reported by different groups,[44–46] we also make pure iodide films with the same ratio of the mixed A-site cations, $FA_{0.8}Cs_{0.2}PbI_3$, and probe photoluminescence of this composition under illumination (Figure S7 – 8). We observed no significant photoluminescence λ_{max} shift, further suggesting that the observed photoluminescence peak shift in the mixed halide samples is due to halide phase separation.

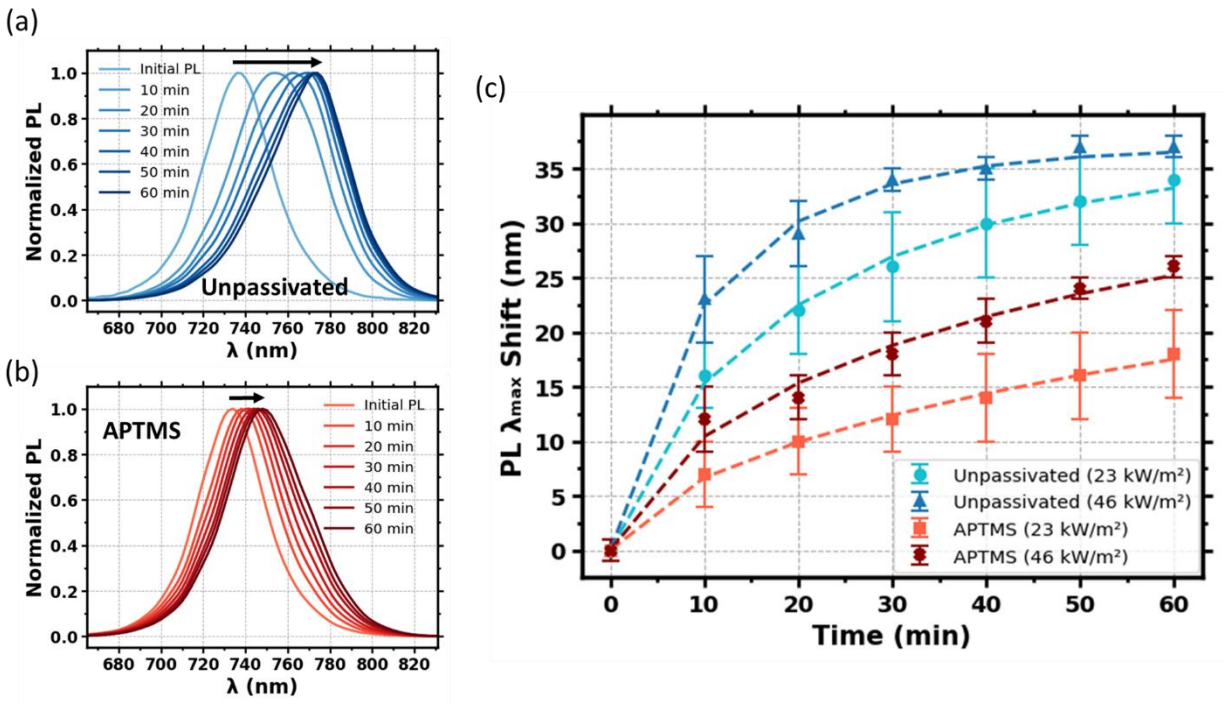

Figure 2. Photoluminescence of unpassivated and APTMS-passivated samples under illumination. Photoluminescence as a function of light soaking time with intensity of 23 kW m^{-2} of (a) unpassivated and (b) APTMS-passivated perovskites. (c) Photoluminescence λ_{max} shift as a function of light soaking time of unpassivated with intensity of 23 kW m^{-2} (light blue), 46 kW m^{-2} (dark blue), and APTMS-passivated perovskites at 23 kW m^{-2} (light red) and 46 kW m^{-2} (dark red). The light source used is a 532 nm continuous wave laser. The dashed lines are the fits for each curve (see Appendix A for details). Error bars are standard error of the mean for three measurements performed on three different films.

As shown in Figure 2a, continuous light soaking under constant intensity exacerbates the halide segregation over time, showing the impact of light soaking time. Similarly, in Figure 3a, we examine the effect of light intensity under constant soaking time. We observe that higher intensities cause more halide segregation. Thus, both light soaking time and intensity are factors that contribute to halide segregation. To compare the impact of these two factors, we plot

photoluminescence λ_{max} shift as a function of light dose (kJ cm^{-2}). Figure 3b shows that within both unpassivated and APTMS-passivated samples, continuous light soaking with the same dose (kJ cm^{-2}) regardless of time/light intensity (23 or 46 kW m^{-2}) causes similar amount of photoluminescence redshift. We also probe the effect of light soaking on light absorption of the perovskite sample and find that light soaking does not affect the light absorption of the sample (Figure S9), likely due to small fraction of the mixed halide phase undergoing halide phase segregation which may not be as easily detectable via absorption measurements.[47]

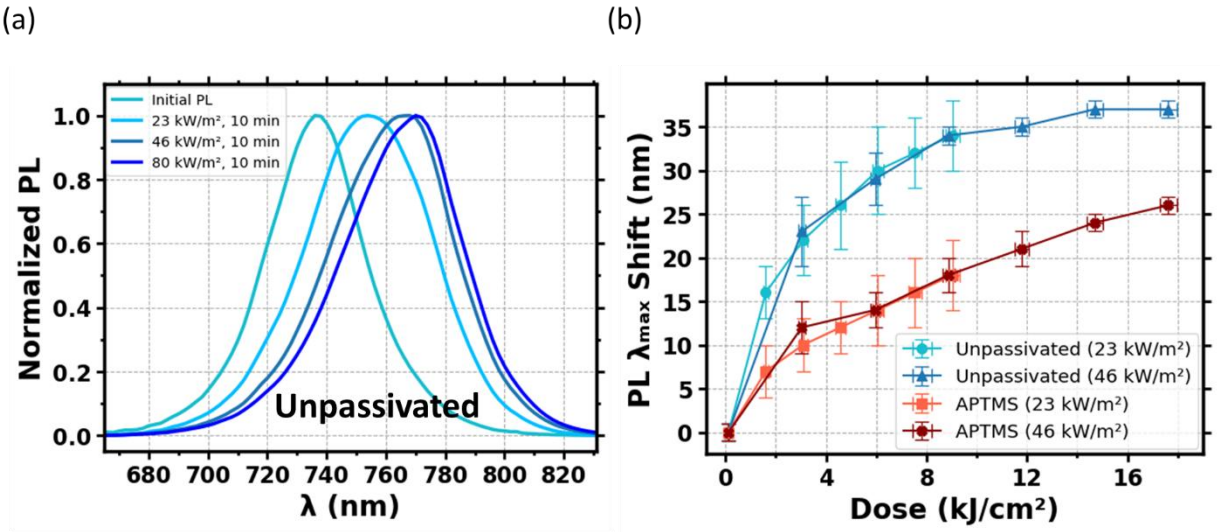

Figure 3. Effect of light soaking time and intensity on halide segregation. (a) Photoluminescence of unpassivated perovskites as a function of light intensity with constant light soaking time of 10 min. (b) Photoluminescence λ_{max} shift as a function of light dose (kJ cm^{-2}) of unpassivated with light intensity of 23 kW m^{-2} (light blue), 46 kW m^{-2} (dark blue), and APTMS-passivated perovskites at 23 kW m^{-2} (light red) and 46 kW m^{-2} (dark red).

Our findings in Figure 3 suggest that photoinduced halide segregation follows first order kinetics, with halide segregation dependent on light dose (kJ/cm^2), expressed in reaction 1 below (as a limiting case).

$$5FA_{0.8}Cs_{0.2}Pb(I_{0.8}Br_{0.2})_3 + h\nu \rightleftharpoons 4FA_{0.8}Cs_{0.2}PbI_3 + FA_{0.8}Cs_{0.2}PbBr_3 \quad (1)$$

This shows that when examining photoinduced halide segregation, special attention should be given to the light dose (the product of light intensity and time), as both light intensity and time contribute to photoinduced halide segregation.

2.4 Conclusions

In summary, we report that APTMS, applied as a surface passivator, kinetically suppresses halide migration in $FA_{0.8}Cs_{0.2}Pb(I_{0.8}Br_{0.2})_3$, a wide bandgap perovskite (E_g of 1.69 eV). We conduct SKPM to show that APTMS surface passivation kinetically suppresses halide relaxation in the dark after illumination. Using photoluminescence, we investigate the kinetic effects of APTMS surface passivation on halide phase segregation and show that APTMS-passivated samples exhibit more than 5 times slower halide segregation. Lastly, we report that halide segregation follows first order kinetics dependent on light dose (kJ/cm^2), where the same light dose leads to the same extent of halide segregation regardless of time/light intensity. This study shows that passivating surface defects has more implications beyond reducing electronic carrier recombination rates, and provides evidence for kinetic suppression of photoinduced halide migration which is a crucial topic for improving efficiency and stability of perovskites.

2.5 Acknowledgements

This paper is based primarily on work supported by the U.S. Department of Energy (DOE-SC0013957). The authors acknowledge the use of facilities and instruments at the Photonics Research Center (PRC) at the Department of Chemistry, University of Washington, as well as that at the Research Training Testbed (RTT), part of the Washington Clean Energy Testbeds system. Part of this work is conducted at the Molecular Analysis Facility, a National

Nanotechnology Coordinated Infrastructure site at the University of Washington which is supported in part by funds from the National Science Foundation (awards NNCI-2025489, NNCI-1542101), the Molecular Engineering & Sciences Institute, and the Clean Energy Institute. We acknowledge Dr. Tanka R. Rana and Prof. J. Devin MacKenzie from the University of Washington for providing the commercial SnO_2 solution. D.S.G. acknowledges salary and infrastructure support from the Washington Research Foundation, the Alvin L. and Verla R. Kwiram Endowment, and the B. Seymour Rabinovitch Endowment.

2.6 References

(1) Jena, A. K.; Kulkarni, A.; Miyasaka, T. Halide Perovskite Photovoltaics: Background, Status, and Future Prospects. *Chem. Rev.* **2019**, *119* (5), 3036–3103. https://doi.org/10.1021/acs.chemrev.8b00539.

(2) Wang, R.; Huang, T.; Xue, J.; Tong, J.; Zhu, K.; Yang, Y. Prospects for Metal Halide Perovskite-Based Tandem Solar Cells. *Nat. Photonics* **2021**, *15* (6), 411–425. https://doi.org/10.1038/s41566-021-00809-8.

(3) Liu, X.-K.; Xu, W.; Bai, S.; Jin, Y.; Wang, J.; Friend, R. H.; Gao, F. Metal Halide Perovskites for Light-Emitting Diodes. *Nat. Mater.* **2021**, *20* (1), 10–21. https://doi.org/10.1038/s41563-020-0784-7.

(4) Veeramalai, C. P.; Feng, S.; Zhang, X.; Pammi, S. V. N.; Pecunia, V.; Li, C. Lead–Halide Perovskites for next-Generation Self-Powered Photodetectors: A Comprehensive Review. *Photon. Res., PRJ* **2021**, *9* (6), 968–991. https://doi.org/10.1364/PRJ.418450.

(5) Utzat, H.; Sun, W.; Kaplan, A. E. K.; Krieg, F.; Ginterseder, M.; Spokoyny, B.; Klein, N. D.; Shulenberger, K. E.; Perkinson, C. F.; Kovalenko, M. V.; Bawendi, M. G. Coherent Single-Photon Emission from Colloidal Lead Halide Perovskite Quantum Dots. *Science* **2019**, *363* (6431), 1068–1072. https://doi.org/10.1126/science.aau7392.

(6) *Interactive Best Research-Cell Efficiency Chart*. https://www.nrel.gov/pv/interactive-cell-efficiency.html (accessed 2023-07-19).

(7) Schulz, P.; Cahen, D.; Kahn, A. Halide Perovskites: Is It All about the Interfaces? *Chem. Rev.* **2019**, *119* (5), 3349–3417. https://doi.org/10.1021/acs.chemrev.8b00558.

(8) deQuilettes, D. W.; Koch, S.; Burke, S.; Paranji, R. K.; Shropshire, A. J.; Ziffer, M. E.; Ginger, D. S. Photoluminescence Lifetimes Exceeding 8 Ms and Quantum Yields Exceeding 30% in Hybrid Perovskite Thin Films by Ligand Passivation. *ACS Energy Lett.* **2016**, *1* (2), 438–444. https://doi.org/10.1021/acsenergylett.6b00236.

(9) Ono, L. K.; Liu, S. (Frank); Qi, Y. Reducing Detrimental Defects for High-Performance Metal Halide Perovskite Solar Cells. *Angewandte Chemie International Edition* **2020**, *59* (17), 6676–6698. https://doi.org/10.1002/anie.201905521.

(10) Wu, W.-Q.; Rudd, P. N.; Ni, Z.; Van Brackle, C. H.; Wei, H.; Wang, Q.; Ecker, B. R.; Gao, Y.; Huang, J. Reducing Surface Halide Deficiency for Efficient and Stable Iodide-Based Perovskite Solar Cells. *J. Am. Chem. Soc.* **2020**, *142* (8), 3989–3996. https://doi.org/10.1021/jacs.9b13418.

(11) Jariwala, S.; Burke, S.; Dunfield, S.; Shallcross, R. C.; Taddei, M.; Wang, J.; Eperon, G. E.; Armstrong, N. R.; Berry, J. J.; Ginger, D. S. Reducing Surface Recombination Velocity of Methylammonium-Free Mixed-Cation Mixed-Halide Perovskites via Surface Passivation. *Chem. Mater.* **2021**, *3* (13), 5035–5044. https://doi.org/10.1021/acs.chemmater.1c00848.

(12) Braly, I. L.; Stoddard, R. J.; Rajagopal, A.; Uhl, A. R.; Katahara, J. K.; Jen, A. K.-Y.; Hillhouse, H. W. Current-Induced Phase Segregation in Mixed Halide Hybrid Perovskites and Its Impact on Two-Terminal Tandem Solar Cell Design. *ACS Energy Lett.* **2017**, *2* (8), 1841–1847. https://doi.org/10.1021/acsenergylett.7b00525.

(13) Samu, G. F.; Janáky, C.; Kamat, P. V. A Victim of Halide Ion Segregation. How Light Soaking Affects Solar Cell Performance of Mixed Halide Lead Perovskites. *ACS Energy Lett.* **2017**, *2* (8), 1860–1861. https://doi.org/10.1021/acsenergylett.7b00589.

(14) DuBose, J. T.; Kamat, P. V. Hole Trapping in Halide Perovskites Induces Phase Segregation. *Acc. Mater. Res.* **2022**. https://doi.org/10.1021/accountsmr.2c00076.

(15) Vashishtha, P.; Halpert, J. E. Field-Driven Ion Migration and Color Instability in Red-Emitting Mixed Halide Perovskite Nanocrystal Light-Emitting Diodes. *Chem. Mater.* **2017**, *29* (14), 5965–5973. https://doi.org/10.1021/acs.chemmater.7b01609.

(16) Nah, Y.; Allam, O.; Kim, H. S.; Choi, J. I.; Kim, I. S.; Byun, J.; Kim, S. O.; Jang, S. S.; Kim, D. H. Spectral Instability of Layered Mixed Halide Perovskites Results from Anion

Phase Redistribution and Selective Hole Injection. *ACS Nano* **2021**, *15* (1), 1486–1496. https://doi.org/10.1021/acsnano.0c08897.

(17) Eames, C.; Frost, J. M.; Barnes, P. R. F.; O'Regan, B. C.; Walsh, A.; Islam, M. S. Ionic Transport in Hybrid Lead Iodide Perovskite Solar Cells. *Nature Communications* **2015**, *6* (1), 7497. https://doi.org/10.1038/ncomms8497.

(18) Yoon, S. J.; Kuno, M.; Kamat, P. V. Shift Happens. How Halide Ion Defects Influence Photoinduced Segregation in Mixed Halide Perovskites. *ACS Energy Lett.* **2017**, *2* (7), 1507–1514. https://doi.org/10.1021/acsenergylett.7b00357.

(19) Meggiolaro, D.; Mosconi, E.; De Angelis, F. Formation of Surface Defects Dominates Ion Migration in Lead-Halide Perovskites. *ACS Energy Lett.* **2019**, *4* (3), 779–785. https://doi.org/10.1021/acsenergylett.9b00247.

(20) Yuan, Y.; Huang, J. Ion Migration in Organometal Trihalide Perovskite and Its Impact on Photovoltaic Efficiency and Stability. *Acc. Chem. Res.* **2016**, *49* (2), 286–293. https://doi.org/10.1021/acs.accounts.5b00420.

(21) deQuilettes, D. W.; Zhang, W.; Burlakov, V. M.; Graham, D. J.; Leijtens, T.; Osherov, A.; Bulović, V.; Snaith, H. J.; Ginger, D. S.; Stranks, S. D. Photo-Induced Halide Redistribution in Organic–Inorganic Perovskite Films. *Nat Commun* **2016**, *7* (1), 11683. https://doi.org/10.1038/ncomms11683.

(22) McMeekin, D. P.; Sadoughi, G.; Rehman, W.; Eperon, G. E.; Saliba, M.; Hörantner, M. T.; Haghighirad, A.; Sakai, N.; Korte, L.; Rech, B.; Johnston, M. B.; Herz, L. M.; Snaith, H. J. A Mixed-Cation Lead Mixed-Halide Perovskite Absorber for Tandem Solar Cells. *Science* **2016**, *351* (6269), 151–155. https://doi.org/10.1126/science.aad5845.

(23) Tao, L.; Qiu, J.; Sun, B.; Wang, X.; Ran, X.; Song, L.; Shi, W.; Zhong, Q.; Li, P.; Zhang, H.; Xia, Y.; Müller-Buschbaum, P.; Chen, Y. Stability of Mixed-Halide Wide Bandgap Perovskite Solar Cells: Strategies and Progress. *Journal of Energy Chemistry* **2021**, *61*, 395–415. https://doi.org/10.1016/j.jechem.2021.03.038.

(24) Tan, S.; Huang, T.; Yang, Y. Defect Passivation of Perovskites in High Efficiency Solar Cells. *J. Phys. Energy* **2021**, *3* (4), 042003. https://doi.org/10.1088/2515-7655/ac2e13.

(25) Zuo, L.; Guo, H.; deQuilettes, D. W.; Jariwala, S.; Marco, N. D.; Dong, S.; DeBlock, R.; Ginger, D. S.; Dunn, B.; Wang, M.; Yang, Y. Polymer-Modified Halide Perovskite Films for Efficient and Stable Planar Heterojunction Solar Cells. *Science Advances* **2017**, *3* (8), e1700106. https://doi.org/10.1126/sciadv.1700106.

(26) Huang, J.; Yuan, Y.; Shao, Y.; Yan, Y. Understanding the Physical Properties of Hybrid Perovskites for Photovoltaic Applications. *Nat Rev Mater* **2017**, *2* (7), 1–19. https://doi.org/10.1038/natrevmats.2017.42.

(27) Niu, T.; Lu, J.; Munir, R.; Li, J.; Barrit, D.; Zhang, X.; Hu, H.; Yang, Z.; Amassian, A.; Zhao, K.; Liu, S. (Frank). Stable High-Performance Perovskite Solar Cells via Grain Boundary Passivation. *Advanced Materials* **2018**, *30* (16), 1706576. https://doi.org/10.1002/adma.201706576.

(28) Bischak, C. G.; Hetherington, C. L.; Wu, H.; Aloni, S.; Ogletree, D. F.; Limmer, D. T.; Ginsberg, N. S. Origin of Reversible Photoinduced Phase Separation in Hybrid Perovskites. *Nano Lett.* **2017**, *17* (2), 1028–1033. https://doi.org/10.1021/acs.nanolett.6b04453.

(29) Hoke, E. T.; Slotcavage, D. J.; Dohner, E. R.; Bowring, A. R.; Karunadasa, H. I.; McGehee, M. D. Reversible Photo-Induced Trap Formation in Mixed-Halide Hybrid Perovskites for Photovoltaics. *Chem. Sci.* **2014**, *6* (1), 613–617. https://doi.org/10.1039/C4SC03141E.

(30) Bush, K. A.; Frohna, K.; Prasanna, R.; Beal, R. E.; Leijtens, T.; Swifter, S. A.; McGehee, M. D. Compositional Engineering for Efficient Wide Band Gap Perovskites with Improved Stability to Photoinduced Phase Segregation. *ACS Energy Lett.* **2018**, *3* (2), 428–435. https://doi.org/10.1021/acsenergylett.7b01255.

(31) Birkhold, S. T.; Precht, J. T.; Giridharagopal, R.; Eperon, G. E.; Schmidt-Mende, L.; Ginger, D. S. Direct Observation and Quantitative Analysis of Mobile Frenkel Defects in Metal Halide Perovskites Using Scanning Kelvin Probe Microscopy. *J. Phys. Chem. C* **2018**, *122* (24), 12633–12639. https://doi.org/10.1021/acs.jpcc.8b03255.

(32) Kamat, P. V.; Kuno, M. Halide Ion Migration in Perovskite Nanocrystals and Nanostructures. *Acc. Chem. Res.* **2021**, *54* (3), 520–531. https://doi.org/10.1021/acs.accounts.0c00749.

(33) Garrett, J. L.; Tennyson, E. M.; Hu, M.; Huang, J.; Munday, J. N.; Leite, M. S. Real-Time Nanoscale Open-Circuit Voltage Dynamics of Perovskite Solar Cells. *Nano Lett.* **2017**, *17* (4), 2554–2560. https://doi.org/10.1021/acs.nanolett.7b00289.

(34) Belisle, R. A.; Bush, K. A.; Bertoluzzi, L.; Gold-Parker, A.; Toney, M. F.; McGehee, M. D. Impact of Surfaces on Photoinduced Halide Segregation in Mixed-Halide Perovskites. *ACS Energy Lett.* **2018**, *3* (11), 2694–2700. https://doi.org/10.1021/acsenergylett.8b01562.

(35) Balakrishna, R. G.; Kobosko, S. M.; Kamat, P. V. Mixed Halide Perovskite Solar Cells. Consequence of Iodide Treatment on Phase Segregation Recovery. *ACS Energy Lett.* **2018**, *3* (9), 2267–2272. https://doi.org/10.1021/acsenergylett.8b01450.

(36) Lim, V. J.-Y.; Knight, A. J.; Oliver, R. D. J.; Snaith, H. J.; Johnston, M. B.; Herz, L. M. Impact of Hole-Transport Layer and Interface Passivation on Halide Segregation in Mixed-Halide Perovskites. *Advanced Functional Materials* **2022**, *32* (41), 2204825. https://doi.org/10.1002/adfm.202204825.

(37) Shi, Y.; Rojas-Gatjens, E.; Wang, J.; Pothoof, J.; Giridharagopal, R.; Ho, K.; Jiang, F.; Taddei, M.; Yang, Z.; Sanehira, E. M.; Irwin, M. D.; Silva-Acuña, C.; Ginger, D. S. (3-Aminopropyl)Trimethoxysilane Surface Passivation Improves Perovskite Solar Cell Performance by Reducing Surface Recombination Velocity. *ACS Energy Lett.* **2022**, *7* (11), 4081–4088. https://doi.org/10.1021/acsenergylett.2c01766.

(38) Pothoof, J.; Westbrook, R. J. E.; Giridharagopal, R.; Breshears, M. D.; Ginger, D. S. Surface Passivation Suppresses Local Ion Motion in Halide Perovskites. *J. Phys. Chem. Lett.* **2023**, *14* (26), 6092–6098. https://doi.org/10.1021/acs.jpclett.3c01089.

(39) Jariwala, S.; Kumar, R. E.; Eperon, G. E.; Shi, Y.; Fenning, D. P.; Ginger, D. S. Dimethylammonium Addition to Halide Perovskite Precursor Increases Vertical and Lateral Heterogeneity. *ACS Energy Lett.* **2021**, 204–210. https://doi.org/10.1021/acsenergylett.1c02302.

(40) Herz, L. M. Charge-Carrier Mobilities in Metal Halide Perovskites: Fundamental Mechanisms and Limits. *ACS Energy Lett.* **2017**, *2* (7), 1539–1548. https://doi.org/10.1021/acsenergylett.7b00276.

(41) Toth, D.; Hailegnaw, B.; Richheimer, F.; Castro, F. A.; Kienberger, F.; Scharber, M. C.; Wood, S.; Gramse, G. Nanoscale Charge Accumulation and Its Effect on Carrier Dynamics in Tri-Cation Perovskite Structures. *ACS Appl. Mater. Interfaces* **2020**, *12* (42), 48057–48066. https://doi.org/10.1021/acsami.0c10641.

(42) Saketh Chandra, T.; Singareddy, A.; Hossain, K.; Sivadas, D.; Bhatia, S.; Singh, S.; Kabra, D.; Nair, P. R. Ion Mobility Independent Large Signal Switching of Perovskite Devices. *Appl. Phys. Lett.* **2021**, *119* (2), 023506. https://doi.org/10.1063/5.0051342.

(43) Kerner, R. A.; Xu, Z.; Larson, B. W.; Rand, B. P. The Role of Halide Oxidation in Perovskite Halide Phase Separation. *Joule* **2021**, *5* (9), 2273–2295. https://doi.org/10.1016/j.joule.2021.07.011.

(44) Chatterjee, R.; Pavlovetc, I. M.; Aleshire, K.; Hartland, G. V.; Kuno, M. Subdiffraction Infrared Imaging of Mixed Cation Perovskites: Probing Local Cation Heterogeneities. *ACS Energy Lett.* **2018**, *3* (2), 469–475. https://doi.org/10.1021/acsenergylett.7b01306.

(45) Liu, L.; Lu, J.; Wang, H.; Cui, Z.; Giorgi, G.; Bai, Y.; Chen, Q. A-Site Phase Segregation in Mixed Cation Perovskite. *Materials Reports: Energy* **2021**, *1* (4), 100064. https://doi.org/10.1016/j.matre.2021.100064.

(46) Kubicki, D. J.; Prochowicz, D.; Hofstetter, A.; Zakeeruddin, S. M.; Grätzel, M.; Emsley, L. Phase Segregation in Potassium-Doped Lead Halide Perovskites from 39K Solid-State NMR at 21.1 T. *J. Am. Chem. Soc.* **2018**, *140* (23), 7232–7238. https://doi.org/10.1021/jacs.8b03191.

(47) Mahesh, S.; M. Ball, J.; J. Oliver, R. D.; P. McMeekin, D.; K. Nayak, P.; B. Johnston, M.; J. Snaith, H. Revealing the Origin of Voltage Loss in Mixed-Halide Perovskite Solar Cells. *Energy & Environmental Science* **2020**, *13* (1), 258–267. https://doi.org/10.1039/C9EE02162K.

Chapter 3: Surface Passivation for Halide Optoelectronics: Comparing Optimization and Reactivity of Amino-Silanes with Formamidinium

Adapted from Huang, Z.;† **Akrami, F.**;† Zhang, J.; Barlow, S.; Marder, S. R.; Ginger, D. S. Surface Passivation for Halide Optoelectronics: Comparing Optimization and Reactivity of Amino-Silanes with Formamidinium. *J. Am. Chem. Soc.* **2025**, *147* (46), 42918–42925. https://doi.org/10.1021/jacs.5c15574.

† Z. Huang and **F. Akrami** contributed equally to this work.

My contributions to this project include leading the optimization of aminosilane surface passivation; contributing to early discussions about incorporating nuclear magnetic resonance spectroscopy into the study; performing time-resolved photoluminescence, UV-Vis absorption, X-ray diffraction, and atomic force microscopy measurements; analyzing solar cell data and generating the corresponding figures and tables (with device measurements conducted by Z. Huang); and writing the original draft with active involvement in subsequent editing and revision.

3.1 Overview

Amino-silane-based surface passivation schemes are gaining attention in halide perovskite optoelectronics, with varying levels of success. We compare surface treatments using (3-aminopropyl)trimethoxysilane (APTMS) and [3-(2-aminoethylamino)propyl]trimethoxysilane (AEAPTMS), applied via room-temperature vacuum deposition, to the perovskite $FA_{0.78}Cs_{0.22}Pb(I_{0.85}Br_{0.15})_3$ (FA = formamidinium). Both molecules improve thin-film photoluminescence properties and photovoltaic device performance, although their effectiveness depends strongly on deposition time. We show AEAPTMS has a wider, more robust processing window and yields higher performance under optimized conditions. In contrast, over-exposure, particularly with APTMS, reduces performance, with notable reductions in photoluminescence lifetime and absorbance. To probe the underlying chemistry, we employ nuclear magnetic resonance (NMR) spectroscopy and depth-resolved time-of-flight secondary ion mass spectrometry (ToF-SIMS), demonstrating that both amino-silanes react with formamidinium (FA^+)

cations in solution and in the solid state. This work underscores the importance of optimizing deposition conditions to balance effective passivation with potential performance loss and elucidates previously unrecognized reactive chemistry between amino-silane passivating agents and halide perovskites.

3.2 Introduction

Metal halide perovskites are semiconductors with the general formula of ABX_3 where A is a monovalent cation (typically methylammonium (MA^+), formamidinium (FA^+), or Cs^+), B is a divalent cation (typically Pb^{2+} or Sn^{2+}), and X is a halide anion (I^-, Br^-, or Cl^-).[1,2] These materials have attracted much attention for their versatility and performance across a wide range of applications, including photovoltaics, light-emitting diodes, photodetectors, and even single photon sources.[3–11]

While halide perovskites are widely described as defect tolerant, like all semiconductors they exhibit a variety of bulk and surface defects.[12–16] In perovskites these defects contribute to detrimental processes ranging from non-radiative recombination[15,17] to ion migration, phase-separation, and instability.[3,18–23] Mitigating these defects, particularly unpassivated surface states, is essential for enhancing the performance of perovskite semiconductors in applications from tandem solar cells to light-emitting applications.[13,21,24–27] Furthermore removing such defects can significantly enhance both material and device stability.

Numerous studies have demonstrated effective surface passivation strategies that reduce nonradiative recombination in perovskite films and enhance solar cell performance.[15,17,28–32] Early interface passivators were often Lewis bases which can bind halide vacancies,[12] however the lability of many simple Lewis bases makes them suitable for surface chemistry studies, but less

suitable for scalable device fabrication. Several years ago, looking for passivators that were widely scalable, cross-linkable (to provide more robust coatings), and able to interact with the perovskite, our group began exploring silanes, which are widely available in bulk quantities due to their use as adhesion promoters in the glass industry,[33] and are compatible with large area low cost coating methods such as low pressure vapor deposition at ambient temperatures. Notably, these studies, and those by other groups, found that cross-linkable amino-silanes are effective as scalable surface passivators in both films and complete devices, with reports of enhanced photoluminescence properties[15,34] and corresponding improvements in open-circuit voltage,[28,34] suppression of voltage-induced ion migration,[20] decreased photoinduced halide segregation,[19] and even improved device stability under full-spectrum sunlight at 85 °C and open-circuit conditions in ambient air.[34] They also found that amino-silanes were able to passivate perovskites that were not well-passivated by other simple Lewis base treatments.[15]

While early studies often focused on (3-aminopropyl)trimethoxysilane (APTMS), Lin et al. recently compared a series of amine-functionalized silanes, reporting that [3-(2-aminoethylamino)propyl]trimethoxysilane (AEAPTMS) yielded superior device performance and stability. While APTMS contains a single primary amine, AEAPTMS contains neighboring primary and secondary amines. Based on density functional theory (DFT) calculations, Lin et al. proposed that AEAPTMS passivates more favorably by binding to undercoordinated Pb^{2+} cations in a cooperative fashion. Interestingly, they also reported that APTMS passivation decreased cell performance, in apparent contradiction to a number of previous reports.[15,19,20,28,35]

In this work, we study the effect of time-optimized, vapor-deposited surface treatments with APTMS and AEAPTMS on a $FA_{0.78}Cs_{0.22}Pb(I_{0.85}Br_{0.15})_3$ perovskite with a bandgap of 1.66 eV. We used this perovskite formulation due to its reported stability and its suitability as a top absorber

layer in perovskite–silicon tandem solar cells.[3,36–39] Using time-resolved photoluminescence (TRPL), we show that both APTMS and AEAPTMS treatments increase carrier lifetimes, as well as open-circuit voltage and power-conversion efficiency of solar cells. We show that the overall effectiveness of the passivation varies with deposition time (silane coating thickness) and that the optimal conditions differ not only between APTMS and AEPTMS but also depending on if we optimize for maximum PL lifetime, or maximum device performance. Finally, we show that both APTMS and AEAPTMS react with FA^+ cations, challenging some current models for surface binding.[34]

3.3 Results and Discussion

We synthesized $FA_{0.78}Cs_{0.22}Pb(I_{0.85}Br_{0.15})_3$ perovskites by adapting previously reported procedures,[36] (see Supporting Information (SI) for details). We measure a bandgap of ~1.66 eV via UV-Vis spectroscopy (Appendix B, Figure S1). For all surface treatments, we deposit both APTMS and AEAPTMS using low pressure vacuum deposition (see SI). Vapor deposition at reduced pressure is scalable, favors deposition of the silane monomer, and offers improved reproducibility.[40] We also find it reduces pooling of liquid silane derivative on the perovskite surface, thus reducing the prospects for etching. Figure 1a shows the molecular structures of APTMS and AEAPTMS.

First, we investigate the effects of time-dependent APTMS and AEAPTMS treatments on TRPL and UV-Vis absorbance (Figure 1b-e). Figures 1b and 1c show that for deposition times of 30 s, 90 s, and 360 s, at room temperature with gauge pressure of about -25 in. of Hg relative to atmospheric pressure, both APTMS and AEAPTMS treatments extend TRPL lifetimes compared

to the unpassivated sample. Table S1 summarizes fitting parameters for the stretched exponential decay of TRPL data.

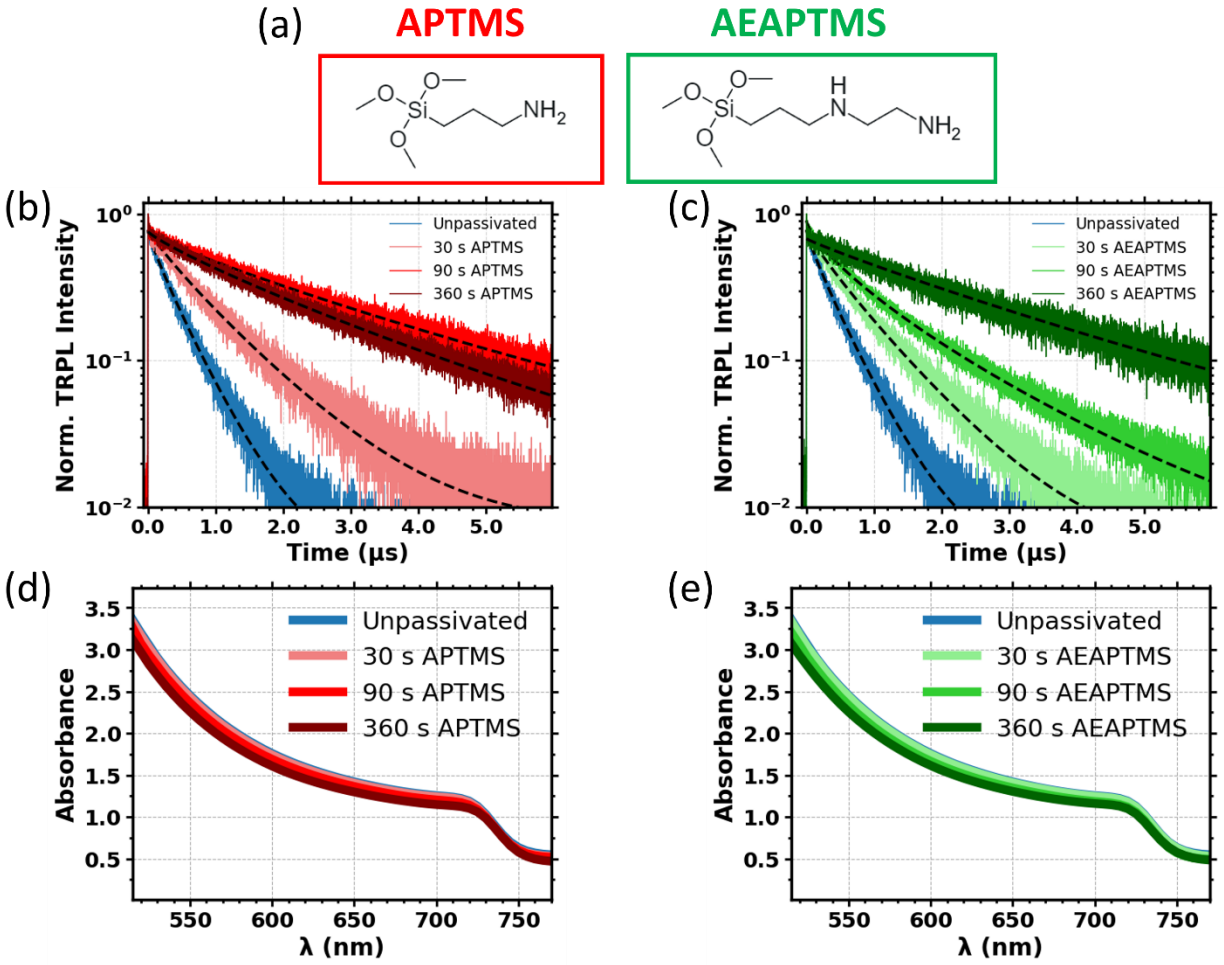

Figure 1. Deposition time-dependent surface treatment of $FA_{0.78}Cs_{0.22}Pb(I_{0.85}Br_{0.15})_3$ perovskites with APTMS and AEAPTMS. (a) Molecular structures of APTMS (red) and AEAPTMS (green). (b) and (c) TRPL decay curves of unpassivated (blue), APTMS-passivated (red), and AEAPTMS-passivated (green) samples with varying deposition times. Black dashed lines are stretched exponential fits to the data. (d) and (e) UV-Vis absorbance spectra of unpassivated (blue), APTMS-passivated (red), and AEAPTMS-passivated (green) samples with varying deposition times.

We observe that longer amino-silane deposition times generally result in successively longer TRPL lifetimes, except for the longest (360 s) APTMS treatment, which does not show an increased lifetime relative to the 90 s APTMS treatment. Notably, we achieve similar TRPL enhancements with both APTMS and AEAPTMS, though at different optimum deposition times (see Table S1). UV-Vis spectra in Figure 1d and 1e show a small but measurable decline in extinction with increasing deposition time for both studied silanes. The X-ray diffraction (XRD) patterns (Appendix B, Figure S2) of the untreated and treated samples across the same deposition time range show a subtle reduction in peak intensities at higher treatment times, indicating little to no bulk structural changes. We further perform atomic force microscopy (AFM) topography and phase imaging to probe nanoscale surface features (Appendix B, Figure S3-S5).

Next, we examine the incorporation of APTMS and AEAPTMS surface treatments into archetypal p–i–n structured perovskite solar cells. Figure 2a shows the detailed schematic of the device architecture. This commonly used architecture comprises an ITO electrode treated with [2-(3,6-dimethoxy-9*H*-carbazol-9-yl)ethyl]phosphonic acid (MeO-2PACz) as the hole-transport layer, evaporated C_{60} as the electron-transport layer, and Ag as the back electrode. Each of these layers is currently widely used and known to yield well-performing devices.[38,41–44]

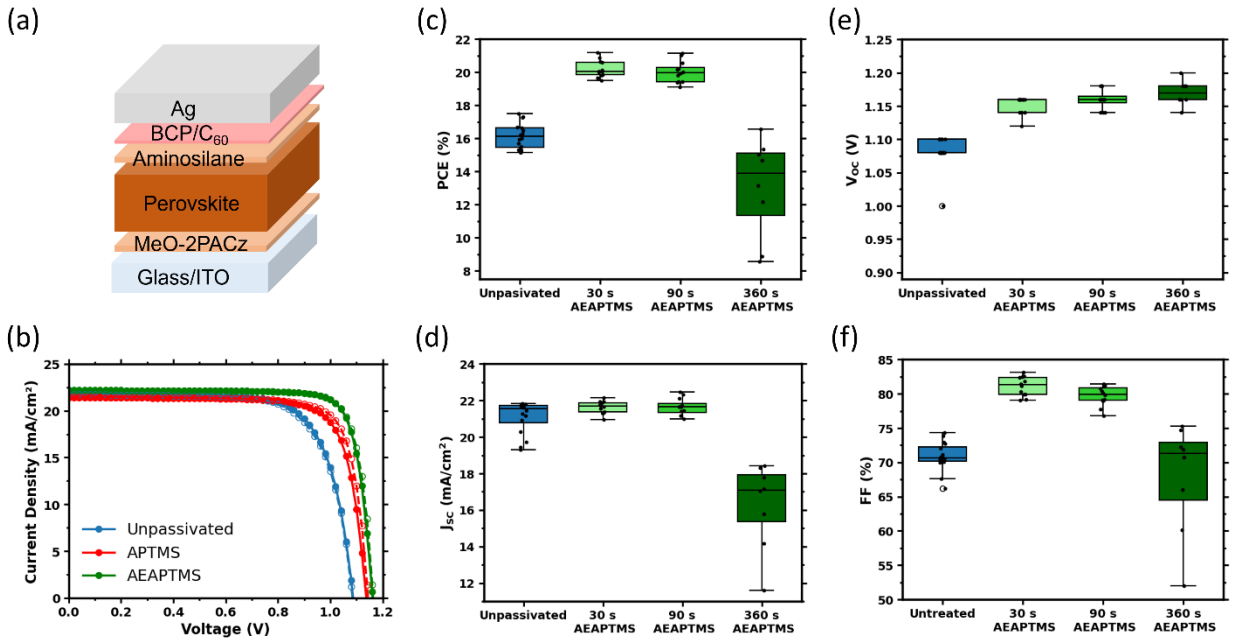

Figure 2. Perovskite solar-cell performance with deposition time-dependent amino-silane surface treatments. (a) A schematic illustration of the p–i–n structured perovskite solar cell. (b) J-V curves of the champion unpassivated (blue), APTMS-treated (red), and AEAPTMS-treated (green) devices with 30 s treatment duration. Solid lines represent forward scans and dotted lines represent reverse scans. (c) Power conversion efficiency (PCE), (d) short-circuit current density (J_{SC}), (e) open-circuit voltage (V_{OC}), and (f) fill factor (FF) of unpassivated (blue) and AEAPTMS-treated (green) devices with varying deposition times (based on forward scans).

We observe that longer amino-silane deposition times eventually lead to a decline in solar cell performance (Figures 2c–f and Appendix B, S6), and we find the optimal performance (Figure 2b) occurs with shorter treatment durations (~30 s). Under optimized treatment conditions, both APTMS- and AEAPTMS-treated devices show improved power conversion efficiencies, most notably through enhanced open-circuit voltage (V_{OC}) and fill factor (FF). Among the two treatments, AEAPTMS-treated solar cells demonstrate the highest overall efficiency. Table S2 summarizes the mean values and standard deviations of the device data. It is noteworthy that,

consistent with the trend of increased TRPL lifetimes at longer amino-silane deposition times (Figure 1b-c), the V_{OC} also tends to improve with extended treatment durations. This result is widely consistent with past data on amino-silane treatment of perovskites.[28,34]

However, despite the V_{OC} improvements, we observe a decrease in J_{SC}, FF, and PCE at longer deposition times. We attribute this trade-off to a combination of perovskite decomposition and, more significantly, the insulating nature of the amino-silanes,[28] which becomes more detrimental as thicker layers provide a greater barrier to charge extraction after prolonged deposition. Furthermore, at even longer deposition times (Appendix B, Figures S7-S8), or under more aggressive conditions,[34] some reduction in the 3D perovskite phase occurs as evidenced by the concomitant decrease in UV-Vis absorbance and XRD peak intensities. In our system, we observe a similar decrease in the XRD peak intensities supporting this loss trend. Overall, these findings highlight a tunable balance between beneficial surface modification and adverse effects, namely electrical insulation and decomposition, which is sensitive to treatment duration and conditions.

On one hand, these observations are consistent with previous work assigning the beneficial effects of amino-silane treatment to the passivation of surface defects, through processes such as coordination of the Lewis basic amine groups to Pb^{2+} sites with surface halide vacancies.[15,28,34] On the other hand, our group and others have reported enhanced performance in amine-based passivation strategies where we have conclusively demonstrated that the amine groups react with the FA^{+} cations.[45–47] Therefore, to better understand how these two amino-silanes interact differently with the perovskite, we monitored the interaction between AEAPTMS and FAI in DMSO-d_6 (0.04 M) by solution ^{1}H NMR spectroscopy.

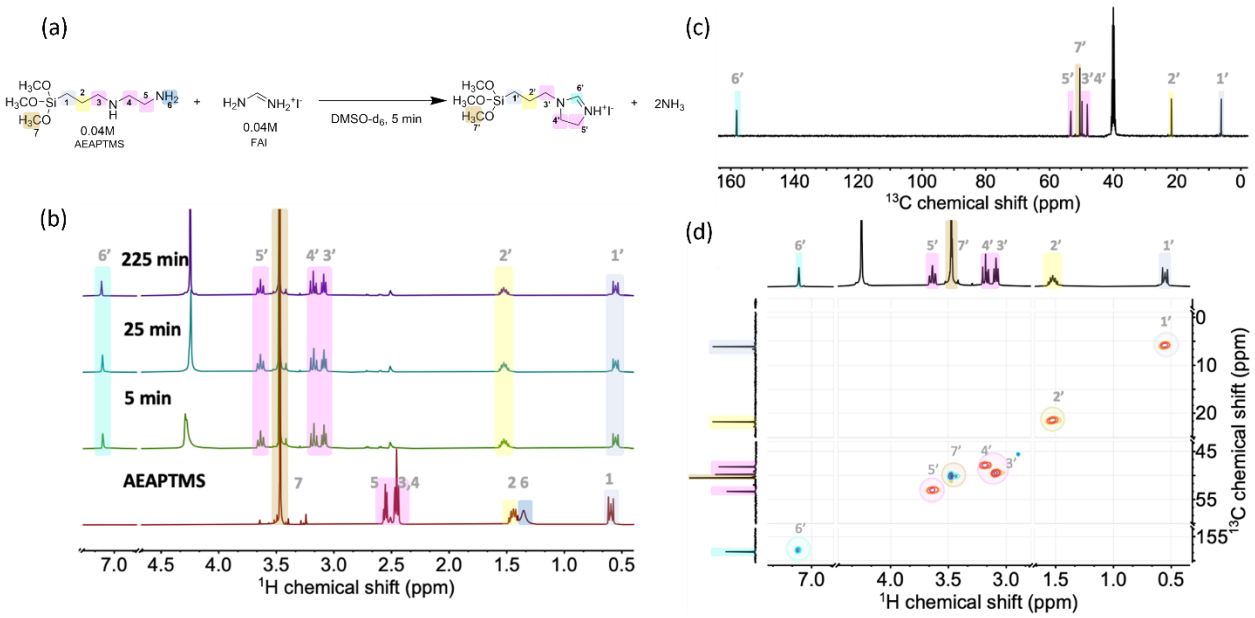

Figure 3. (a) Overall reaction between AEAPTMS and FAI, (b) ^{1}H NMR spectra of AEAPTMS in DMSO-d_6 (0.08 M), and the spectrum of AEAPTMS and FAI mixture after mixing (0.04 M, 1:1 ratio) in DMSO-d_6 for 5, 15, and 225 min, indicating that the cyclization reaction is essentially complete in ca. 5 min. (c) ^{13}C{^{1}H} NMR spectrum and (d) ^{1}H-^{13}C Heteronuclear Single Quantum Coherence (HSQC) NMR spectrum of the AEAPTMS and FAI mixture after mixing (0.04 M, 1/1 ratio) in DMSO-d_6 for 10 h. The relatively clean ^{13}C NMR spectrum suggests the cyclization reaction is complete and the product is stable in DMSO-d_6.

Figure 3b shows ^{1}H NMR spectra of AEAPTMS and the mixed solutions of AEAPTMS and FAI in DMSO-d_6 (0.04 M) with varying mixing times. Within 5 minutes, the mixed solution shows a new peak in the ^{1}H NMR spectrum at a chemical shift of 7.10 ppm, while the characteristic methylene resonances of AEAPTMS, especially those assigned to CH_2N groups, shift and the signal corresponding to the methine resonance of FA^+ (7.86 ppm)[47] is absent. As shown in Figure 3c, the ^{13}C{^{1}H} NMR spectrum of the same solution after mixing for 10 hours shows a new signal at 158.1 ppm, indicating the formation of a new sp^2 carbon environment not attributable to FA^+.

Heteronuclear single quantum correlation (HSQC) spectroscopy (Figure 3d) indicates that the proton and carbon associated with these two new resonances are bonded to one another. This data, along with Appendix B, Figures S11–S12, suggest the nucleophilic attack of AEAPTMS on FA^+, leading to ring formation with concomitant elimination of ammonia. Appendix B, Figure S13 shows the mass spectrum of AEAPTMS and mixed solution of AEAPTMS and FAI. The signal at *m/z* = 233.3 is also consistent with the formation of 1-(3-(trimethoxysilyl)propyl)-4,5-dihydro-1*H*-imidazol-3-ium cation after mixing AEAPTMS and FAI, thus strongly supporting the proposed reaction.

In contrast, the reaction between APTMS and FAI in DMSO-d_6 (0.04 M) appears to be ca. 50% complete after 5 minutes and does not proceed further, even over many hours (Appendix B, Figure S15a). The expected initial products of APTMS and FA^+ are the *N*-(3-(trimethoxysilyl)propyl)formamidinium ion and ammonia. Subsequent proton transfer from *N*-(3-(trimethoxysilyl)propyl)formamidinium to a second molecule of APTMS would result in the formation of a *N*-(3-(trimethoxysilyl)propyl)formamidine and the non-nucleophilic 3-(trimethoxysilyl)propylammonium ion. Although typical formamidinium derivatives are insufficiently acidic to protonate typical primary amines, in the present case we hypothesize that the formamidine product of this proton-transfer equilibrium is stabilized by coordination of the deprotonated nitrogen to the Lewis acidic silicon center, forming a five-membered ring (Appendix B, Figure S15b, S16). The reaction *does* proceed to completion if conducted in methanol-d_4 (Appendix B, Figure S17), which can compete for binding with the silicon center (as evidenced by scrambling of CD_3 groups into the $Si(OMe)_3$ group, Appendix B, Figure S18), or in the presence of the strong non-nucleophilic base DBU, which accepts the proton generated on forming the internal formamidine-Si adduct (Appendix B, Figures S16, S19). Similar interactions are possible

in the case of the AEAPTMS / FA reaction; however, a five-membered cyclic internal formamidine adduct analogous to that proposed above for the APTMS cannot be formed since there is no appropriate NH proton to be lost, a possible eight-membered adduct is likely less stable, and, critically, the formation of the cyclic 1-(3-(trimethoxysilyl)propyl)-4,5-dihydro-1*H*-imidazol-3-ium cation is thermodynamically favorable (Appendix B, Figure S14). We also use ^{1}H, $^{13}C\{^{1}H\}$, and 2D NMR methods, as well as mass spectrometry (MS), to confirm the structures of reaction products (Figure 3b-d, Appendix B, Figure S11-S13). Mass spectroscopy suggests reaction of AEAPTMS and FAI exclusively forms of the above-mentioned imidazolium derivative, with no detectable uncyclized products (Appendix B, Figure S13). In contrast, mass spectra for the reaction of APTMS and FAI (1:1) in methanol show peaks assignable to both *N*-(3-(trimethoxysilyl)propyl)formamidinium (*m/z* = 207.2) and *N,N'*-bis(3-(trimethoxysilyl)propyl)formamidinium (*m/z* = 369.2) (Appendix B, Figure S23).

Given the difference in reactivity of formamidinium with amino-silanes in solution, we employed time-of-flight secondary ion mass spectroscopy (ToF-SIMS) to explore the interaction of the amino-silanes and FA^{+} on solid-state perovskite interfaces.

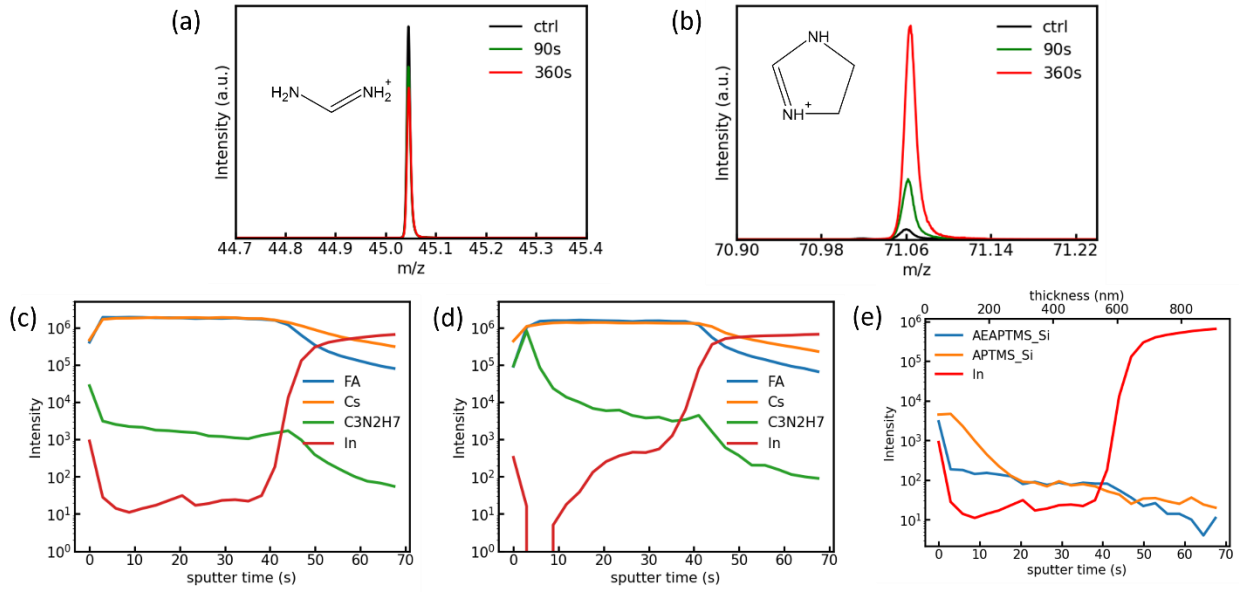

Figure 4. ToF-SIMS mass spectra at (a) m/z = 45.05 and (b) m/z = 71.06, corresponding to FA^+ and 4,5-dihydroimidazolium respectively, of perovskite films passivated with AEAPTMS using different deposition times. ToF-SIMS depth profile of (c) unpassivated and (d) AEAPTMS-passivated film (360 s) on ITO substrate. (e) Si depth profile of perovskite films on ITO substrate with different passivation at 90 s.

Figure 4a-b shows the signal of FA^+ (m/z = 45.05) and 4,5-dihydroimidazolium ($C_3H_2N_7^+$, m/z = 71.06, a fragment of 1-(3-(trimethoxysilyl)propyl)-4,5-dihydro-1*H*-imidazol-3-ium) respectively, from ToF-SIMS mass spectra of AEAPTMS-passivated perovskite films with varying deposition times. Figure 4a shows the signal of FA^+ decreases continuously with increasing duration of AEAPTMS-treatment, while Figure 4b shows a concomitant increase in the signal of $C_3H_2N_7^+$ (4,5-dihydroimidazolium), as expected if the AEAPTMS reacts with FA^+ to form 1-(3-(trimethoxysilyl)propyl)-4,5-dihydro-1*H*-imidazol-3-ium as suggested by the solution NMR (Figure 3a). The full mass spectrum also shows a weak signal (likely due to fragmentation) at *m/z* = 233.3 corresponding to the product of AEAPTMS-FA^+ reaction (1-(3-(trimethoxysilyl)propyl)-4,5-dihydro-1*H*-imidazol-3-ium), again in good agreement with the solution reaction scheme. We do detect a small signal at an *m/z* that is indicative of $C_3H_2N_7^+$ for an unpassivated film, which we speculate could arise from ion bombardment-induced fragmentation and subsequent recombination of FA^+ (Figure 4c). Nevertheless, the signal associated with $C_3H_2N_7^+$ ring increases by ~20 times after exposure to AEAPTMS (Figure 4d). Together, these results confirm that the reaction of AEAPTMS and FA^+ takes place rapidly on the perovskite surface, with increasing product formed at increasing deposition times.

Next, we examine the ToF-SIMs results on APTMS-treated perovskite samples, which show no evidence for *N*-(3-(trimethoxysilyl)propyl)formamidium (*m/z* = 207.2) or *N,N'*-bis(3-

(trimethoxysilyl)propyl)formamidinium (*m/z* = 369.2) mass fragments in films. In addition, for APTMS, we observe no significant changes in the signal of FA^+ with deposition time (Appendix B, Figure S24), which is in contrast with the decrease in FA^+ signal with increasing deposition time for AEAPTMS (Figure 4a). It is possible that the high fragmentation probabilities of the C-N bonds would lead to dissociation of many of these compounds into APTMS and FA^+ like fragments. However given that we see (weak) signals for the parent fragment of AEAPTMS reacting with FA^+, we conclude that while it is possible that 1-(3-(trimethoxysilyl)propyl)formamidium and/or N,N′-bis(3-(trimethoxysilyl)propyl)formamidinium are formed from the reaction of APTMS and FA^+ during vacuum deposition, the reaction proceeds less (or the products fragment more readily) than in the case of AEAPTMS reacting with FA^+ during vacuum deposition.

Previously, both our group,[15,19,20,28] and others,[34] have proposed the amino-silane passivators can passivate halide vacancies (undercoordinated Pb^{2+} sites), and that protonated ammoniums could stabilize A-site vacancies in the perovskite surface. Evidence also suggests that thin silane treatments also help reduce contact-induced recombination that occurs when the perovskite is in contact with an extraction layer or electrical contact.[28] However, the performance improvements of AEAPTMS, which clearly reacts with FA^+ in the perovskite, suggest additional mechanisms. Taddei et al. proposed a lower-dimensional perovskite structure containing the 4,5-dihydroimidazolium cation can form upon reaction with sufficient concentrations of ethylenediamine,[46] while Luther and coworkers have recently proposed that 1D phases are formed by the reaction products of simple alkylamines and diamines with FA^+.[48] Presumably these phases form heterojunctions at the surface, which would both push carriers away from surface defects, as well as provide for some electronic decoupling from the electrodes/transport layers.

Finally, we also compare the penetration of the AEAPTMS and APTMS into the perovskite films by tracking the depth (sputter-time) dependence of Si containing fragments. Figure 4e shows that the initial Si signal is slightly higher for the APTMS-treated films compared to the AEAPTMS-treated films, possibly due to the higher vapor pressure of APTMS leading to faster deposition. Furthermore, the APTMS-treated ToF-SIMS depth profile indicates that Si penetrates deeper into the perovskite bulk compared to the AEAPTMS-treated depth profile with the same treatment duration, these results suggest that the AEAPTMS/perovskite interface is relatively sharp compared to a more diffused APTMS/perovskite interface. We speculate that the higher reactivity of AEAPTMS with FA^+, as observed by solution NMR, and the formation of bulkier reaction products help restrict its penetration into the film, where the reacted cations likely remain near the surface with polymerized tails forming a confined passivating network. This confinement may account for the wider processing window observed for AEAPTMS.

3.4 Conclusion

In summary, we investigated the effects of APTMS and AEAPTMS surface treatments on halide perovskites. While both amino-silanes can effectively passivate the perovskite surface under optimized conditions, we find that AEAPTMS has a wider processing window, and yields the highest solar cell efficiency, with the most notable improvements observed in the V_{OC} and FF under optimized conditions. We highlight the tunable balance between beneficial passivation and detrimental effects, namely electrical insulation and loss of 3D perovskite phase, influenced by amino-silane treatment duration and conditions.

Using a combination of NMR spectroscopy and depth-resolved ToF-SIMS, we demonstrate that FA^+ cations chemically react with these amino-silanes. Overall, our results provide new insight

into the interfacial chemistry between amino-silanes and halide perovskites and contribute to the growing evidence that reactivity of FA^+ with amine-containing treatments, including amine-functionalized silanes, is a general phenomenon that underpins many additive and passivation approaches. For the future design of the surface passivator, incorporating controllable interfacial reactivity and cross-linking functionalities that yield sharp, self-limiting, and stable interfaces could further enhance device performance and long-term stability. This work also underscores the importance of optimizing treatment conditions to maximize passivation benefits while minimizing adverse effects, an essential consideration for the advancement of halide perovskite semiconductors and the development of robust passivation strategies.

3.5 Acknowledgements

This paper is based primarily on work originally supported by the Office of Naval Research Award (N00014-20-1-2587). The authors acknowledge the use of facilities and instruments at the Photonics Research Center (PRC) at the Department of Chemistry, University of Washington; Research Training Testbed (RTT), part of the Washington Clean Energy Testbeds system. Part of this work is conducted at the Molecular Analysis Facility (MAF), a National Nanotechnology Coordinated Infrastructure site at the University of Washington which is supported in part by funds from the National Science Foundation (awards NNCI-2025489, NNCI-1542101), the Molecular Engineering & Sciences Institute. NMR and mass spectrometry studies were conducted as part of the Center for Hybrid Organic Inorganic Semiconductors for Energy (CHOISE) an Energy Frontier Research Center funded by the Office of Basic Energy Sciences, Office of Science within the U.S. Department of Energy. An Advion Compact Mass Spectrometer used to support the synthetic work at the University of Colorado was purchased using a DURIP equipment grant from the Office of Naval Research (N00014-23-1-2058). We

also acknowledge Dr. Fangyuan Jiang at the University of Washington for useful scientific discussions.

3.6 References

(1) Tress, W. Metal Halide Perovskites as Mixed Electronic–Ionic Conductors: Challenges and Opportunities—From Hysteresis to Memristivity. *J. Phys. Chem. Lett.* **2017**, *8* (13), 3106–3114. https://doi.org/10.1021/acs.jpclett.7b00975.

(2) Jena, A. K.; Kulkarni, A.; Miyasaka, T. Halide Perovskite Photovoltaics: Background, Status, and Future Prospects. *Chem. Rev.* **2019**, *119* (5), 3036–3103. https://doi.org/10.1021/acs.chemrev.8b00539.

(3) Jiang, F.; Shi, Y.; Rana, T. R.; Morales, D.; Gould, I. E.; McCarthy, D. P.; Smith, J. A.; Christoforo, M. G.; Yaman, M. Y.; Mandani, F.; Terlier, T.; Contreras, H.; Barlow, S.; Mohite, A. D.; Snaith, H. J.; Marder, S. R.; MacKenzie, J. D.; McGehee, M. D.; Ginger, D. S. Improved Reverse Bias Stability in p–i–n Perovskite Solar Cells with Optimized Hole Transport Materials and Less Reactive Electrodes. *Nat Energy* **2024**, *9* (10), 1275–1284. https://doi.org/10.1038/s41560-024-01600-z.

(4) Eperon, G. E.; Hörantner, M. T.; Snaith, H. J. Metal Halide Perovskite Tandem and Multiple-Junction Photovoltaics. *Nat Rev Chem* **2017**, *1* (12), 1–18. https://doi.org/10.1038/s41570-017-0095.

(5) Wang, R.; Huang, T.; Xue, J.; Tong, J.; Zhu, K.; Yang, Y. Prospects for Metal Halide Perovskite-Based Tandem Solar Cells. *Nat. Photonics* **2021**, *15* (6), 411–425. https://doi.org/10.1038/s41566-021-00809-8.

(6) Shen, G.; Zhang, Y.; Juarez, J.; Contreras, H.; Sindt, C.; Xu, Y.; Kline, J.; Barlow, S.; Reichmanis, E.; Marder, S. R.; Ginger, D. S. Increased Brightness and Reduced Efficiency Droop in Perovskite Quantum Dot Light-Emitting Diodes Using Carbazole-Based Phosphonic Acid Interface Modifiers. *ACS Nano* **2025**, *19* (1), 1116–1127. https://doi.org/10.1021/acsnano.4c13036.

(7) Liu, X.-K.; Xu, W.; Bai, S.; Jin, Y.; Wang, J.; Friend, R. H.; Gao, F. Metal Halide Perovskites for Light-Emitting Diodes. *Nat Mater* **2021**, *20* (1), 10–21. https://doi.org/10.1038/s41563-020-0784-7.

(8) Zheng, D.; Pauporté, T. Advances in Optical Imaging and Optical Communications Based on High-Quality Halide Perovskite Photodetectors. *Advanced Functional Materials* **2023**, *34* (11), 2311205. https://doi.org/10.1002/adfm.202311205.

(9) Dong, H.; Ran, C.; Gao, W.; Li, M.; Xia, Y.; Huang, W. Metal Halide Perovskite for Next-Generation Optoelectronics: Progresses and Prospects. *eLight* **2023**, *3* (1), 3.

https://doi.org/10.1186/s43593-022-00033-z.

(10) Utzat, H.; Sun, W.; Kaplan, A. E. K.; Krieg, F.; Ginterseder, M.; Spokoyny, B.; Klein, N. D.; Shulenberger, K. E.; Perkinson, C. F.; Kovalenko, M. V.; Bawendi, M. G. Coherent Single-Photon Emission from Colloidal Lead Halide Perovskite Quantum Dots. *Science* **2019**, *363* (6431), 1068–1072. https://doi.org/10.1126/science.aau7392.

(11) Nguyen, H. A.; Dixon, G.; Dou, F. Y.; Gallagher, S.; Gibbs, S.; Ladd, D. M.; Marino, E.; Ondry, J. C.; Shanahan, J. P.; Vasileiadou, E. S.; Barlow, S.; Gamelin, D. R.; Ginger, D. S.; Jonas, D. M.; Kanatzidis, M. G.; Marder, S. R.; Morton, D.; Murray, C. B.; Owen, J. S.; Talapin, D. V.; Toney, M. F.; Cossairt, B. M. Design Rules for Obtaining Narrow Luminescence from Semiconductors Made in Solution. *Chem. Rev.* **2023**, *123* (12), 7890–7952. https://doi.org/10.1021/acs.chemrev.3c00097.

(12) deQuilettes, D. W.; Koch, S.; Burke, S.; Paranji, R. K.; Shropshire, A. J.; Ziffer, M. E.; Ginger, D. S. Photoluminescence Lifetimes Exceeding 8 Ms and Quantum Yields Exceeding 30% in Hybrid Perovskite Thin Films by Ligand Passivation. *ACS Energy Lett.* **2016**, *1* (2), 438–444. https://doi.org/10.1021/acsenergylett.6b00236.

(13) Schulz, P.; Cahen, D.; Kahn, A. Halide Perovskites: Is It All about the Interfaces? *Chem. Rev.* **2019**, *119* (5), 3349–3417. https://doi.org/10.1021/acs.chemrev.8b00558.

(14) Ono, L. K.; Liu, S. (Frank); Qi, Y. Reducing Detrimental Defects for High-Performance Metal Halide Perovskite Solar Cells. *Angewandte Chemie International Edition* **2020**, *59* (17), 6676–6698. https://doi.org/10.1002/anie.201905521.

(15) Jariwala, S.; Burke, S.; Dunfield, S.; Shallcross, R. C.; Taddei, M.; Wang, J.; Eperon, G. E.; Armstrong, N. R.; Berry, J. J.; Ginger, D. S. Reducing Surface Recombination Velocity of Methylammonium-Free Mixed-Cation Mixed-Halide Perovskites via Surface Passivation. *Chem. Mater.* **2021**, *3* (13), 5035–5044. https://doi.org/10.1021/acs.chemmater.1c00848.

(16) Xue, J.; Wang, R.; Yang, Y. The Surface of Halide Perovskites from Nano to Bulk. *Nature Reviews Materials* **2020**, *5* (11), 809–827. https://doi.org/10.1038/s41578-020-0221-1.

(17) deQuilettes, D. W.; Yoo, J. J.; Brenes, R.; Kosasih, F. U.; Laitz, M.; Dou, B. D.; Graham, D. J.; Ho, K.; Shi, Y.; Shin, S. S.; Ducati, C.; Bawendi, M. G.; Bulović, V. Reduced Recombination via Tunable Surface Fields in Perovskite Thin Films. *Nat Energy* **2024**, *9* (4), 457–466. https://doi.org/10.1038/s41560-024-01470-5.

(18) deQuilettes, D. W.; Zhang, W.; Burlakov, V. M.; Graham, D. J.; Leijtens, T.; Osherov, A.; Bulović, V.; Snaith, H. J.; Ginger, D. S.; Stranks, S. D. Photo-Induced Halide Redistribution in Organic–Inorganic Perovskite Films. *Nature Communications* **2016**, *7* (1), 11683. https://doi.org/10.1038/ncomms11683.

(19) Akrami, F.; Jiang, F.; Giridharagopal, R.; Ginger, D. S. Kinetic Suppression of Photoinduced Halide Migration in Wide Bandgap Perovskites via Surface Passivation. *J.*

Phys. Chem. Lett. **2023**, *14* (41), 9310–9315. https://doi.org/10.1021/acs.jpclett.3c02570.

(20) Pothoof, J.; Westbrook, R. J. E.; Giridharagopal, R.; Breshears, M. D.; Ginger, D. S. Surface Passivation Suppresses Local Ion Motion in Halide Perovskites. *J. Phys. Chem. Lett.* **2023**, *14* (26), 6092–6098. https://doi.org/10.1021/acs.jpclett.3c01089.

(21) Vashishtha, P.; Halpert, J. E. Field-Driven Ion Migration and Color Instability in Red-Emitting Mixed Halide Perovskite Nanocrystal Light-Emitting Diodes. *Chem. Mater.* **2017**, *29* (14), 5965–5973. https://doi.org/10.1021/acs.chemmater.7b01609.

(22) DuBose, J. T.; Kamat, P. V. Hole Trapping in Halide Perovskites Induces Phase Segregation. *Acc. Mater. Res.* **2022**, *3* (7), 761–771. https://doi.org/10.1021/accountsmr.2c00076.

(23) Huang, Z.; Jiang, F.; Song, Z.; Dolia, K.; Zhu, T.; Yan, Y.; Ginger, D. S. Local A-Site Phase Segregation Leads to Cs-Rich Regions Showing Accelerated Photodegradation in Mixed-Cation Perovskite Semiconductor Films. *ACS Energy Lett.* **2024**, *9* (6), 3066–3073. https://doi.org/10.1021/acsenergylett.4c00960.

(24) Wolff, C. M.; Caprioglio, P.; Stolterfoht, M.; Neher, D. Nonradiative Recombination in Perovskite Solar Cells: The Role of Interfaces. *Advanced Materials* **2019**, *31* (52), 1902762. https://doi.org/10.1002/adma.201902762.

(25) Luo, D.; Su, R.; Zhang, W.; Gong, Q.; Zhu, R. Minimizing Non-Radiative Recombination Losses in Perovskite Solar Cells. *Nat Rev Mater* **2020**, *5* (1), 44–60. https://doi.org/10.1038/s41578-019-0151-y.

(26) Yang, X.; Luo, D.; Xiang, Y.; Zhao, L.; Anaya, M.; Shen, Y.; Wu, J.; Yang, W.; Chiang, Y.-H.; Tu, Y.; Su, R.; Hu, Q.; Yu, H.; Shao, G.; Huang, W.; Russell, T. P.; Gong, Q.; Stranks, S. D.; Zhang, W.; Zhu, R. Buried Interfaces in Halide Perovskite Photovoltaics. *Advanced Materials* **2021**, *33* (7), 2006435. https://doi.org/10.1002/adma.202006435.

(27) Yang, S. J.; Wang, K.; Luo, Y.; Park, J. Y.; Yang, H.; Coffey, A. H.; Ma, K.; Sun, J.; Wieghold, S.; Zhu, C.; Dou, L. Two-Factor Phase Separations in Mixed-Halide Quasi-2D Perovskite LEDs: Dimensionality and Halide Segregations. *ACS Energy Lett.* **2023**, *8* (9), 3693–3701. https://doi.org/10.1021/acsenergylett.3c01009.

(28) Shi, Y.; Rojas-Gatjens, E.; Wang, J.; Pothoof, J.; Giridharagopal, R.; Ho, K.; Jiang, F.; Taddei, M.; Yang, Z.; Sanehira, E. M.; Irwin, M. D.; Silva-Acuña, C.; Ginger, D. S. (3-Aminopropyl)Trimethoxysilane Surface Passivation Improves Perovskite Solar Cell Performance by Reducing Surface Recombination Velocity. *ACS Energy Lett.* **2022**, *7* (11), 4081–4088. https://doi.org/10.1021/acsenergylett.2c01766.

(29) Liu, C.; Yang, Y.; Chen, H.; Xu, J.; Liu, A.; Bati, A. S. R.; Zhu, H.; Grater, L.; Hadke, S. S.; Huang, C.; Sangwan, V. K.; Cai, T.; Shin, D.; Chen, L. X.; Hersam, M. C.; Mirkin, C. A.; Chen, B.; Kanatzidis, M. G.; Sargent, E. H. Bimolecularly Passivated Interface Enables

Efficient and Stable Inverted Perovskite Solar Cells. *Science* **2023**, *382* (6672), 810–815. https://doi.org/10.1126/science.adk1633.

(30) Wang, M.; Shi, Z.; Fei, C.; Deng, Z. J. D.; Yang, G.; Dunfield, S. P.; Fenning, D. P.; Huang, J. Ammonium Cations with High pKa in Perovskite Solar Cells for Improved High-Temperature Photostability. *Nat Energy* **2023**, *8* (11), 1229–1239. https://doi.org/10.1038/s41560-023-01362-0.

(31) Jiang, Q.; Zhao, Y.; Zhang, X.; Yang, X.; Chen, Y.; Chu, Z.; Ye, Q.; Li, X.; Yin, Z.; You, J. Surface Passivation of Perovskite Film for Efficient Solar Cells. *Nat. Photonics* **2019**, *13* (7), 460–466. https://doi.org/10.1038/s41566-019-0398-2.

(32) Westbrook, R. J. E.; Macdonald, T. J.; Xu, W.; Lanzetta, L.; Marin-Beloqui, J. M.; Clarke, T. M.; Haque, S. A. Lewis Base Passivation Mediates Charge Transfer at Perovskite Heterojunctions. *J. Am. Chem. Soc.* **2021**, *143* (31), 12230–12243. https://doi.org/10.1021/jacs.1c05122.

(33) Jenneskens, L. W.; Schuurs, H. E. C.; Simons, D.-J.; Willems, L. Molecular Mechanisms of Adhesion Promotion by Silane Coupling Agents in Glass Bead-Reinforced Polyamide-6 Model Composites. *Composites* **1994**, *25* (7), 504–511. https://doi.org/10.1016/0010-4361(94)90177-5.

(34) Lin, Y.-H.; Vikram; Yang, F.; Cao, X.-L.; Dasgupta, A.; Oliver, R. D. J.; Ulatowski, A. M.; McCarthy, M. M.; Shen, X.; Yuan, Q.; Christoforo, M. G.; Yeung, F. S. Y.; Johnston, M. B.; Noel, N. K.; Herz, L. M.; Islam, M. S.; Snaith, H. J. Bandgap-Universal Passivation Enables Stable Perovskite Solar Cells with Low Photovoltage Loss. *Science* **2024**, *384* (6697), 767–775. https://doi.org/10.1126/science.ado2302.

(35) Zheng, R.; Zhao, S.; Zhang, H.; Li, H.; Zhuang, J.; Liu, X.; Li, H.; Wang, H. Defect Passivation Grain Boundaries Using 3-Aminopropyltrimethoxysilane for Highly Efficient and Stable Perovskite Solar Cells. *Solar Energy* **2021**, *224*, 472–479. https://doi.org/10.1016/j.solener.2021.06.001.

(36) Xu, J.; Boyd, C. C.; Yu, Z. J.; Palmstrom, A. F.; Witter, D. J.; Larson, B. W.; France, R. M.; Werner, J.; Harvey, S. P.; Wolf, E. J.; Weigand, W.; Manzoor, S.; Hest, M. F. A. M. van; Berry, J. J.; Luther, J. M.; Holman, Z. C.; McGehee, M. D. Triple-Halide Wide–Band Gap Perovskites with Suppressed Phase Segregation for Efficient Tandems. *Science* **2020**, *367* (6482), 1097–1104. https://doi.org/10.1126/science.aaz5074.

(37) Fu, F.; Li, J.; Yang, T. C.-J.; Liang, H.; Faes, A.; Jeangros, Q.; Ballif, C.; Hou, Y. Monolithic Perovskite-Silicon Tandem Solar Cells: From the Lab to Fab? *Advanced Materials* **2022**, *34* (24), 2106540. https://doi.org/10.1002/adma.202106540.

(38) Al-Ashouri, A.; Köhnen, E.; Li, B.; Magomedov, A.; Hempel, H.; Caprioglio, P.; Márquez, J. A.; Morales Vilches, A. B.; Kasparavicius, E.; Smith, J. A.; Phung, N.; Menzel, D.; Grischek, M.; Kegelmann, L.; Skroblin, D.; Gollwitzer, C.; Malinauskas, T.; Jošt, M.;

Matič, G.; Rech, B.; Schlatmann, R.; Topič, M.; Korte, L.; Abate, A.; Stannowski, B.; Neher, D.; Stolterfoht, M.; Unold, T.; Getautis, V.; Albrecht, S. Monolithic Perovskite/Silicon Tandem Solar Cell with >29% Efficiency by Enhanced Hole Extraction. *Science* **2020**, *370* (6522), 1300–1309. https://doi.org/10.1126/science.abd4016.

(39) Liu, J.; De Bastiani, M.; Aydin, E.; Harrison, G. T.; Gao, Y.; Pradhan, R. R.; Eswaran, M. K.; Mandal, M.; Yan, W.; Seitkhan, A.; Babics, M.; Subbiah, A. S.; Ugur, E.; Xu, F.; Xu, L.; Wang, M.; Rehman, A. ur; Razzaq, A.; Kang, J.; Azmi, R.; Said, A. A.; Isikgor, F. H.; Allen, T. G.; Andrienko, D.; Schwingenschlögl, U.; Laquai, F.; De Wolf, S. Efficient and Stable Perovskite-Silicon Tandem Solar Cells through Contact Displacement by MgFx. *Science* **2022**, *377* (6603), 302–306. https://doi.org/10.1126/science.abn8910.

(40) Sypabekova, M.; Hagemann, A.; Rho, D.; Kim, S. Review: 3-Aminopropyltriethoxysilane (APTES) Deposition Methods on Oxide Surfaces in Solution and Vapor Phases for Biosensing Applications. *Biosensors* **2023**, *13* (1), 36. https://doi.org/10.3390/bios13010036.

(41) Li, L.; Wang, Y.; Wang, X.; Lin, R.; Luo, X.; Liu, Z.; Zhou, K.; Xiong, S.; Bao, Q.; Chen, G.; Tian, Y.; Deng, Y.; Xiao, K.; Wu, J.; Saidaminov, M. I.; Lin, H.; Ma, C.-Q.; Zhao, Z.; Wu, Y.; Zhang, L.; Tan, H. Flexible All-Perovskite Tandem Solar Cells Approaching 25% Efficiency with Molecule-Bridged Hole-Selective Contact. *Nat Energy* **2022**, *7* (8), 708–717. https://doi.org/10.1038/s41560-022-01045-2.

(42) Fu, S.; Sun, N.; Chen, H.; Liu, C.; Wang, X.; Li, Y.; Abudulimu, A.; Xu, Y.; Ramakrishnan, S.; Li, C.; Yang, Y.; Wan, H.; Huang, Z.; Xian, Y.; Yin, Y.; Zhu, T.; Chen, H.; Rahimi, A.; Saeed, M. M.; Zhang, Y.; Yu, Q.; Ginger, D. S.; Ellingson, R. J.; Chen, B.; Song, Z.; Kanatzidis, M. G.; Sargent, E. H.; Yan, Y. On-Demand Formation of Lewis Bases for Efficient and Stable Perovskite Solar Cells. *Nat. Nanotechnol.* **2025**, 1–7. https://doi.org/10.1038/s41565-025-01900-9.

(43) Almasabi, K.; Zheng, X.; Turedi, B.; Alsalloum, A. Y.; Lintangpradipto, M. N.; Yin, J.; Gutiérrez-Arzaluz, L.; Kotsovos, K.; Jamal, A.; Gereige, I.; Mohammed, O. F.; Bakr, O. M. Hole-Transporting Self-Assembled Monolayer Enables Efficient Single-Crystal Perovskite Solar Cells with Enhanced Stability. *ACS Energy Lett.* **2023**, *8* (2), 950–956. https://doi.org/10.1021/acsenergylett.2c02333.

(44) Wojciechowski, K.; Leijtens, T.; Siprova, S.; Schlueter, C.; Hörantner, M. T.; Wang, J. T.-W.; Li, C.-Z.; Jen, A. K.-Y.; Lee, T.-L.; Snaith, H. J. C60 as an Efficient N-Type Compact Layer in Perovskite Solar Cells. *J. Phys. Chem. Lett.* **2015**, *6* (12), 2399–2405. https://doi.org/10.1021/acs.jpclett.5b00902.

(45) Jiang, Q.; Tong, J.; Xian, Y.; Kerner, R. A.; Dunfield, S. P.; Xiao, C.; Scheidt, R. A.; Kuciauskas, D.; Wang, X.; Hautzinger, M. P.; Tirawat, R.; Beard, M. C.; Fenning, D. P.; Berry, J. J.; Larson, B. W.; Yan, Y.; Zhu, K. Surface Reaction for Efficient and Stable Inverted Perovskite Solar Cells. *Nature* **2022**, *611* (7935), 278–283.

https://doi.org/10.1038/s41586-022-05268-x.

(46) Taddei, M.; Smith, J. A.; Gallant, B. M.; Zhou, S.; Westbrook, R. J. E.; Shi, Y.; Wang, J.; Drysdale, J. N.; McCarthy, D. P.; Barlow, S.; Marder, S. R.; Snaith, H. J.; Ginger, D. S. Ethylenediamine Addition Improves Performance and Suppresses Phase Instabilities in Mixed-Halide Perovskites. *ACS Energy Lett.* **2022**, *7* (12), 4265–4273. https://doi.org/10.1021/acsenergylett.2c01998.

(47) Zhou, S.; Gallant, B. M.; Zhang, J.; Shi, Y.; Smith, J.; Drysdale, J. N.; Therdkatanyuphong, P.; Taddei, M.; McCarthy, D. P.; Barlow, S.; Kilbride, R. C.; Dasgupta, A.; Marshall, A. R.; Wang, J.; Kubicki, D. J.; Ginger, D. S.; Marder, S. R.; Snaith, H. J. Reactive Passivation of Wide-Bandgap Organic–Inorganic Perovskites with Benzylamine. *J. Am. Chem. Soc.* **2024**, *146* (40), 27405–27416. https://doi.org/10.1021/jacs.4c06659.

(48) Minh, D. N.; Haque, M. A.; Yang, F.; Harvey, S. P.; Kerner, R. A.; Jiang, C.-S.; Dutta, N. S.; Hayden, S.; Taddei, M.; Zhang, X.; Davis, M. A.; Schutt, K.; Luther, J. M. The Reactive Nature of Formamidinium: Amine Passivation Induces Heterostructure Formation in Inverted Perovskite Cells. *Joule* **2025**, *9* (7), 102055. https://doi.org/10.1016/j.joule.2025.102055.

Appendix A: Supporting Information for Chapter 2

A1. Experimental Procedures

1.1 Materials

All materials are used as received unless otherwise stated. Materials used in this study include formamidinium iodide (FAI, ≥99%, Sigma Aldrich), cesium iodide (CsI, 99.999% trace metals basis, Sigma Aldrich), lead(II) iodide (PbI_2, >98.0%, TCI America), lead(II) bromide ($PbBr_2$, 99.999% metals basis, Alfa Aesar), lead(II) chloride ($PbCl_2$, 99.999% trace metals basis, Sigma Aldrich), tin(IV) oxide (SnO_2, 15% in H_2O colloidal dispersion, Alfa Aesar), N,N-dimethylformamide (DMF, anhydrous 99.8%, Sigma Aldrich), dimethyl sulfoxide (DMSO, anhydrous ≥99.9%, Sigma Aldrich), methyl acetate (anhydrous 99.5%, Sigma Aldrich), and (3-aminopropyl)trimethoxysilane (APTMS, 97%, Sigma Aldrich).

1.2 Sample Preparations

The samples are synthesized on glass and indium tin oxide (ITO) coated glass substrates, 1.5 cm^2 in size, which are pre-cleaned by sequential sonication in water containing 2% Micro-90 detergent, deionized water, acetone, and isopropanol for 15 minutes each. The substrates are then ozone-cleaned for ~25 minutes.

The electron transport layer (ETL) is deposited according to a method reported by Sidhik *et. al*.[1] We dilute the commercial SnO_2 solution by deionized water to 2.67%, and spin coat 100 µL of the diluted solution at 5000 rpm for 30 s in ambient air. The SnO_2 films are annealed at 150 ºC for 30 min in ambient air. Before transferring it to the glovebox, the ETL substrates are placed in the ozone cleaner for 15 min to improve the wetting properties.

The perovskite layer with mixed halide composition of $FA_{0.8}Cs_{0.2}Pb(I_{0.8}Br_{0.2})_3$ is prepared according to a recipe reported by Jariwala *et.* al.[2] The correct molar ratio of FAI, CsI, PbI_2, $PbBr_2$, and $PbCl_2$ were dissolved in DMF and DMSO (3:1 v/v) to produce a 1 M solution. The small amount of Cl added is in stoichiometric excess (6 mg for a 1 mL solution). The pure iodide composition, $FA_{0.8}Cs_{0.2}PbI_3$, is prepared by excluding $PbBr_2$ and tuning the amount of PbI_2. The perovskite solutions are filtered through a 0.2 μm PTFE membrane filter. 100 μL of the perovskite solution is deposited on top of the substrate and spin coated at 5000 rpm for 60 s. After ~30 s, 80 μL of anhydrous methyl acetate antisolvent is dropped onto the spinning substrate. The films are then annealed at 100 ºC for 30 min. These steps are done in a nitrogen filled glovebox.

1.3 Surface Passivation with APTMS

APTMS surface passivation of the perovskite samples are done at room temperature in a vacuum oven with gauge pressure of about -27 In. of Hg relative to atmospheric pressure for 5 min, following established protocols.[3,4] To do this procedure, 1 mL of APTMS is placed in a 4 mL vial with the perovskite samples placed face up around the vial. The vial and the samples are covered with a 500 mL glass jar inside the chamber. For labile Lewis bases, we often observe reversible PL enhancements that can be removed by washing the sample or exposing it to vacuum. Polymerization of the silane by catalytic amounts of H_2O presumably helps keep the APTMS layer intact during solution or vacuum treatments.

1.4 UV-Vis Absorption Spectroscopy

UV-Vis absorption spectra are measured on a Perkin-Elmer Lambda 950 UV/Vis/NIR spectrometer in a range of 320-850 nm with an integration time of 1 s. The perovskite samples are measured on glass substrates, unless otherwise stated, in ambient conditions immediately after being removed from a nitrogen filled glovebox.

1.5 X-Ray Diffraction

The X-ray diffraction measurements are done on samples deposited on glass substrates using a Bruker D8 Discover with a Pilatus 100 K large area 2D detector (Cu Kα radiation). The perovskite samples are measured in ambient conditions immediately after being removed from a nitrogen filled glovebox.

1.6 Time-Resolved Photoluminescence (tr-PL)

tr-PL is measured using a PicoQuant Picoharp 300 TCSPC system equipped with a 640 nm pulsed diode laser. The laser was pulsed at repetition rates of 500 kHz to 250 kHz for the unpassivated and APTMS surface passivated samples respectively, to capture the full decay trace and prevent photon pile-up at the detector. The excitation fluence used for both samples is ~3.4 nJ/cm^2. The PL emission was filtered using a 700 nm long-pass filter before being directed to the detector. The data was fitted using a stretched exponential function to obtain the average PL lifetimes $<\tau>$ in Figure S4. More details about the fitting function can be found in Ref. 3.[3] The perovskite samples are measured on glass substrates in ambient conditions immediately after being removed from a nitrogen filled glovebox.

1.7 Scanning Kelvin Probe Microscopy (SKPM)

In SKPM, an AC voltage is applied to enable generation of oscillating electrical forces between the tip and the sample surface. A DC voltage is then applied to nullify the oscillating electrical forces that are due to the contact potential difference (CPD) between the tip and the sample surface. The CPD is defined as $(\varphi_{tip} - \varphi_{sample}) / e$, where φ_{tip} is the work function of the tip, φ_{sample} is the work function of the sample, and e is the elementary charge.

SKPM measurements are performed at room temperature, in the dark, and in a sealed cell under flowing nitrogen. The experiments are done using Asylum Research MFP-3D (Oxford Instruments) atomic force microscope mounted on an inverted Nikon Eclipse microscope. Cr/Pt-coated tips (BudgetSensors, 75 kHz, 3 N/m) are used to probe the CPD. The SKPM measurements are performed using the amplitude-modulated (AM) mode with a 10 nm lift height, and an AC bias applied typically of 2 V, at the tip's resonant frequency. To acquire more data points, we perform line scans and show the average data in this study.

To fit the surface potential (SP) relaxation, we use a stretched exponential decay function shown in Eq. S1. The stretched exponential decay, in this case, is a superposition of different SP relaxation times. A β value closer to 0 represents a more heterogeneous distribution in the SP relaxation times and a β value closer to 1 represents a more homogeneous distribution in the SP relaxation times. If β is 1, then the SP decay follows a single exponential decay. The characteristic time constant, τ_c, is the time required for the SP intensity to reach 1/e of the maximum intensity. The average time constant, $<\tau>$, is then given by Eq. S2, where $\Gamma(1/\beta)$ is the gamma function.

$$I = I_0 e^{(-t/\tau_c)^{\beta}} \quad \text{(S1)}$$

$$\langle \tau \rangle = \frac{\tau_c}{\beta} \Gamma\left(\frac{1}{\beta}\right) \quad \text{(S2)}$$

A summary of fitting SP relaxation parameters is given in Table S1 which shows longer time constants after APTMS surface passivation and increase in the β factors at both illumination intensities, suggestive of a reduction in the distribution of SP relaxation times.

Table S1. Stretched exponential fitting parameters used for SP relaxation after 1 h illumination of unpassivated and APTMS passivated samples at 18 kW m^{-2} and 80 kW m^{-2}.

Sample	**β (a.u.)**	**τ_c (min)**	**<τ> (min)**	**R^2**
Unpassivated (18 kW/m^2)	0.5	9.3	16.7	0.990
Unpassivated (80 kW/m^2)	0.6	19.2	29.7	0.980
APTMS (18 kW/m^2)	0.8	38.9	42.5	0.994
APTMS (80 kW/m^2)	0.8	49.7	54.7	0.994

1.8 Steady-State Photoluminescence (ss-PL)

ss-PL measurements are conducted using a Photon Etc. IMA upright microscope fitted with a transmitted darkfield condenser and ThorLabs 1501M-USB 1.4 Megapixel cooled charged-coupled device (CCD) camera. To minimize PL redshift during PL spectrum collection, both unpassivated and APTMS passivated samples are excited at a constant excitation intensity of 7 kW m^{-2}, with a spectral step size of 2 nm and integration time of 0.5 s per wavelength. Prior to the measurements, the samples are encapsulated in a nitrogen filled glovebox to prevent interactions between the samples with ambient air. To encapsulate, we edge-seal a glass slide to cover the top layer that otherwise would be exposed to ambient air. LED light curable BLUFIXX gel is used along the edges of the glass to encapsulate the samples for these measurements.

To fit the PL λ_{max} shift as a function of light soaking time, we negate the data (multiply by -1) and use a stretched exponential function, as discussed previously (Eq. S1). A summary of fitting parameters is given in Table S2 below which shows that higher illumination intensity causes faster PL redshifts in both samples, and more than 5-fold slower PL redshift in APTMS-passivated samples.

Table S2. Stretched exponential fitting parameters used for PL λ_{max} shift of unpassivated and APTMS passivated samples at 23 kW m^{-2} and 46 kW m^{-2}.

Sample	**β (a.u.)**	**τ_c (min)**	**<τ> (min)**	**R^2**
Unpassivated (23 kW/m^2)	0.8	21.7	24.4	0.997
Unpassivated (46 kW/m^2)	0.8	10.8	11.8	0.997
APTMS (23 kW/m^2)	0.7	118.1	159.8	0.997
APTMS (46 kW/m^2)	0.7	49.4	63.1	0.987

A2. Supplementary Figures

2.1. UV-Vis absorbance spectra and X-ray diffraction patterns

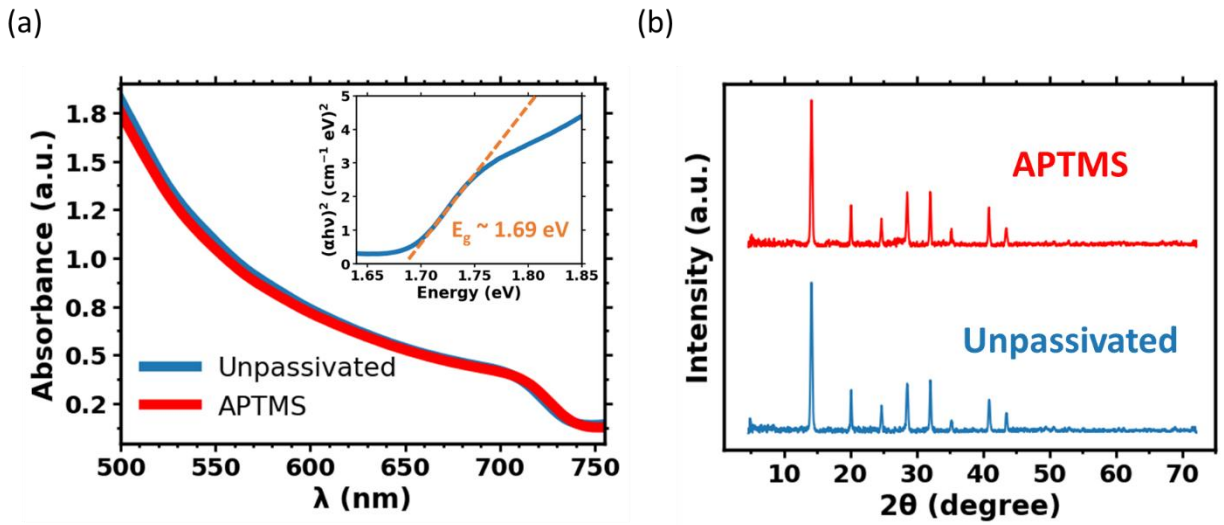

Figure S1. (a) UV-Vis absorption spectra of unpassivated (blue) and APTMS passivated (red) $FA_{0.8}Cs_{0.2}Pb(I_{0.8}Br_{0.2})_3$ samples. The inset shows the Tauc plot from the absorption spectrum of unpassivated sample that is used to determine the bandgap (E_g ~ 1.69 eV). (b) X-ray diffraction patterns of unpassivated (blue) and APTMS passivated (red) $FA_{0.8}Cs_{0.2}Pb(I_{0.8}Br_{0.2})_3$ samples.

2.2. Atomic Force Microscopy topography images

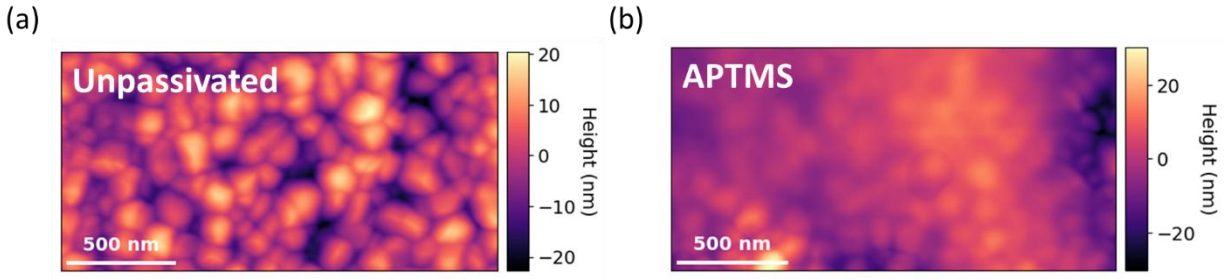

Figure S2. Atomic force microscopy (AFM) topography images of (a) the unpassivated and (b) APTMS surface passivated $FA_{0.8}Cs_{0.2}Pb(I_{0.8}Br_{0.2})_3$ samples. These images show that APTMS forms a thin layer at the perovskite surface.

2.3. Steady-state photoluminescence spectra

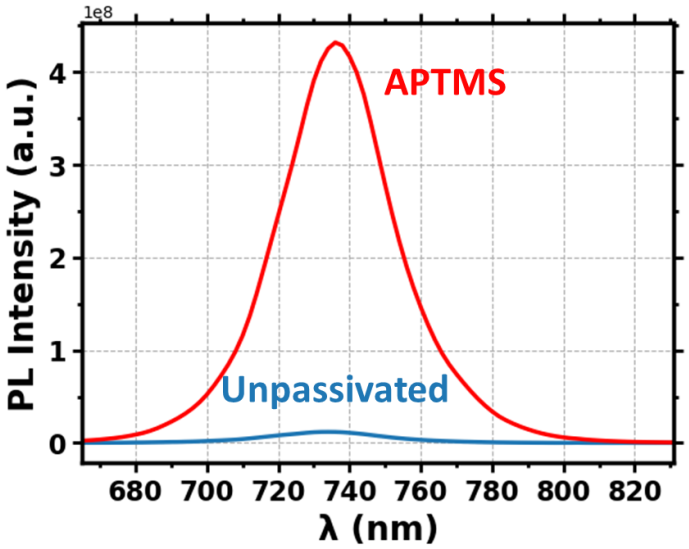

Figure S3. Steady-state PL spectra of unpassivated (blue) and APTMS surface passivated (red) $FA_{0.8}Cs_{0.2}Pb(I_{0.8}Br_{0.2})_3$ samples. The samples are excited by a 532 nm continuous wave laser with an intensity of 7 kW m^{-2}.

2.4. Time-resolved photoluminescence decays

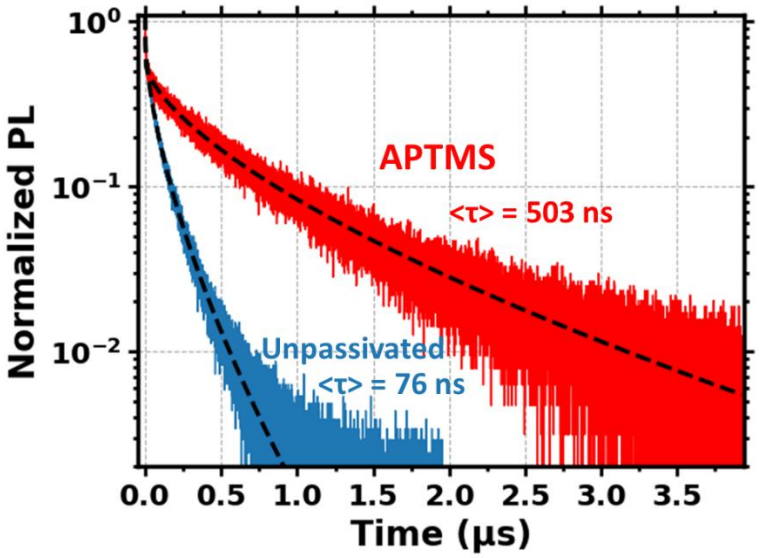

Figure S4. Time-resolved PL measurements of unpassivated (blue) and APTMS (red) surface passivated $FA_{0.8}Cs_{0.2}Pb(I_{0.8}Br_{0.2})_3$ samples. Stretched exponential fits of the decay curves are shown as dashed lines in black.

2.5. Maximum contact potential differences

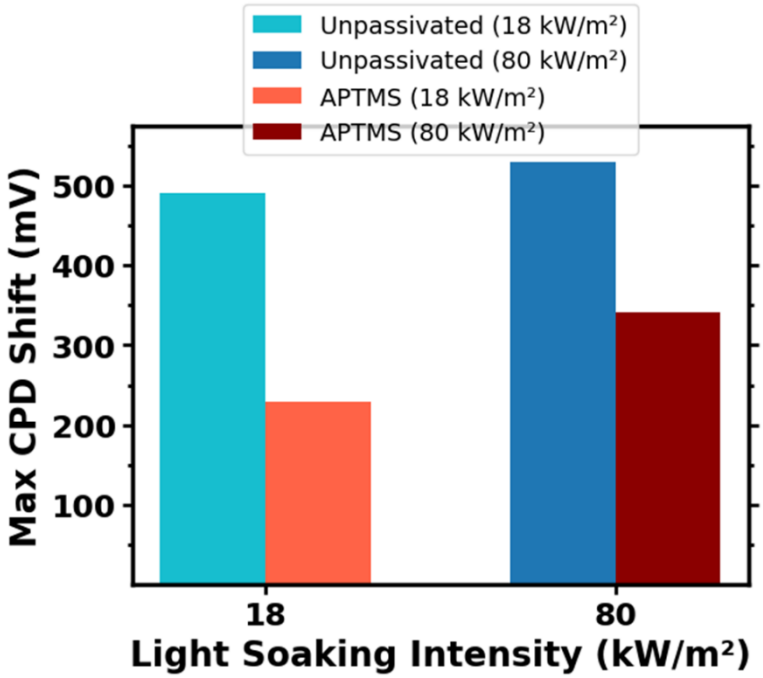

Figure S5. Maximum CPD shifts observed during 1 h illumination of unpassivated samples with intensity of 18 kW m^{-2} (light blue), 80 kW m^{-2} (dark blue), and APTMS passivated samples at 18 kW m^{-2} (light red) and 80 kW m^{-2} (dark red).

2.6. Surface potential relaxations

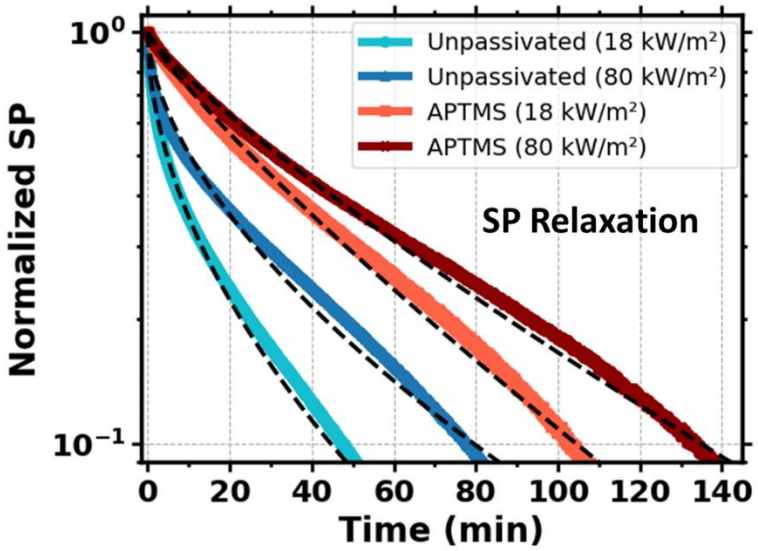

Figure S6. SP relaxation after 1 h illumination of unpassivated with intensity of 18 kW m^{-2} (light blue), 80 kW m^{-2} (dark blue), and APTMS passivated perovskites at 18 kW m^{-2} (light red) and 80 kW m^{-2} (dark red). Stretched exponential fits of the decay curves are shown as dashed lines in black. See Table S1 for detailed fitting parameters.

2.7. UV-Vis absorbance and X-ray diffraction patterns of the pure-iodide composition

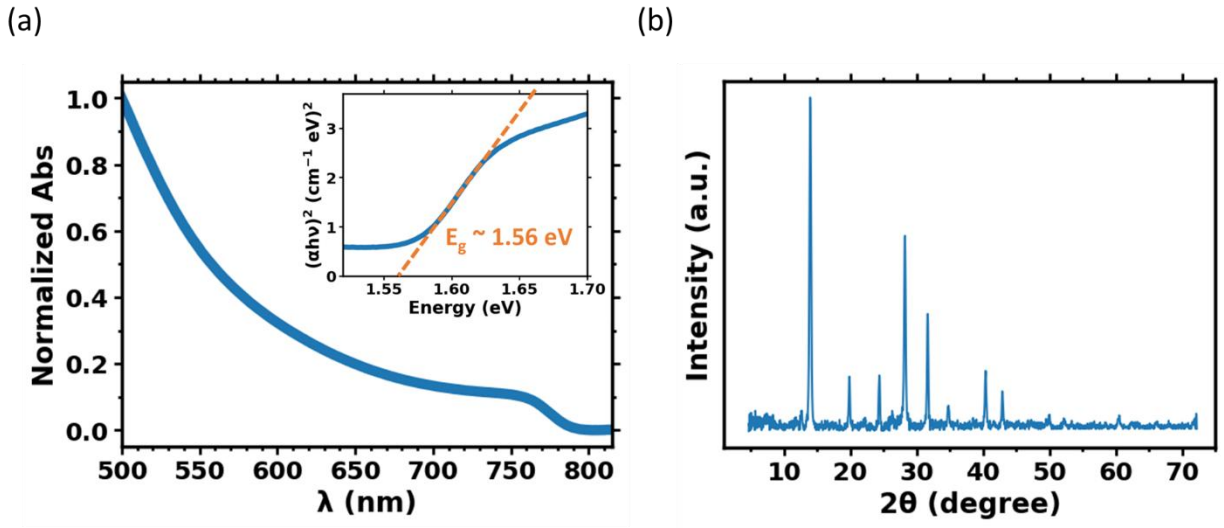

Figure S7. (a) UV-Vis absorption spectrum of pure iodide, $FA_{0.8}Cs_{0.2}PbI_3$, sample. The inset shows the Tauc plot from the absorption spectrum that is used to determine the bandgap (E_g ~ 1.56 eV). (b) X-ray diffraction patterns of pure iodide, $FA_{0.8}Cs_{0.2}PbI_3$, sample.

2.8. Photoluminescence peak position evolutions

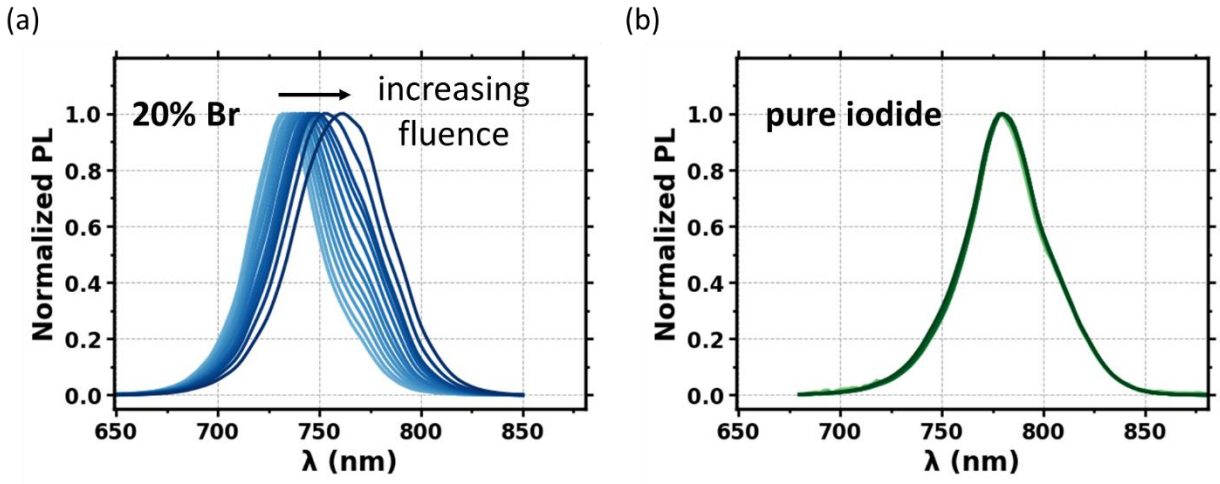

Figure S8. Steady-state PL of (a) mixed halide, $FA_{0.8}Cs_{0.2}Pb(I_{0.8}Br_{0.2})_3$, and (b) pure iodide, $FA_{0.8}Cs_{0.2}PbI_3$, samples as a function of light fluence. The light fluence is increased from 0 to 4 kJ cm^{-2}. The light source used is a 532 nm continuous wave laser**.**

2.9. UV-Vis absorbance before and after light soaking

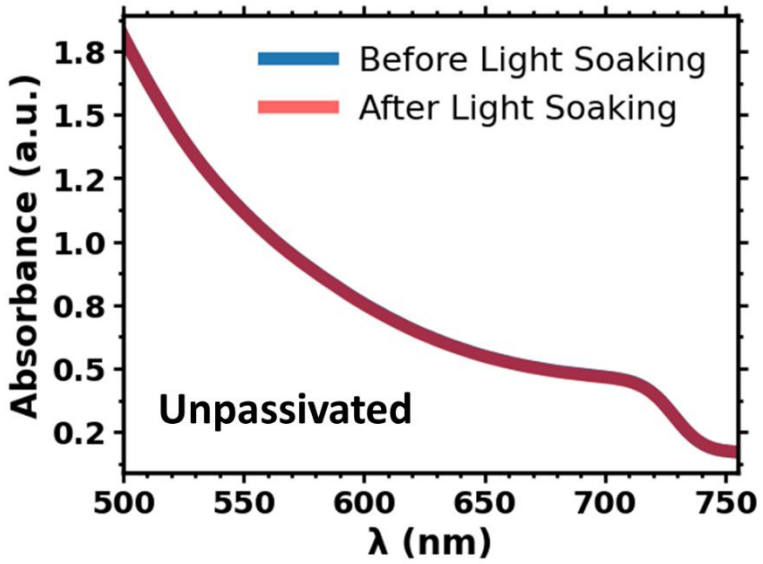

Figure S9. UV-Vis absorption spectra of unpassivated $FA_{0.8}Cs_{0.2}Pb(I_{0.8}Br_{0.2})_3$ sample before (blue) and after light soaking. The light source used to light soak the sample is a 532 nm continuous wave laser with a fluence of ~17 kJ cm^{-2}. This measurement is performed on SnO_2 covered ITO substrate and the sample is encapsulated the same way as in ss-PL measurements.

A3. References

(1) Sidhik, S.; Wang, Y.; De Siena, M.; Asadpour, R.; Torma, A. J.; Terlier, T.; Ho, K.; Li, W.; Puthirath, A. B.; Shuai, X.; Agrawal, A.; Traore, B.; Jones, M.; Giridharagopal, R.; Ajayan, P. M.; Strzalka, J.; Ginger, D. S.; Katan, C.; Alam, M. A.; Even, J.; Kanatzidis, M. G.; Mohite, A. D. Deterministic Fabrication of 3D/2D Perovskite Bilayer Stacks for Durable and Efficient Solar Cells. *Science* **2022**, *377* (6613), 1425–1430. https://doi.org/10.1126/science.abq7652.

(2) Jariwala, S.; Kumar, R. E.; Eperon, G. E.; Shi, Y.; Fenning, D. P.; Ginger, D. S. Dimethylammonium Addition to Halide Perovskite Precursor Increases Vertical and Lateral Heterogeneity. *ACS Energy Lett.* **2022**, *7* (1), 204–210. https://doi.org/10.1021/acsenergylett.1c02302.

(3) Jariwala, S.; Burke, S.; Dunfield, S.; Shallcross, R. C.; Taddei, M.; Wang, J.; Eperon, G. E.; Armstrong, N. R.; Berry, J. J.; Ginger, D. S. Reducing Surface Recombination Velocity of Methylammonium-Free Mixed-Cation Mixed-Halide Perovskites via Surface Passivation. *Chem. Mater.* **2021**, *3* (13), 5035–5044. https://doi.org/10.1021/acs.chemmater.1c00848.

(4) Shi, Y.; Rojas-Gatjens, E.; Wang, J.; Pothoof, J.; Giridharagopal, R.; Ho, K.; Jiang, F.; Taddei, M.; Yang, Z.; Sanehira, E. M.; Irwin, M. D.; Silva-Acuña, C.; Ginger, D. S. (3-Aminopropyl)Trimethoxysilane Surface Passivation Improves Perovskite Solar Cell Performance by Reducing Surface Recombination Velocity. *ACS Energy Lett.* **2022**, *7* (11), 4081–4088. https://doi.org/10.1021/acsenergylett.2c01766.

Appendix B: Supporting Information for Chapter 3

B1. Experimental Procedures

1.1 Materials

All materials are used as received unless otherwise stated. Materials used in this study include formamidinium iodide (FAI, >99.99%, Greatcell), cesium iodide (CsI, 99.999%, metal basis, Alfa Aesar), lead(II) bromide ($PbBr_2$, 99.998% metal basis, Alfa Aesar), lead(II) iodide (PbI_2, 99.999%, Sigma Aldrich), lead(II) chloride ($PbCl_2$, >99.0%, TCI), methylammonium chloride (MACl, >99.5%, Xi'an Polymer Light Technology Corp.), [2-(3,6-dimethoxy-9*H*-carbazol-9-yl)ethyl]phosphonic acid (MeO-2PACz, TCI), (3-aminopropyl)trimethoxysilane (APTMS, 97%, Sigma Aldrich), *N*-[3-(trimethoxysilyl)propyl]ethylenediamine (AEAPTMS, 97%, Sigma Aldrich), anisole (anhydrous, Sigma Aldrich), *N,N*-dimethylformamide (DMF, anhydrous, Sigma Aldrich), dimethyl sulfoxide (DMSO, anhydrous, Sigma Aldrich), isopropanol (IPA, Sigma Aldrich), C60 (98%, Sigma Aldrich), bathocuproine (BCP, 96%, Sigma Aldrich).

1.2 Sample Preparations

The samples are synthesized on glass and patterned indium tin oxide (ITO, Xin Yan Technology Ltd. 15 ohm per square pattern ITO glass, surface polish, XY15S) coated glass substrates, 1.5 cm^2 in size, which are pre-cleaned by sequential sonication in water containing 2% Micro-90 detergent, deionized water, acetone, and isopropanol for 15 min each. The substrates are then ozone-cleaned for ~23 min.

The hole transport layer MeO-2PACz (0.75 mg/mL in isopropanol) is spin coated on the ITO substrate at 2000 rpm for 30 s. Then the substrate is annealed at 100 °C for 10 min. After annealing,

80 µL of perovskite precursor solution (1.4 M $Cs_{0.22}FA_{0.78}Pb(I_{0.85}Br_{0.15})_3$ with 3 mol% of $MAPbCl_3$ additive in mixed solvent of DMF/DMSO = 3:1 v/v%), pre-filtered through a 0.2 µm PTFE membrane filter, is spin coated onto the substrate in two steps. First, it is spin coated at 1000 rpm for 2 s (acceleration: 1000 rpm s^{-1}), followed by a second step at 5000 rpm for 35 s (acceleration 10000 rpm s^{-1}). 250 µL of antisolvent anhydrous anisole is dropped onto the spinning substrate at 10 s before the end of the second step. The samples are then annealed at 100 °C for 20 min.

Aminosilane surface treatment of the perovskite samples is done at room temperature in a vacuum oven (Precision Vacuum Oven Model 19) with gauge pressure of about -25 in. Hg relative to atmospheric pressure, following established protocols.[1–3] To do this procedure, 1 mL of aminosilane is placed in a 4 mL vial with the perovskite samples placed face up around the vial. The vial and the samples are covered with a 500 mL glass jar inside the chamber. After the amino-silane treatment, all films were immediately transferred to a nitrogen glovebox. All optical and structural characterizations, as well as devices fabrication, were performed the next day. A schematic illustration of the vapor deposition setup is provided in Figure S26.

After aminosilane treatment, 30 nm of C_{60} and 5 nm of BCP are thermally evaporated onto the perovskite layer. For C_{60}, the deposition rate starts at 0.2 Å/s for the first 5 nm and increases to 0.5 Å/s for the remaining 25 nm. The deposition rate for BCP is 0.2 Å/s. For completing the whole perovskite solar cell device, 100 nm Ag is thermally evaporated with an evaporation rate of 0.5 Å/s for the first 10 nm, which then increases to 1 Å/s for the rest of the 90 nm.

1.3 Solar Cell Characterization

Current density-voltage (J-V) characteristics under 1 Sun equivalent illumination are measured using an ORIEL LSH-7320 ABA LED solar simulator in a nitrogen-filled glovebox, which is

calibrated with a filtered KG3 Silicon reference solar cell certified by National Renewable Energy Laboratory. The effective area of the solar cell is 0.0453 cm^2. J-V scans are carried out with a Keithley 2400 source meter unit, controlled by a program written in LabView. The voltage values are scanned with a 0.02 V step size in the range of -0.1 V to 1.2 V. The steady-state power output was carried out by measuring the solar cells under the bias of the maximum power point (MMP) and 1 Sun intensity.

1.4 UV-Vis Absorption Spectroscopy

UV-Vis absorption spectra are measured on a Perkin-Elmer Lambda 950 UV/Vis/NIR spectrometer with integration time of 1 s. The perovskite samples are measured on glass substrates.

1.5 X-Ray Diffraction

The X-ray diffraction measurements are done on samples deposited on glass substrates using a Bruker D8 Discover with a Pilatus 100 K large area 2D detector (Cu Kα radiation).

1.6 Time-Resolved Photoluminescence (TRPL)

TRPL is measured using a PicoQuant Picoharp 300 TCSPC system equipped with a 640 nm pulsed diode laser. The excitation fluence used is ~3 nJ/cm^2. The PL emission is filtered using a 700 nm long-pass filter before being directed to the detector. The data was fitted using a stretched exponential function.[1,4] The perovskite samples are measured on glass substrates.

1.7 Time-of-flight secondary ion mass spectrometry (ToF-SIMS)

Positive-ion ToF-SIMS and depth profiles are acquired using an IONTOF ToF-SIMS 5 spectrometer. Profiles are acquired in the non-interlaced mode. Spectra/images are acquired using

a 25 keV Bi_3^+ cluster ion source in the pulsed mode using HMR mode. Data is acquired using a 100 μm × 100 μm spot at 256 × 256 pixels. The ion source is operated with a current of 0.04 pA to avoid saturation in the spectra. The primary ion dose per layer is 1.5×10^{11} ions/cm^2. Sputtering is done using a gas cluster ion source using 20 keV argon 1000 clusters with a current of 6.84 nA, over an area of 500 μm × 500 μm. The sputter dose per layer is 5×10^{13} ions/cm^2. An electron flood gun and argon flooding are used for charge neutralization. Positive-ion data are calibrated using the $C_4H_7^+$, PbI^+ and Cs_2I^+ peaks with calibration errors less than 25 ppm. Mass resolving power (m/Δm) for positive-ion data is ~4000 for *m/z* = 27 ($C_2H_3^+$).

1.8 Nuclear Magnetic Resonance (NMR):

NMR experiments (including ^1H, $\{^1H\}^{13}C$, COSY, HSQC and HMBC) are conducted using a two-channel Bruker Avance III HD Nanobay 400 MHz instrument running TOPSPIN 3 equipped with a 5 mm z-gradient broadband/fluorine observation probe or a Bruker Ascend 400 spectrometer. Deuterated DMSO and methanol are used as the solvent for these experiments.

1.9 Mass Spectroscopy:

Mass spectrometry measurements are performed using an Advion Interchim Expression CMS with direct injection.

1.10 Atomic Force Microscopy

AFM topography and phase images are acquired using Asylum Research MFP-3D (Oxford Instruments) atomic force microscope mounted on an inverted Nikon Eclipse microscope. These measurements use Pt-coated tips (mikroMach, 325 kHz, 40 N/m) driven near resonance.

B2. Supplementary Figures

2.1. The Tauc plot based on UV-Vis absorbance

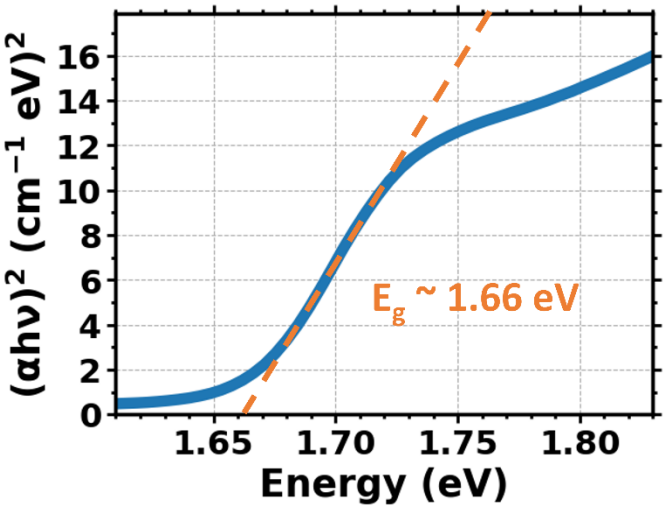

Figure S1. The Tauc plot of $FA_{0.78}Cs_{0.22}Pb(I_{0.85}Br_{0.15})_3$ based on the UV-Vis absorbance to determine the bandgap (E_g ~ 1.66 eV).

2.2. X-ray diffraction patterns

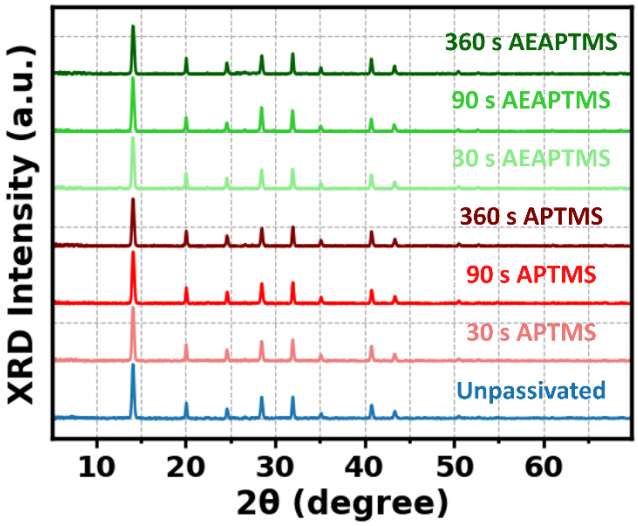

Figure S2. X-ray diffraction patterns of unpassivated (blue), APTMS-treated samples with varying deposition times (red), and AEAPTMS-treated samples with varying deposition times (green).

2.3. AFM topography and phase images (APTMS)

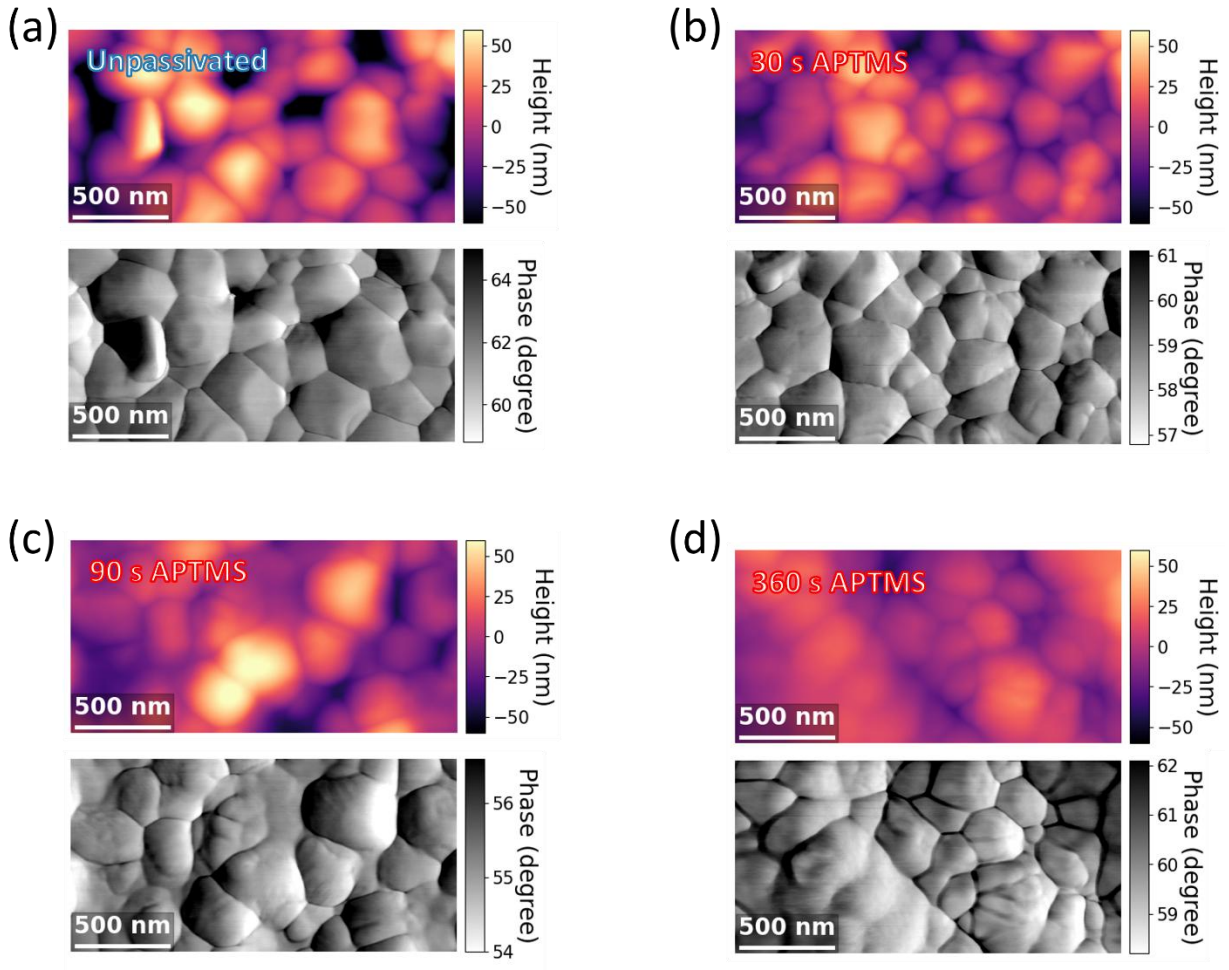

Figure S3. AFM topography and phase images of (a) unpassivated, (b) 30s, (c) 90 s, and (d) 360 s APTMS treatment time.

2.4. AFM topography and phase images (AEAPTMS)

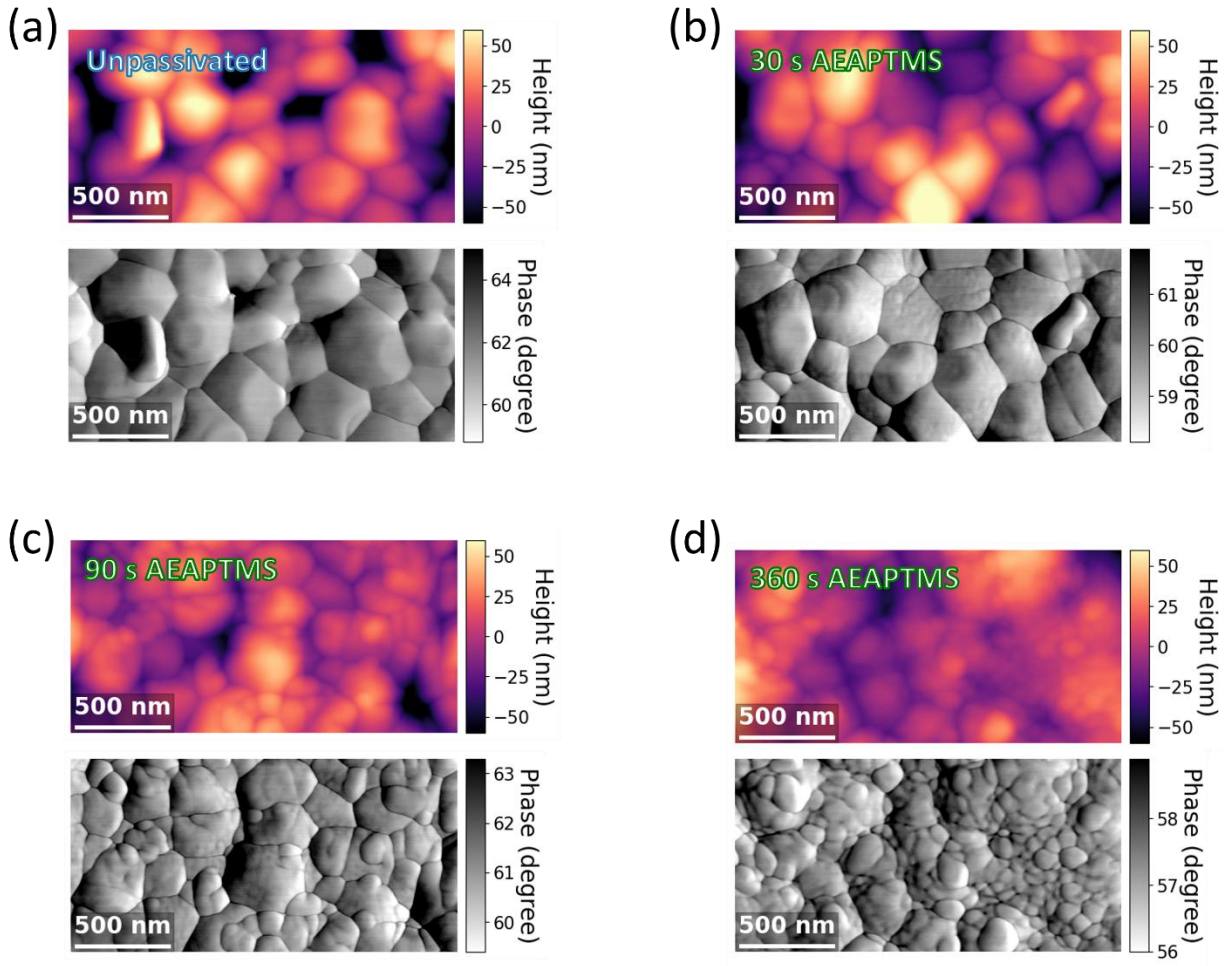

Figure S4. AFM topography and phase images of (a) unpassivated, (b) 30s, (c) 90 s, and (d) 360 s AEAPTMS treatment time.

2.5. AFM topography and phase images (larger-scale)

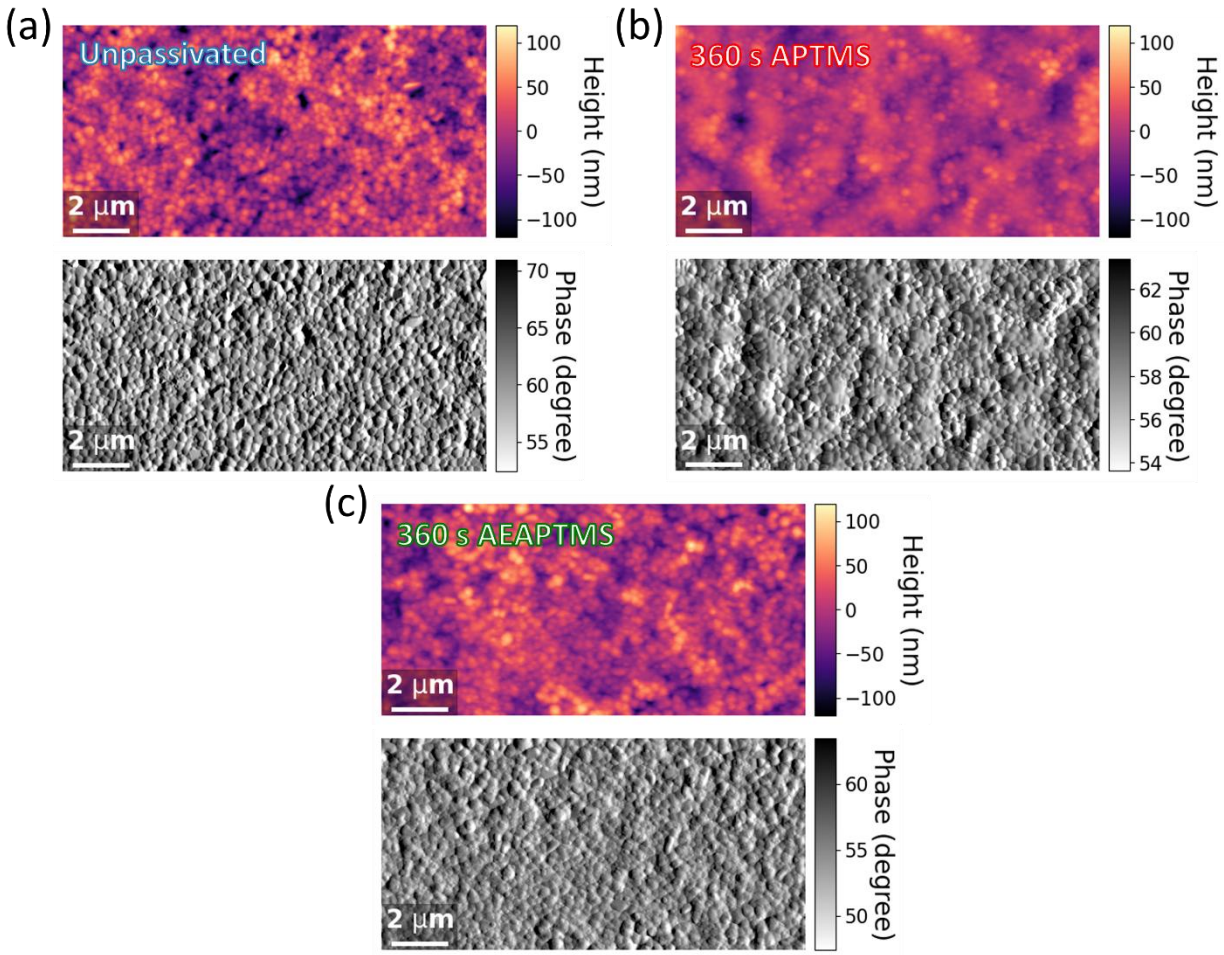

Figure S5. Larger-scale AFM topography and phase images of (a) unpassivated, (b) 360 s APTMS-, and (c) 360 s AEAPTMS-treated samples.

2.6. Solar cell performance (APTMS)

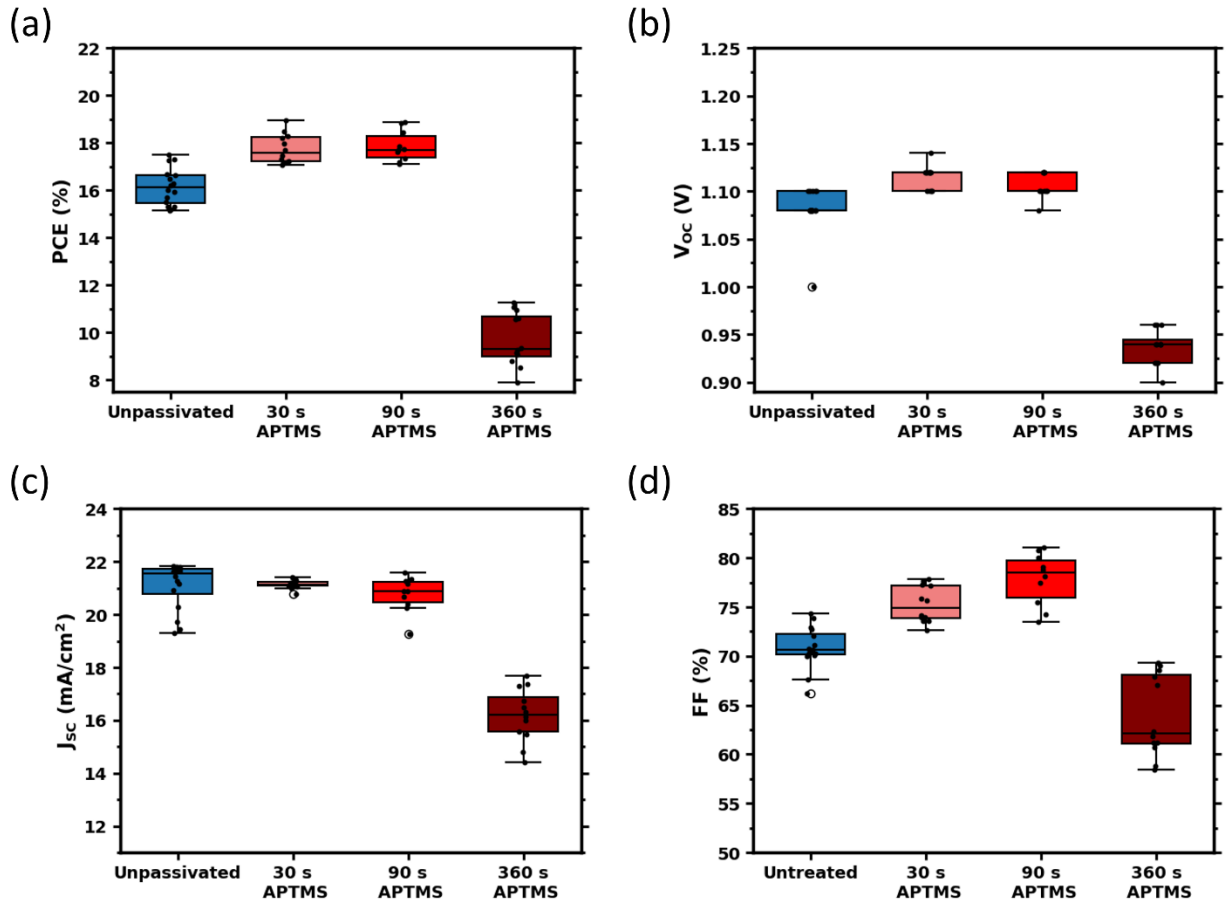

Figure S6. (a) PCE, (b) V_{OC} (c) J_{SC}, and (d) FF of unpassivated (blue) and APTMS-treated (red) solar cells with 30 s, 90 s, and 360 s APTMS deposition times, based on forward J-V scans.

2.7. X-ray diffraction (900 s deposition time)

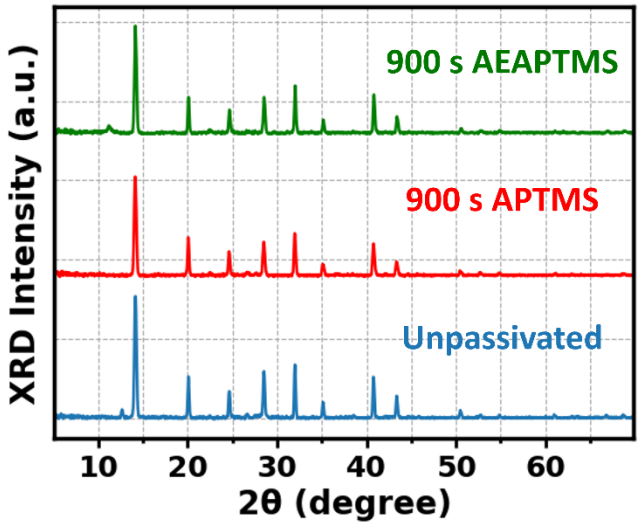

Figure S7. X-ray diffraction patterns of unpassivated (blue), APTMS-treated (red), and AEAPTMS-treated (green) samples at 900 s deposition time.

2.8. UV-Vis absorption spectra

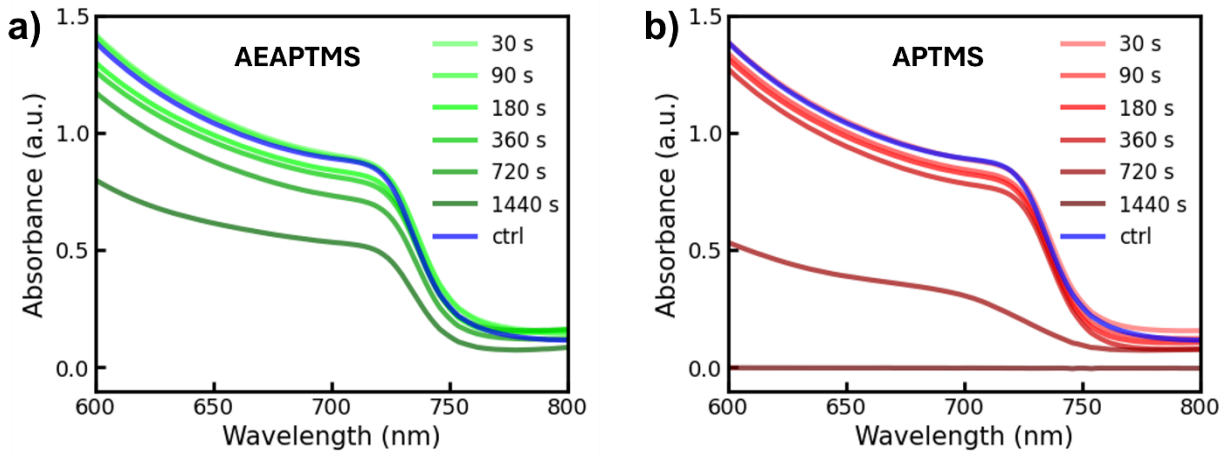

Figure S8. UV–Vis absorption spectra of perovskite films treated with (a) AEAPTMS and (b) APTMS under different exposure durations. The absorbance gradually decreases with increasing exposure time. After 1440s of APTMS treatment, perovskite film becomes completely transparent.

2.9. J-V curves of champion solar cells (AEAPTMS)

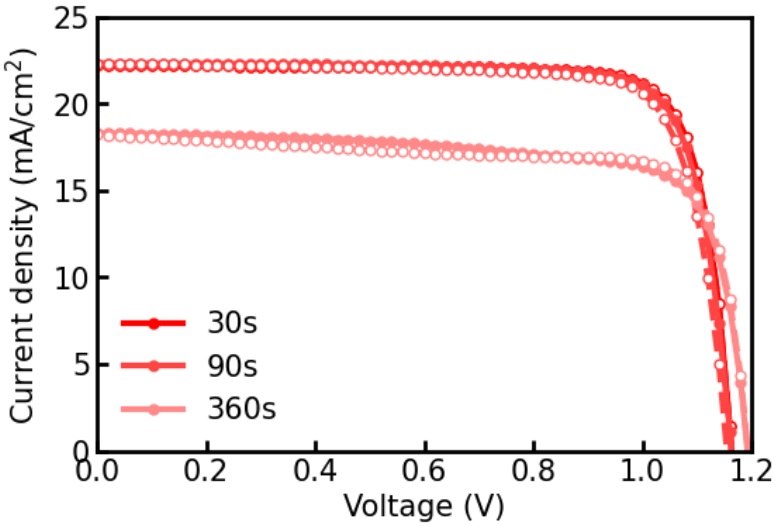

Figure S9. J-V curve of champion perovskite solar cells with AEAPTMS passivation for different deposition times.

2.10. J-V curves of champion solar cells (APTMS)

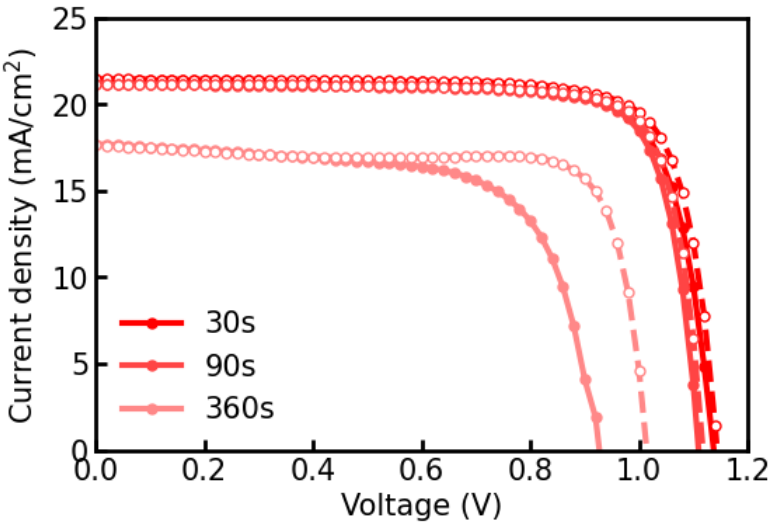

Figure S10. J-V curve of champion perovskite solar cells with APTMS passivation for different deposition times.

2.11. ^{1}H-^{1}H correlation spectrum

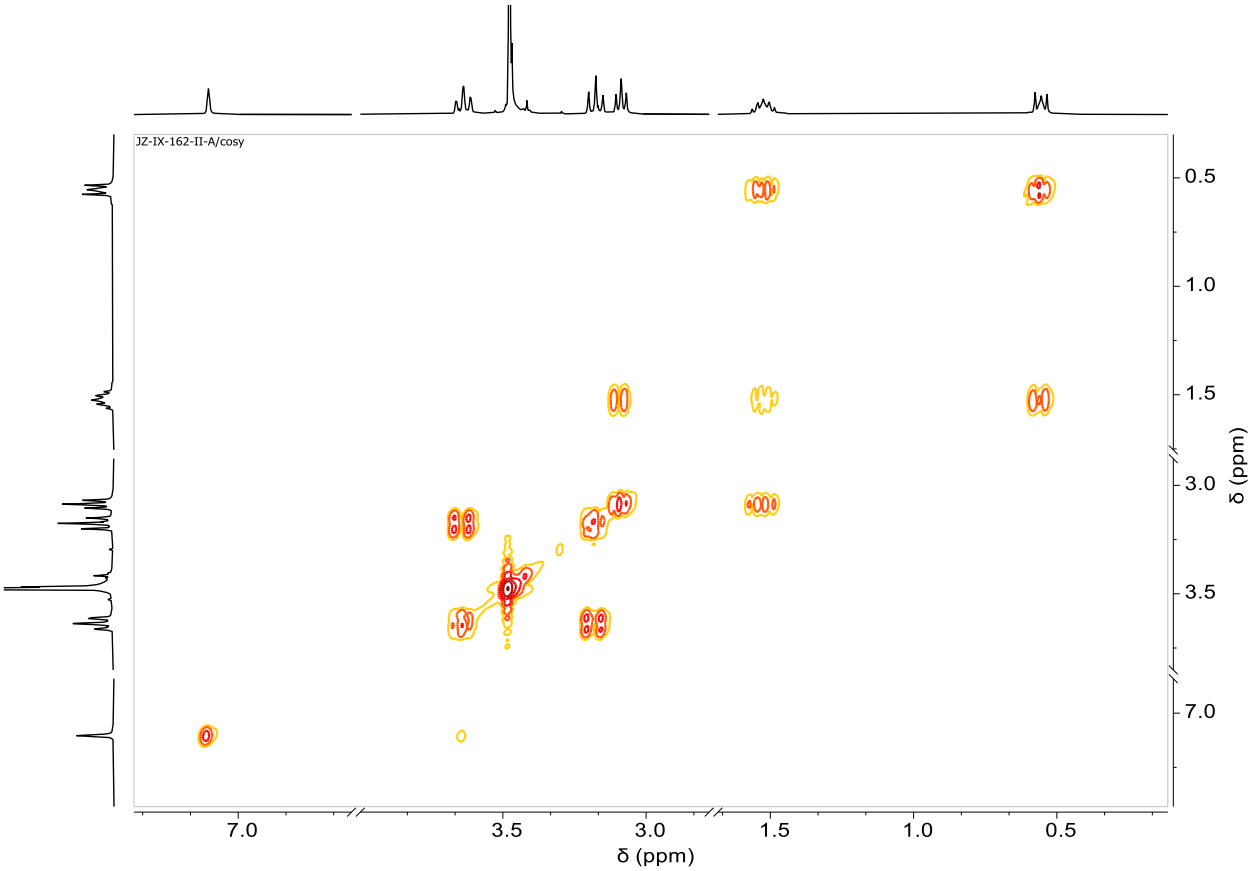

Figure S11. ^{1}H-^{1}H correlation spectrum (COSY) (d) of the reaction solution of AEAPTMS and FAI mixture after mixing (0.04 M, 1/1 ratio) in DMSO-d_6 for 10 h.

2.12. ^{1}H-^{13}C Heteronuclear Multiple Bond Quantum Coherence

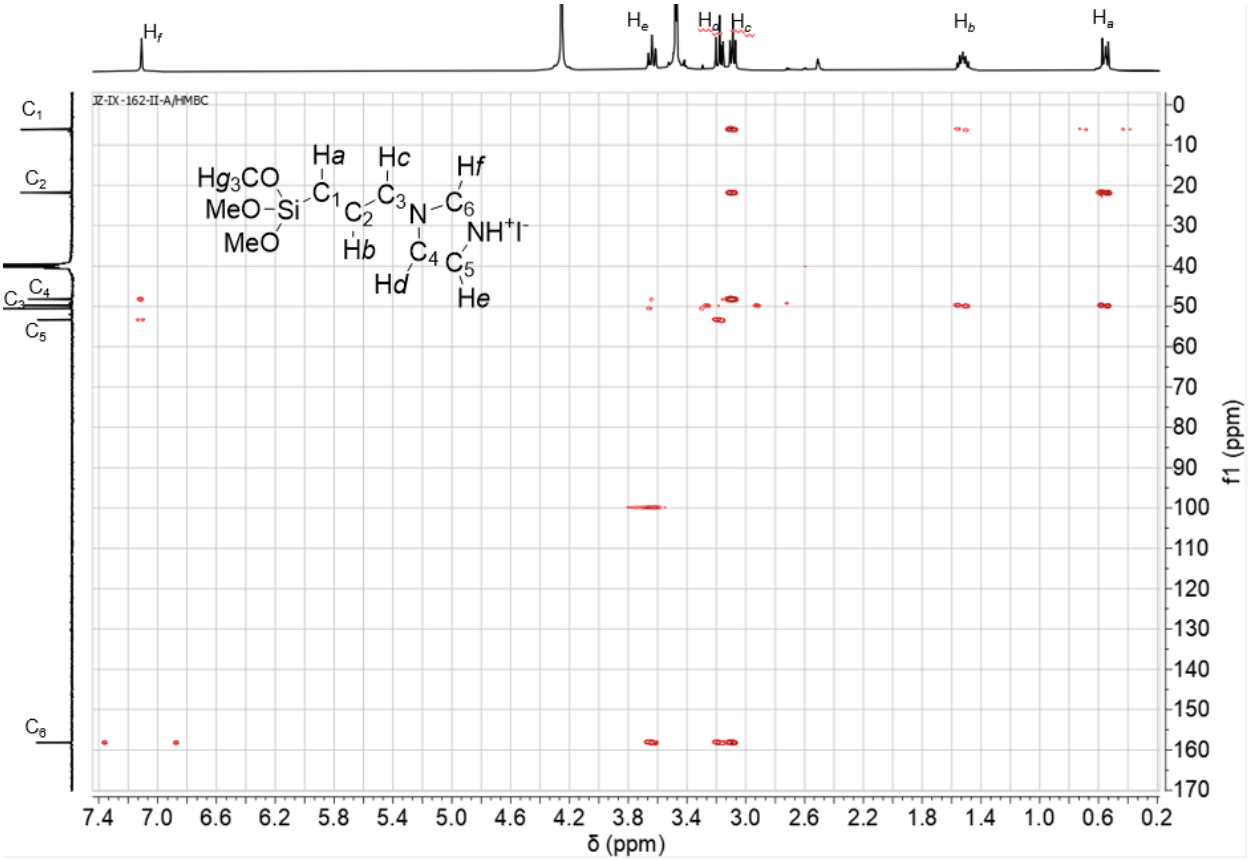

Figure S12. ^{1}H-^{13}C Heteronuclear Multiple Bond Quantum Coherence (HMQC) NMR spectrum of AEAPTMS and FAI mixture after mixing (0.04 M, 1/1 ratio) in DMSO-d_6 for 10 h.

2.13. Mass spectrum

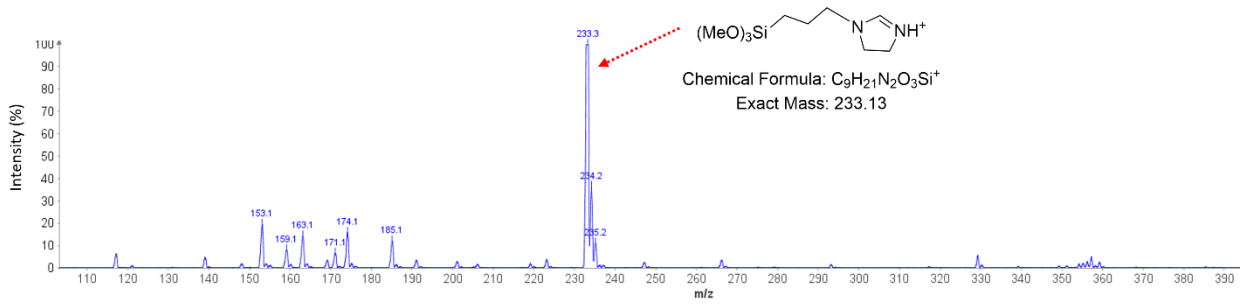

Figure S13. Mass spectrum of the solution of AEAPTMS and FAI mixture (1/1 ratio) in DMSO, immediately after mixing. The figure indicates that immediately after mixing, the reaction is complete (m/z = 233.3 corresponds to the substituted imidazolium derivative) and no substantial amount of the uncyclized monosubstituted formamidinium (m/z = 250.2) remains in the mixture.

2.14. Possible reactions in the AEAPTMS / FAI system

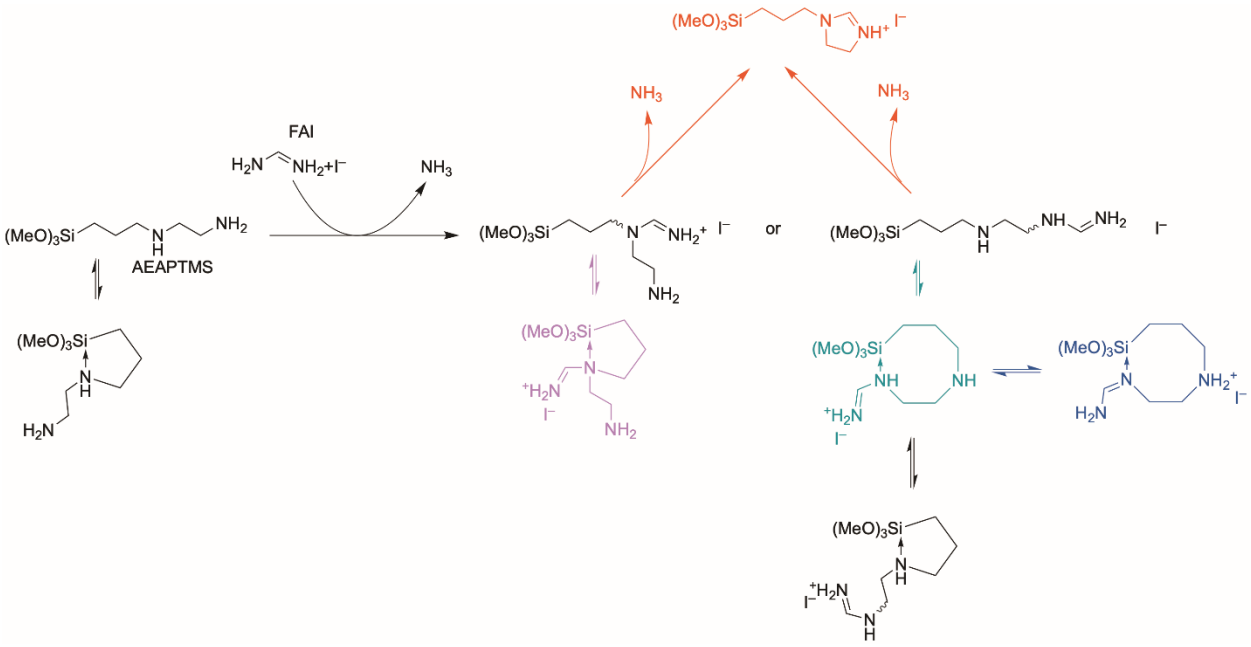

Figure S14. Possible reactions in the AEAPTMS / FAI system showing how 1-(3-(trimethoxysilyl)propyl)-4,5-dihydro-1*H*-imidazol-3-ium cation (red) can be formed by double condensation of AEAPTMS with FA^+, regardless of whether the secondary of primary amine reacts first. The intermediate formed through secondary amine / FA^+ reaction can form a five-membered ring analogous to the species shown in magenta in Figure S14 through coordination of the resulting tertiary amine to silicon (magenta); however, this species cannot be deprotonated to a cyclic formamidine. Conversely, the intermediate formed through primary amine / FA^+ reaction can cyclize to an eight-membered species (teal) that *can* be converted to a cyclic formamidine through internal proton transfer (dark blue-green) or transfer to another molecule of AEAPTMS (not shown); however, these products are not seen, since they are likely much less stable than the five-membered cyclic formamidines *and* the imidazolinium ion (red) is a stable product not possible in the case of using APTMS.

2.15. ^{1}H NMR spectra of the reaction product of APTMS and FAI

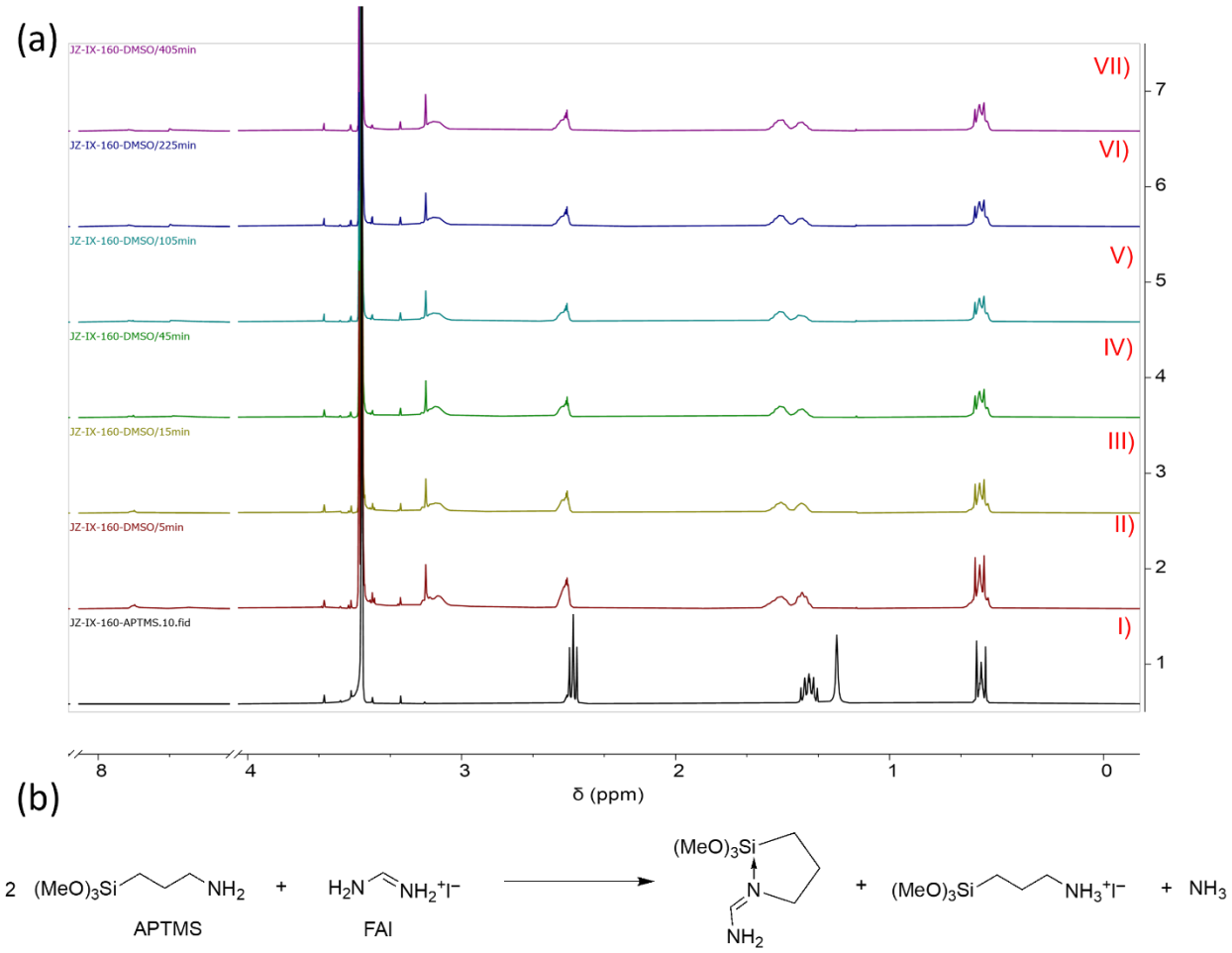

Figure S15. (a) ^{1}H NMR spectra of the reaction product of APTMS and FAI mixture in DMSO-d_4 (0.04 M) after mixing for I) 5 min, II) 15 min, III) 45 min, IV) 105 min, V) 330 min, and VI) 1390 min. (b) Schematic of the reaction.

2.16. Possible reactions in the APTMS / FAI system

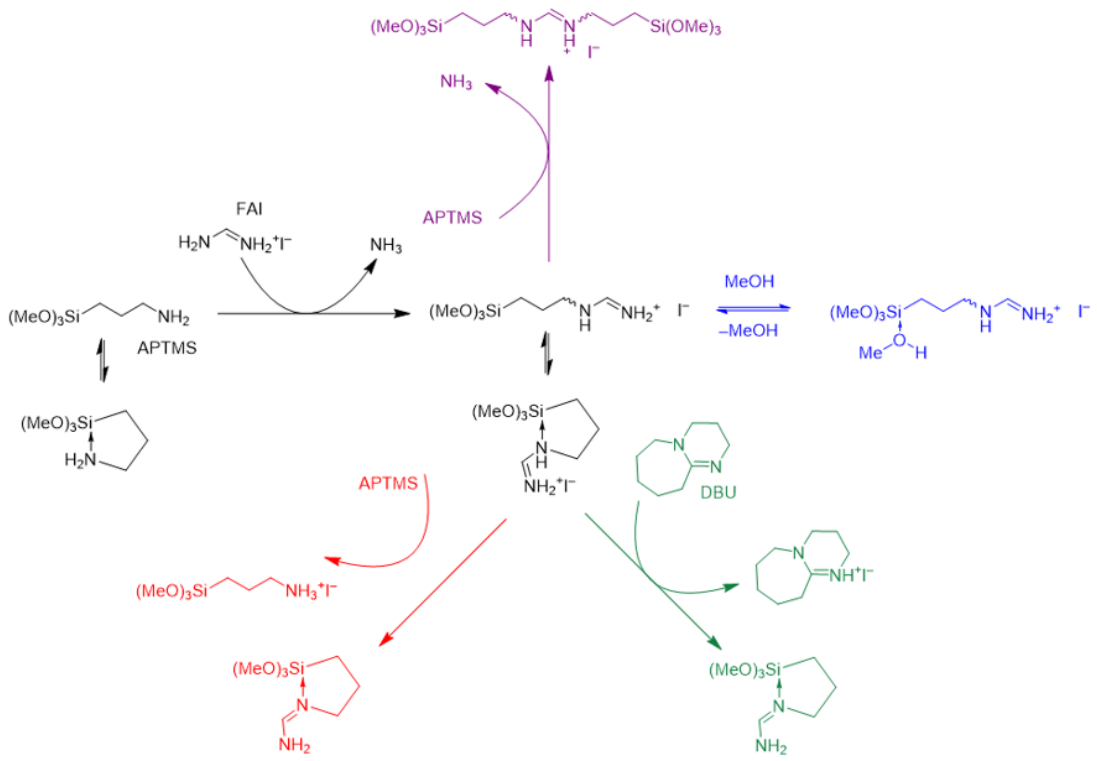

Figure S16. Possible reactions in the APTMS / FAI system. Deprotonation of a substituted cyclic formamidinium adduct to form a cyclic formamidine (red) accounts for the extent of reaction shown in Figure S15 (note that, in principle, coordination may precede deprotonation as shown here (magenta) deprotonation could precede coordination, or these processes could be concerted; also note that proton-transfer equilibria involving NH_3 / NH_4^+ are also possible, but volatile NH_3 will be lost from the system under many conditions). The reaction goes to completion in MeOH, presumably due to competitive Lewis acid-base formation with methanol (blue, see also Figure S17) or in the presence of a strong non-nucleophilic base (green, Figure S19). The *N,N′*-disubstituted formamidinium species can also be formed (purple) and participate in related equilibria.

2.17. NMR spectra of the reaction product of APTMS and FAI

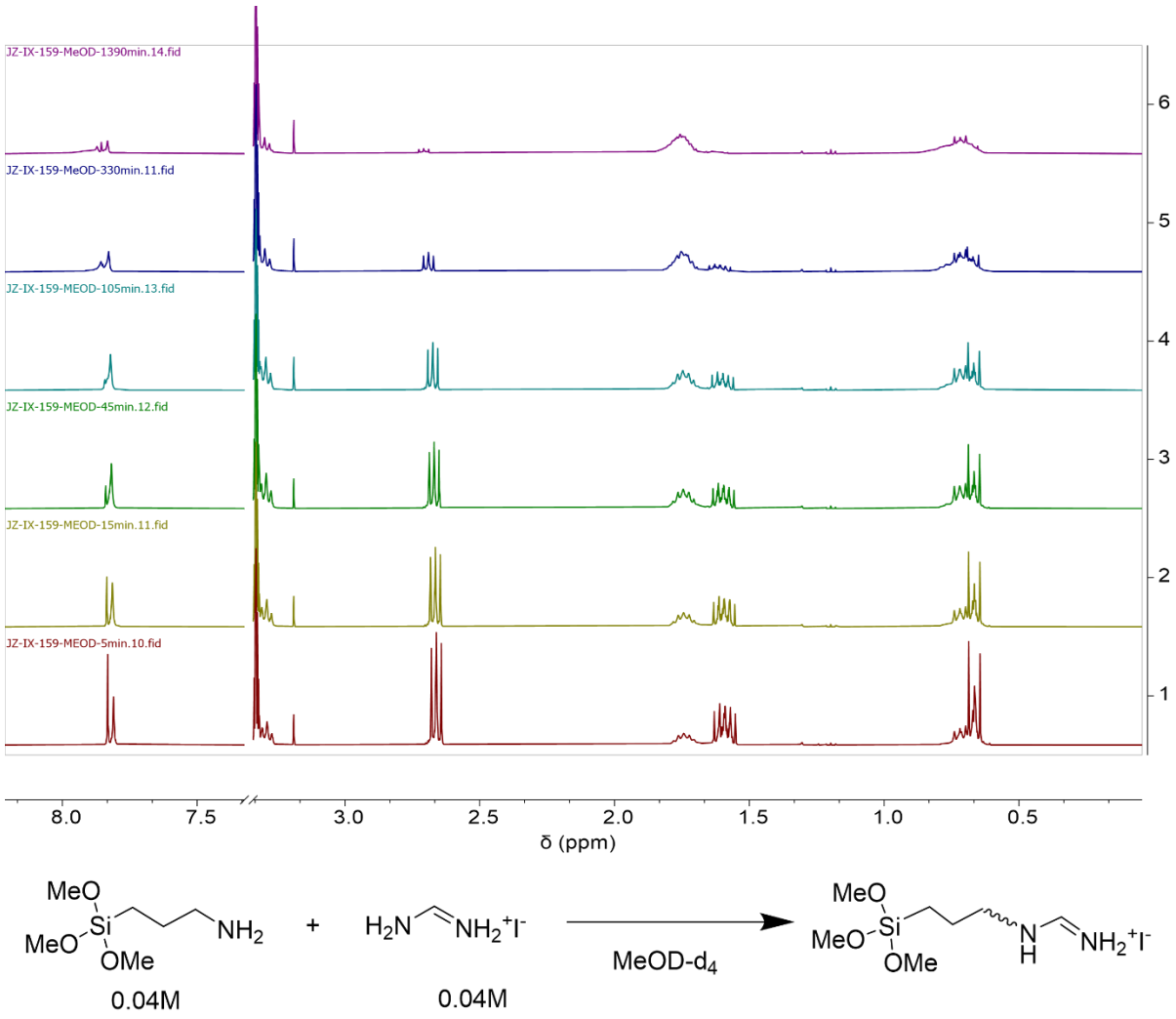

Figure S17. Top: ^{1}H NMR spectra of the reaction product of APTMS and FAI mixture in MeOD-d_4 (0.04 M) after mixing for I) 5 min, II) 15 min, III) 45 min, IV) 105 min, V) 330 min, and VI) 1390 min. Bottom: Schematic of the reaction (noting that methanol may be loosely coordinated to the silicon centers as shown for the blue structure of figure S16).

2.18. 1H NMR spectra

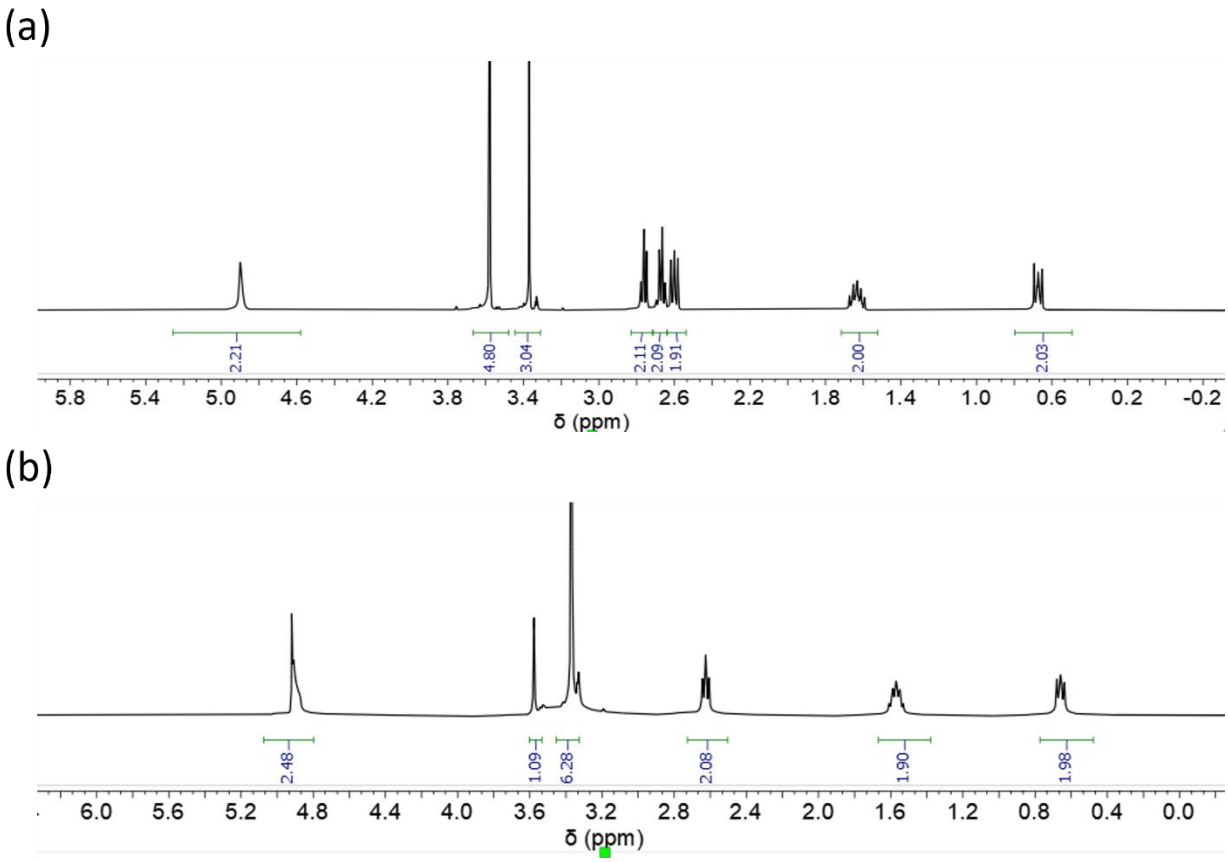

Figure S18. ^{1}H NMR spectra of (a) AEAPTMS and (b) APTMS in MeOD-d_4 (0.08 M) immediately after mixing. In both cases, the $(CH_3O)_3Si$ proton signal at ca. 3.6 ppm under integrates relative to other resonances, indicating ca. 50% and ca. 90% respectively are exchanged with the CD_3 groups of the solvent in this timeframe, presumably via coordination of CD_3OD as a Lewis base to the siloxane (as shown in blue in the upper part of Figure S16 for CH_3OH), followed by deuteron transfer, and dissociation of CH_3OD). The multiplet at ca. 3.3 ppm is attributable to the residual methyl proton signal of the deuterated methanol, the singlet at ca. 3.3 ppm to free CH_3OD, and the peak at ca. 4.9 ppm to the residual proton signal associated with the hydroxy group of deuterated and non-deuterated methanol.

2.19. 1H NMR spectra

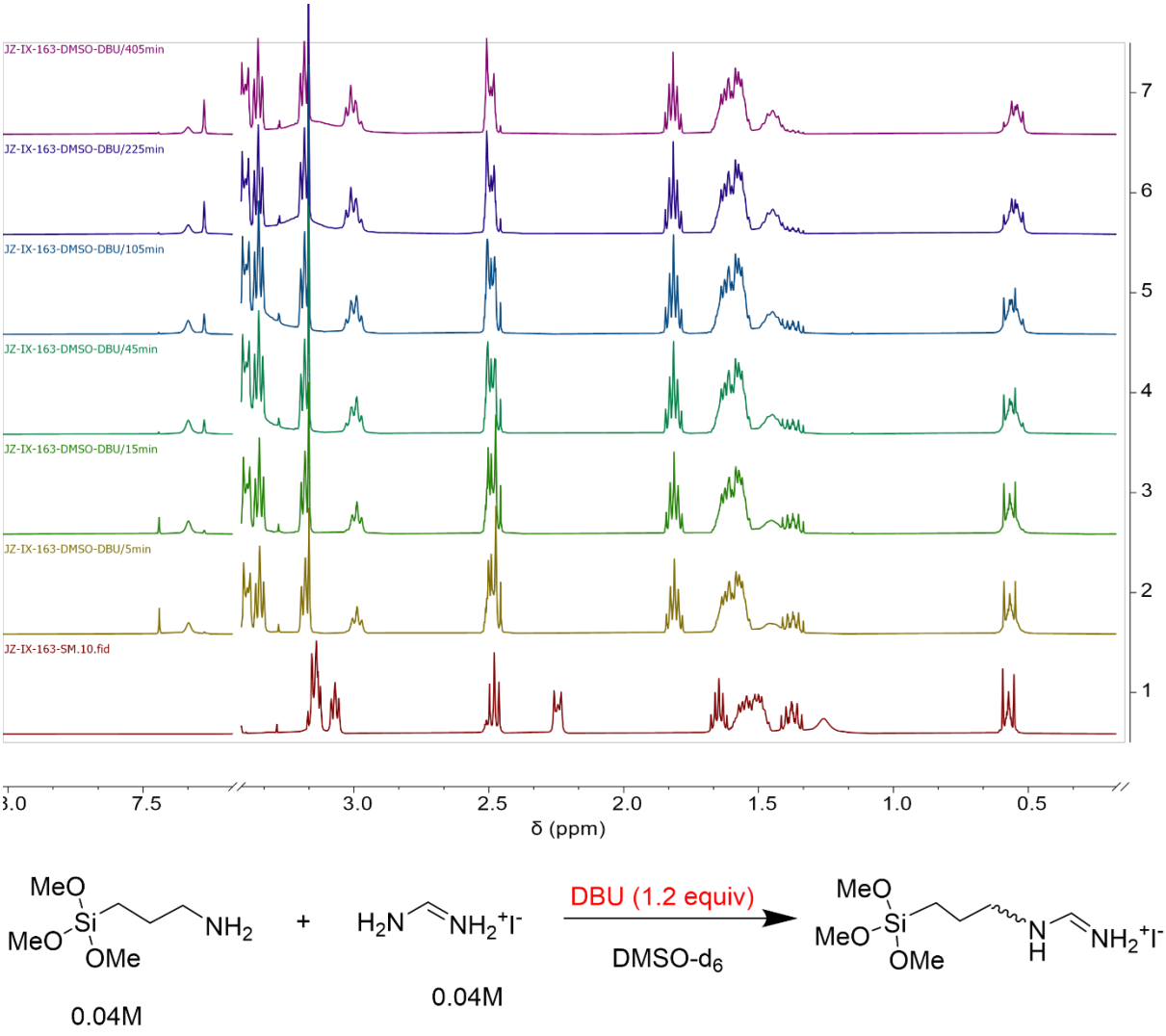

Figure S19. (a) ^{1}H NMR spectra of the reaction product of APTMS and FAI mixture in DBU (1.2 equiv.) after mixing for I) 5 min, II) 15 min, III) 45 min, IV) 105 min, V) 330 min, and VI) 1390 min. (b) Schematic of the reaction.

2.20. ^{1}H-^{1}H correlation spectroscopy

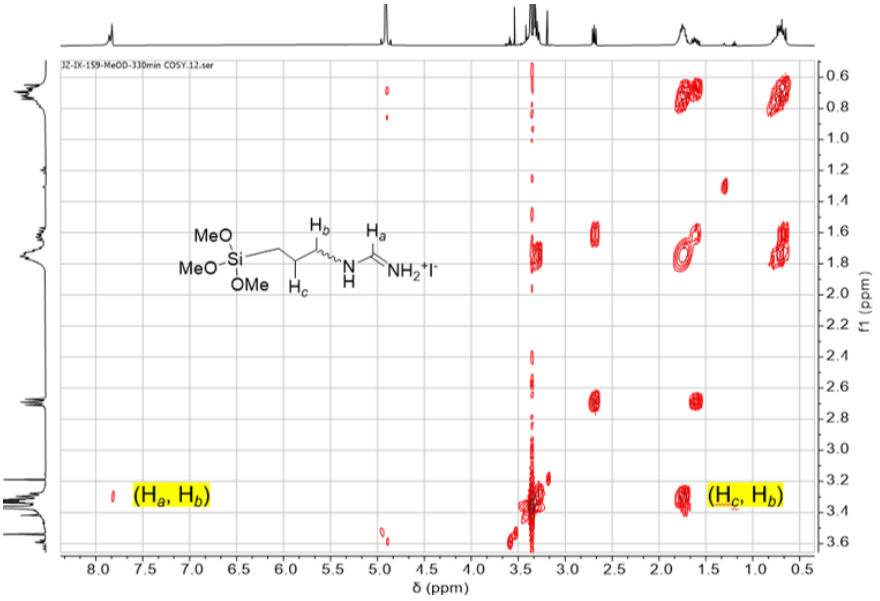

Figure S20. ^{1}H-^{1}H correlation spectroscopy (COSY) of a solution of APTMS and FAI mixture after mixing (0.04 M) in methanol-d_4.

2.21. ^{1}H-^{13}C Heteronuclear Single Quantum Coherence

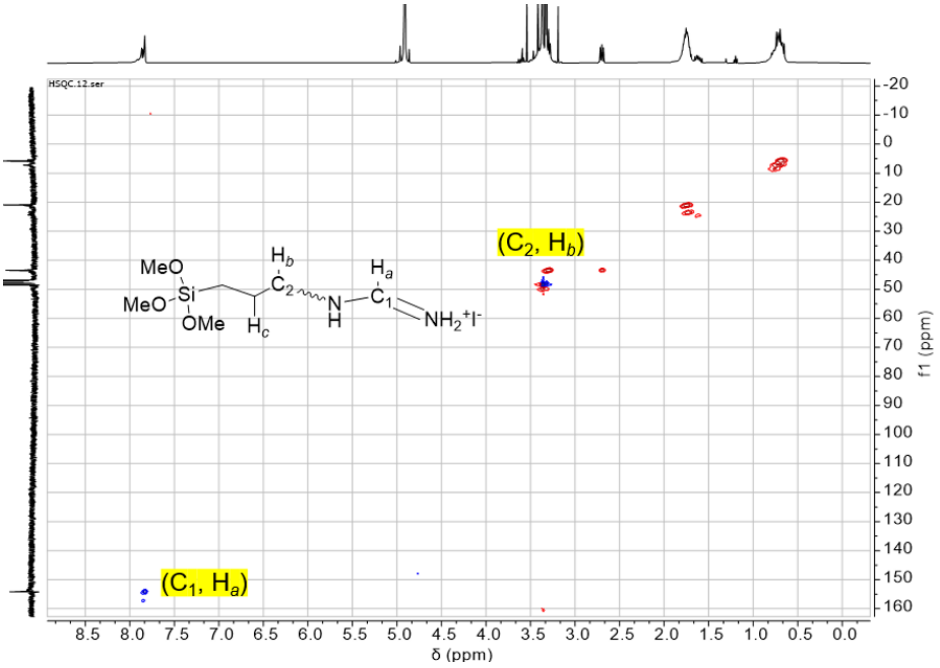

Figure S21. ^{1}H-^{13}C Heteronuclear Single Quantum Coherence (HSQC) NMR spectrum of APTMS and FAI mixture after mixing (0.04 M, 1/1 ratio) in methanol-d_4.

2.22. ^{1}H-^{13}C Heteronuclear Multiple Bond Quantum Coherence

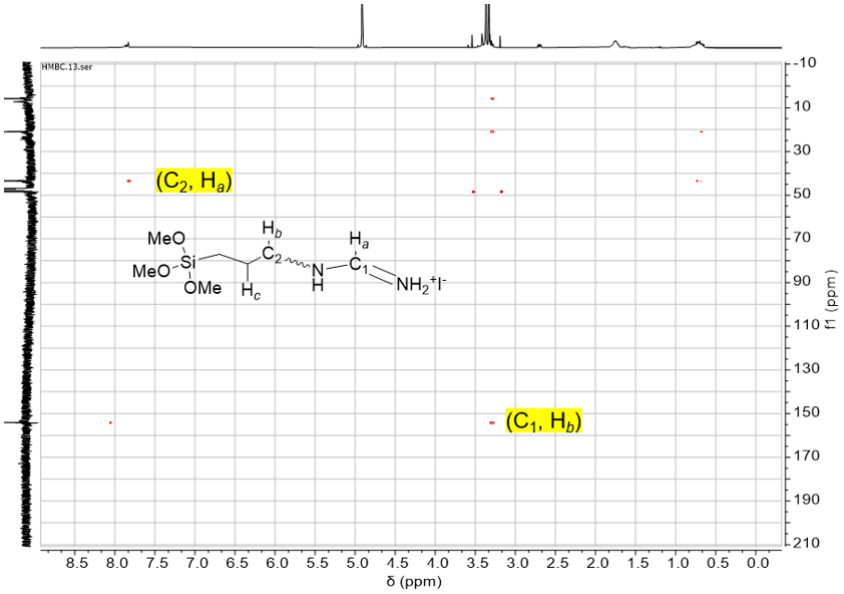

Figure S22. ^{1}H-^{13}C Heteronuclear Multiple Bond Quantum Coherence (HMQC) NMR spectrum of APTMS and FAI mixture after mixing (0.04 M, 1/1 ratio) in methanol-d_4.

2.23. Mass spectrum of the solution of APTMS and FAI mixture

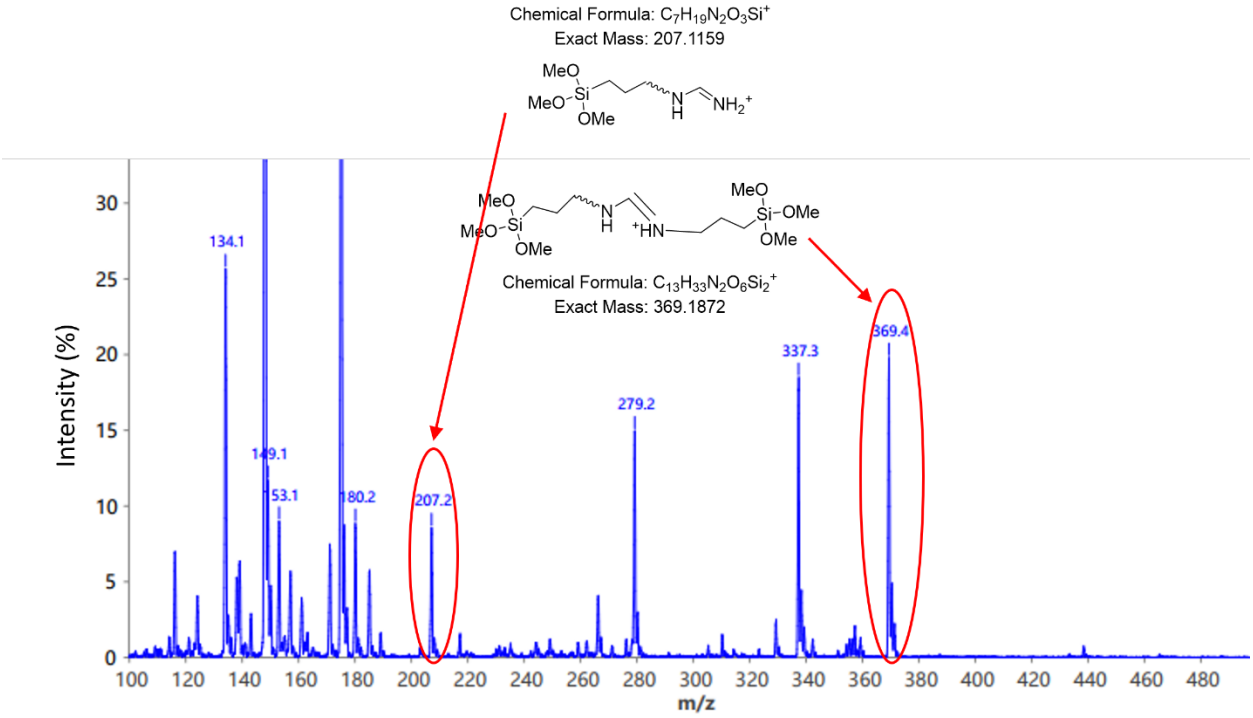

Figure S23. Mass spectrum of the solution of APTMS and FAI mixture (1/1 ratio) in MeOH, immediately after mixing. The figure indicates that, immediately after mixing, mono-substituted formamidinium (m/z = 207.2) and bis-substituted formamidinium (m/z = 369.2) are formed, while APTMS or its protonation product are also still present (*m/z*= 180.2 and 148.1 correspond to (MH^+) and $[MH\text{-}MeO]^+$ respectively).

2.24. ToF-SIMS mass spectra of APMTS

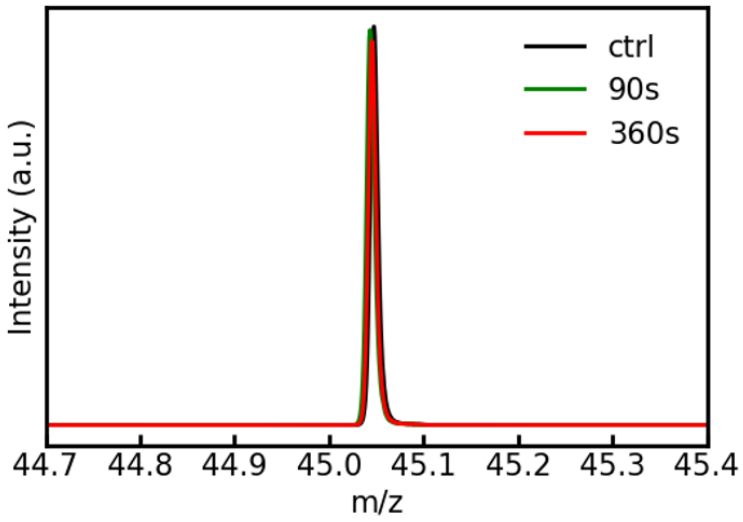

Figure S24. ToF-SIMS mass spectra at m/z = 45.05 of APMTS passivated perovskite film under different deposition time, corresponding to FA^+.

2.25. ToF-SIMS cation depth profile

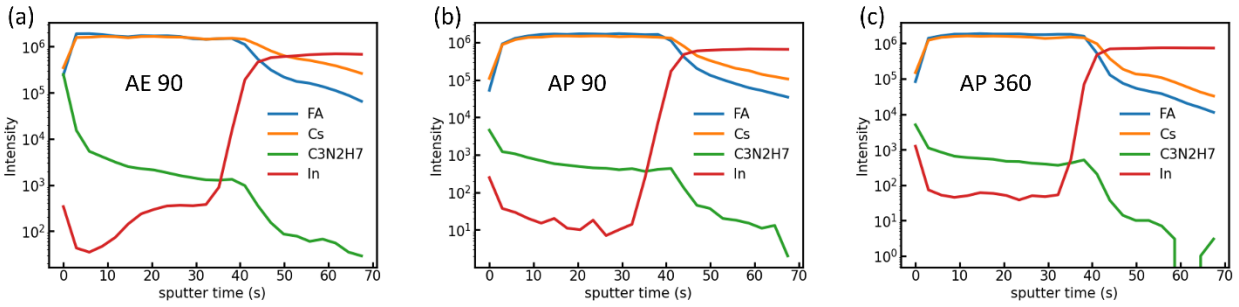

Figure S25. ToF-SIMS cation depth profile of perovskite film with (a) AEAPTMS 90 s, (b) APTMS 90s , and (c) APTMS 360 s treatment coated on ITO.

2.26. The experimental setup used for amino-silane vapor treatment

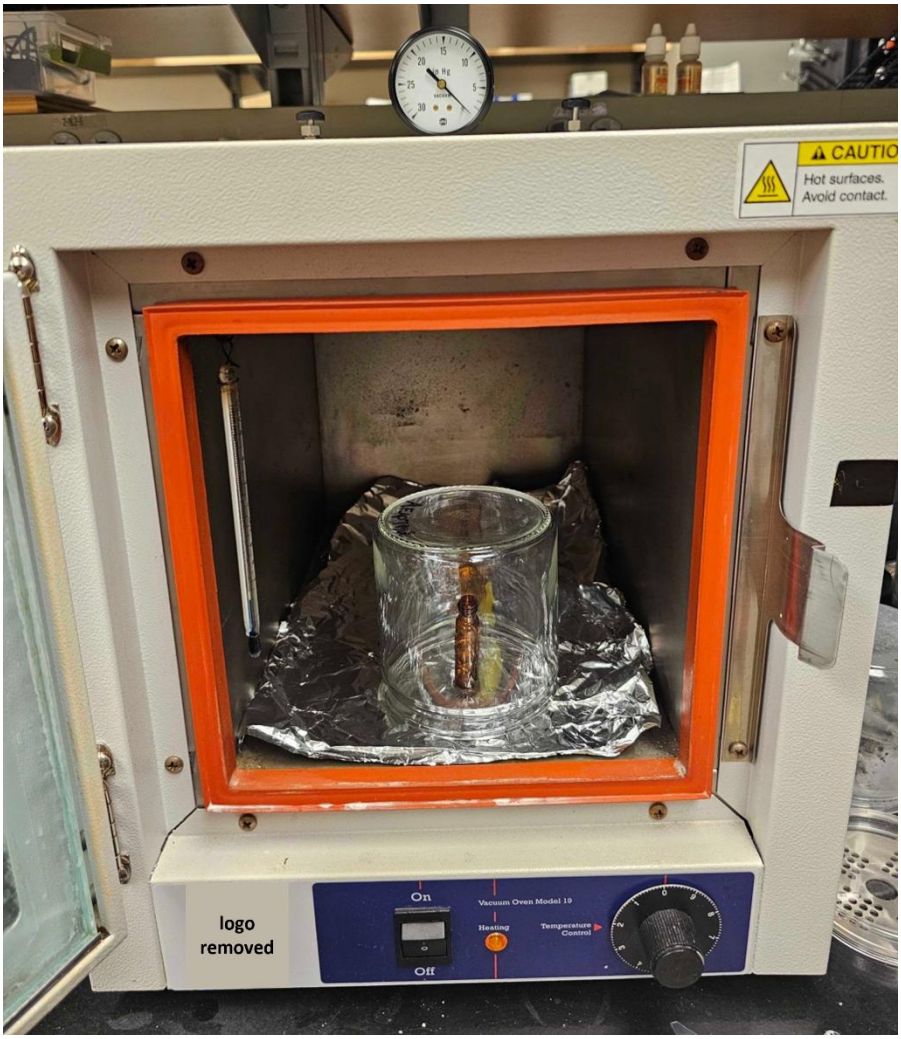

Figure S26. The experimental setup used for amino-silane vapor treatment.

B3. Supplementary Tables

Table S1. The stretched exponential decay fitting parameters for TRPL decays of unpassivated, APTMS-passivated, and AEAPTMS-passivated films. The values represent the mean ± standard error of the mean for three measurements performed on three different films.

Sample	β	τ_c (ns)	<τ> (ns)
Unpassivated	0.81 ± 0.04	302 ± 31	339 ± 26
30 s APTMS	0.80 ± 0.04	549 ± 104	618 ± 94
90 s APTMS	0.86 ± 0.01	2075 ± 148	2245 ± 151
360 s APTMS	0.85 ± 0.02	2011 ± 123	2190 ± 112
30 s AEAPTMS	0.85 ± 0.02	532 ± 63	579 ± 62
90 s AEAPTMS	0.75 ± 0.02	788 ± 54	937 ± 58
360 s AEAPTMS	0.88 ± 0.03	2065 ± 278	2200 ± 260

Table S2. The mean and sample standard deviation values of unpassivated, APTMS-passivated, and AEAPTMS-passivated solar cells shown in Figure 2c-f and Figure S6.

Sample	**V_{OC} (V)**	**J_{SC} (mA/cm^2)**	**FF (%)**	**PCE (%)**
Unpassivated	1.08 ± 0.02	21.09 ± 0.89	70.88 ± 2.07	16.15 ± 0.78
30 s APTMS	1.12 ± 0.01	21.15 ± 0.17	75.27 ± 1.84	17.75 ± 0.62
90 s APTMS	1.11 ± 0.01	20.77 ± 0.68	77.84 ± 2.67	17.87 ± 0.65
360 s APTMS	0.94 ± 0.02	16.19 ± 1.01	63.87 ± 4.19	9.71 ± 1.12
30 s AEAPTMS	1.15 ± 0.01	21.63 ± 0.34	81.11 ± 1.42	20.20 ± 0.52
90 s AEAPTMS	1.16 ± 0.01	21.65 ± 0.47	79.72 ± 1.44	20.02 ± 0.65
360 s AEAPTMS	1.17 ± 0.02	16.28 ± 2.36	67.89 ± 8.11	13.04 ± 2.99

B4. References

(1) Jariwala, S.; Burke, S.; Dunfield, S.; Shallcross, R. C.; Taddei, M.; Wang, J.; Eperon, G. E.; Armstrong, N. R.; Berry, J. J.; Ginger, D. S. Reducing Surface Recombination Velocity of Methylammonium-Free Mixed-Cation Mixed-Halide Perovskites via Surface Passivation. *Chem. Mater.* **2021**, *3* (13), 5035–5044. https://doi.org/10.1021/acs.chemmater.1c00848.

(2) Shi, Y.; Rojas-Gatjens, E.; Wang, J.; Pothoof, J.; Giridharagopal, R.; Ho, K.; Jiang, F.; Taddei, M.; Yang, Z.; Sanehira, E. M.; Irwin, M. D.; Silva-Acuña, C.; Ginger, D. S. (3-Aminopropyl)Trimethoxysilane Surface Passivation Improves Perovskite Solar Cell Performance by Reducing Surface Recombination Velocity. *ACS Energy Lett.* **2022**, *7* (11), 4081–4088. https://doi.org/10.1021/acsenergylett.2c01766.

(3) Akrami, F.; Jiang, F.; Giridharagopal, R.; Ginger, D. S. Kinetic Suppression of Photoinduced Halide Migration in Wide Bandgap Perovskites via Surface Passivation. *J. Phys. Chem. Lett.* **2023**, *14* (41), 9310–9315. https://doi.org/10.1021/acs.jpclett.3c02570.

(4) Taddei, M.; Jariwala, S.; Westbrook, R. J. E.; Gallagher, S.; Weaver, A. C.; Pothoof, J.; Ziffer, M. E.; Snaith, H. J.; Ginger, D. S. Interpreting Halide Perovskite Semiconductor Photoluminescence Kinetics. *ACS Energy Lett.* **2024**, *9* (6), 2508–2516. https://doi.org/10.1021/acsenergylett.4c00614.

Acknowledgement of Artificial Intelligence Tool Use

We acknowledge the use of ChatGPT 5 to assist in proofreading portions of the thesis for grammar and readability. The entire draft was written and reviewed by the author, and ChatGPT was used to identify areas for revision and provide suggested alternative text, which was selected and revised by the author. The author acknowledges responsibility for all content in the thesis.